VRIJE UNIVERSITEIT

A CRYOGENIC BUFFER GAS BEAM SOURCE OF BaF MOLECULES

ACADEMISCH PROEFSCHRIFT

ter verkrijging van de graad Doctor aan
de Vrije Universiteit Amsterdam,
op gezag van de rector magnificus
prof.dr. J.J.G. Geurts,
volgens besluit van de decaan
van de Faculteit der Bètawetenschappen
in het openbaar te verdedigen
op dinsdag 3 juni 2025 om 13.45 uur
in de universiteit

door

Maarten Cornelis Mooij

geboren te Vlissingen

promotoren:	prof.dr. H.L. Bethlem prof.dr. W.M.G. Ubachs
promotiecommissie:	prof.dr. S. Hoekstra dr. J. Onvlee prof.dr. H.G. Raven dr. S. Truppe prof.dr. O.O. Versolato

This work is done as part of the NL-*e*EDM consortium, which received funding from the Dutch Research Council (NWO) via grants EEDM-166 and XL21.074 and was carried out at the LaserLaB of the Vrije Universiteit.

The cover of this thesis shows a section view of the 3D model of the cryogenic source described in this thesis. The model is hidden behind a blue layer, which is partially transparent. The shape of the transparency corresponds to a phase-space distribution reconstructed to the cell exit.

Printed by Ipskamp Printing B.V., Enschede
ISBN: 978-94-6473-817-9
DOI: https://doi.org/10.5463/thesis.1236

Contents

Introduction

1

1.1 The electric dipole moment of the electron

The standard model (SM) of particle physics is a well-tested theory that describes matter and its interactions in terms of elementary particles [1]. However, in the universe, a large matter-antimatter asymmetry is observed, whose magnitude cannot be explained by the SM [2]. A symmetry breaking between matter and antimatter requires CP-violation, where C and P stand for charge conjugation symmetry and parity, respectively. CP-violation within the SM has been observed in the decay of kaons [3], but this is insufficient to explain the magnitude of the asymmetry. According to the CPT-theorem of quantum field theory, where T stands for time-reversal symmetry, a violation of CP implies that T-symmetry is broken. Thus, to explain the matter-antimatter asymmetry, a much larger T-violation is necessary than that predicted by the SM.

An experimental approach to test time-reversal symmetry is to search for non-zero electric dipole moments of fundamental particles, such as the electron. A non-zero electric dipole moment of the electron (*e*EDM) implies a non-uniform charge distribution along the spin axis, and this breaks time-reversal symmetry. As the SM was insufficient to explain the matter-antimatter asymmetry, the *e*EDM predicted by the SM is also very small, $\mathcal{O}(10^{-35})$ e cm [4] and currently experimentally far out of reach. However, in an attempt to solve the matter-antimatter asymmetry, theories beyond the standard model (BSM) typically predict a much larger value of the *e*EDM [5]. Therefore, searching for an *e*EDM is a very sensitive probe to test a broad range of BSM-theories. In other words, if a non-zero value is found, it immediately implies the breakdown of the SM.

1.2 Measuring the electric dipole moment of the electron

Through the years, multiple experiments have been performed using neutrons, atoms, and molecules to search for permanent EDMs. Due to the strong enhancement through the internal structure of molecules [6], the most sensitive *e*EDM measurements are performed on (neutral or ionic) molecules, namely, in YbF [7, 8], ThO [9, 10] and the current best value of $|d_e| < 4.1 \times 10^{-30}$ e cm using HfF^+ [11]. We aim to perform

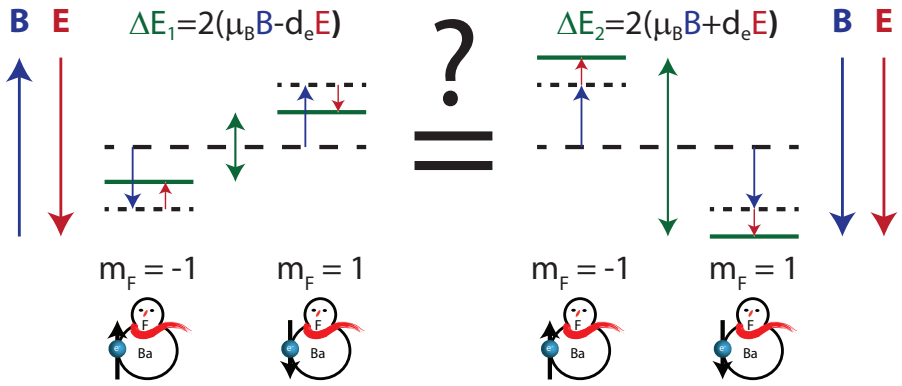

FIGURE 1.1: A cartoon-like schematic overview displaying the experimental method used to search for an *e*EDM in BaF. Magnetic (**B**) and electric (**E**) fields applied to BaF molecules induce energy shifts of the magnetic hyperfine states m_{F} depending on the orientation of the spin of the valence electron with respect to the fields. The shift due to the magnetic interaction is indicated by the blue arrows, whereas the (much smaller) shift resulting from the interaction of the permanent electric dipole with the electric field is indicated by the red arrows.

a sensitive measurement using BaF molecules [12]. Note that the current limits on the electric dipole moments are exceedingly small. For reference, $4.1 \times 10^{-30}\ e\,\mathrm{cm}$ corresponds to 2×10^{-21} Debye, while the body-fixed electric dipole moments of molecules are typically of the order of 1 Debye. However, the *CP*-violating electric dipole moment of the electron is fundamentally different from that of a molecule as it is *permanent*, i.e., it occurs even in zero electric field and the energy shift is linear in low electric fields, while the electric dipole moment of a molecule is *induced*, i.e., it is zero in zero electric field and the energy shift depends quadratically on sufficiently small applied electric fields. This difference makes it possible to distinguish these two dipole moments even though one is many orders of magnitude smaller than the other.

Figure 1.1 shows the experimental method of the NL-*e*EDM experiment. In the experiment, a relative energy shift, ΔE, is measured between two opposite magnetic hyperfine substates ($m_{\mathrm{F}} = \pm 1$). On the left- and right-hand sides, the energy shift (not to scale) of the two hyperfine states is shown when opposite or parallel magnetic and electric fields are applied, respectively. The question the NL-*e*EDM experiment tries to answer, is whether the energy differences between the hyperfine states on the left- and right- hand sides are the same, or that a non-zero *e*EDM leads to an additional opposite energy shift in the hyperfine states. Note that the energy shift drawn in the figure due to an electric field assumes a positive value of d_e, but so far the sign is unknown.

In the experiment, molecules are brought into a superposition of two $m_{\mathrm{F}} = \pm 1$ magnetic hyperfine substates. When applying magnetic and electric fields, the states start to precess, and as a result of the different energy, at a different frequency. The

phase difference induced by the permanent electric dipole moment d_e is [12]:

$$\phi_{\mathrm{EDM}} = d_e |P| E_{\mathrm{eff}} \tau / \hbar, \tag{1.1}$$

with $|P|$ the polarizability of the polar molecule in an external electric field and E_{eff} the effective electric field experienced by the valence electron within the molecule. E_{eff} cannot be measured directly and is calculated using methods from theoretical chemistry. The time τ the molecules coherently interact with the external fields is ultimately determined by the velocity of the molecules. $\hbar$ is the reduced Planck constant.

The statistical uncertainty of the experiment is given by:

$$\sigma_{\mathrm{d}} = \frac{\hbar}{e} \frac{1}{2|P| E_{\mathrm{eff}} \tau \sqrt{\dot{N} T}}, \tag{1.2}$$

with e the elementary charge, $\dot{N}$ the number of molecules per second and T the total measurement time.

We use the rather heavy polar molecule BaF, which is easily polarisable and has an effective electric field equal to $E_{\mathrm{eff}} \approx 6.5$ GV/cm [13]. Although E_{eff} is smaller than in other molecules used in *e*EDM searches such as ThO ($\sim$78 GV/cm [10]), YbF ($\sim$23 GV/cm [14]) and HfF^+ ($\sim$23 GV/cm [11]), this is compensated by the fact that the small mass, relative to other species used for *e*EDM searches, makes it feasible to decelerate BaF using Stark deceleration. Furthermore, BaF has a level structure that is suitable for laser cooling [15–17]. The design of the experimental setup focusses on increasing the coherence time and the total number of molecules. Because of the $1/\left(\tau\sqrt{\dot{N}}\right)$ dependence, increasing the coherence time is advantageous, as long as the number of molecules does not drop more than the square root. This is the motivation for the design of the NL-*e*EDM experiment, which has been built up over the past few years. The first generation aims to reach an uncertainty below 5×10^{-30} e cm [12].

1.3 Design and current states of the NL-*e*EDM setup

The design of the setup is shown in Figure 1.2. The major components are the cryogenic source, an electrostatic lens, the travelling-wave Stark decelerator, a transverse laser cooling section, a state preparation and interaction zone, and a detection zone. Before turning to the cryogenic source, which is the central topic of this thesis, I will briefly discuss the details of the other subcomponents of the setup, mainly based on theses of fellow PhD students on the project, and conclude with a theoretical analysis that has been performed in addition to the experimental work.

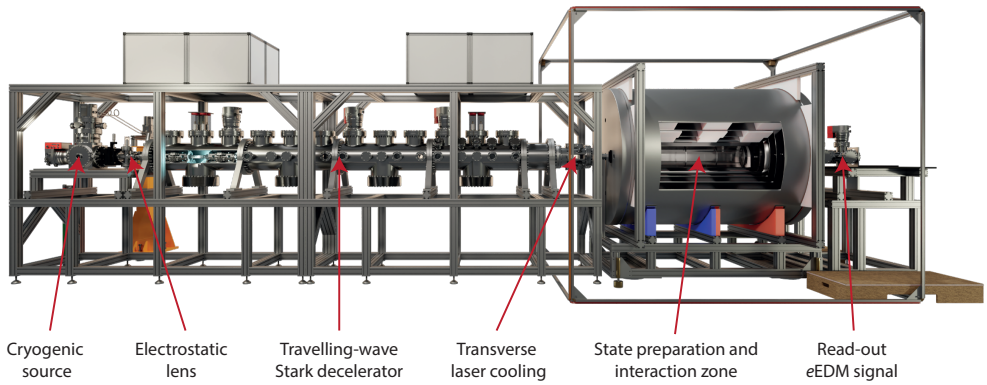

FIGURE 1.2: Overview of the NL-*e*EDM setup. The molecular beam, propagating from left to right, is produced in a cryogenic source, focused with an electrostatic lens into the Stark decelerator, which reduces the longitudinal velocity. The transverse velocity is reduced by laser cooling after the decelerator. After bringing the molecules into the superposition state and applying well-controlled electric and magnetic fields, the *e*EDM signal is readout. *3D drawing made by Anno Touwen.*

1.3.1 The travelling-wave Stark decelerator

A key feature of the NL-*e*EDM setup is the travelling-wave Stark decelerator, which uses time-varying electric fields to reduce the forward velocity of a molecular beam [18, 19] and by that increases the coherence time in the *e*EDM measurement. The travelling-wave Stark decelerator consists of a 4.5 m long series of 4 mm diameter rings. Per set of eight consecutive rings, two local electric field minima are generated by applying a sinusoidal voltage distribution to the rings. Molecules in low-field seeking states are confined in the electric field minima. By modulating the voltages applied to the rings, the local minima can be made to move through the decelerator. By reducing the frequency of the modulation, the minima, and hence the molecules confined to these minima, are slowed down. More details are decribed by Zapara [20], Aggarwal [21] and Touwen [22]. Using this decelerator, SrF has been decelerated to a complete stand still and was trapped for up to 50 ms in static fields [21]. BaF, which is heavier and therefore more difficult to decelerate, has so far been decelerated from 200 m/s to 150 m/s [22].

1.3.2 The electrostatic lens

To optimise the phase-space matching of the cryogenic beam to the travelling wave Stark decelerator, an electrostatic hexapole lens was placed in between the two. This lens reduces losses due to the relatively long free flight distance that is required to be able to install a valve between the source and the decelerator that seals off the decelerator when the source is being serviced. It was shown by Touwen *et al.* [23], that

by including the lens, the number of decelerated BaF was increased by a factor of 2.5. Furthermore, the lens allows for easy alignment of the beam into the decelerator.

1.3.3 Transverse laser cooling

A low forward velocity can be achieved by combining a cryogenic source and a travelling-wave Stark decelerator. To reduce losses, while the molecular beam passes through the > 50 cm interaction zone, the transverse velocity will be reduced by applying laser cooling. Due to its relatively high mass, $\sim$2000 photons need to be scattered to cool BaF to the Doppler limit [12]. For most molecules, scattering 2000 photons would be prohibited by spontaneous decay of the excited state into higher lying vibrational states of the electronic ground state. However, BaF is very 'diagonal' [15], which means that electronically excited vibrational states predominantly decay to their counterparts in the electronic ground state, and leaks can be closed by adding a limited number of laser frequencies to repump molecules that have decayed to unwanted states. Currently, various groups are experimentally studying laser cooling of BaF molecules [17, 24]. The opportunity of combining Stark deceleration with (transverse) laser cooling was one of the main reasons why the BaF molecule was selected for the NL-*e*EDM experiment. The 2D-transverse laser cooling is being experimentally explored by van Hofslot, following a cycling scheme as demonstrated for YbF by Ho *et al.* [25].

1.3.4 State preparation, interaction zone and detection zone

The *e*EDM states used in our experiment are the two magnetic hyperfine sublevels $m_{\mathrm{F}} = -1$ and $m_{\mathrm{F}} = 1$ of the $F = 1$ hyperfine component of the $\mathrm{X}^2\Sigma^+, v = 0, N = 0$ ground state of BaF. A purely optical method is used to bring the molecules in the $m_{\mathrm{F}} = \pm 1$ superposition state. Via counter-propagating (with respect to the molecular beam) laser pulses, precise control over all necessary parameters is achieved [26].

After preparation, a potential *e*EDM phase-shift builds up between the two components of the superposition as the molecules propagate through an interaction zone with well-controlled electric and magnetic fields. Homogeneous electric fields of several kV/cm are imposed by applying opposite voltages to two indium tin-oxide coated glass plates, while double-cosine coils are used to generate homogeneous magnetic fields at nT level. To minimise magnetic field fluctuations, the interaction zone is shielded by 5 layers of μ-metal, while the external magnetic field is compensated using large coils in a Helmholtz configuration. Details on electric and magnetic field control are described by Meijknecht [27].

The fluorescence signal recorded after the interaction zone as a function of the frequency difference between the two lasers contains information on a possible *e*EDM, as well as the strengths of the applied external electric and magnetic fields. A refined

model based on optical Bloch equations is developed, including all hyperfine levels in the ground state, to extract all information from the measured spectrum. The resulting information is used to suppress systematic effects originating from imperfections [26]. More details on the method for preparing molecules in superposition and reading out and analysing the signals are described by Boeschoten [28], Marshall [29] and Touwen [22]. In order to optimise multiple components of the NL-*e*EDM-setup in parallel, the *e*EDM measurements discussed here were performed using the so-called 'fast' beam source that combines the expansion of carrier gas (a mixture of 2% SF_6 and 98% argon) from an Even–Lavie valve with laser ablation of a barium atoms from a metal target [30].

1.3.5 Theoretical investigations

Theoretical calculations are crucial to determine the magnitude of the *e*EDM from a measured asymmetry arising from CP-violation, or, if no asymmetry is measured, to set an upper limit for the *e*EDM. For paramagnetic systems such as the BaF molecule, two parity and time-reversal symmetry-breaking interactions between electrons and nucleons are dominant, namely the *e*EDM and a nucleon-electron scalar-pseudoscalar interaction. In our consortium, the molecular enhancement factors W_d and W_s that relate a measured energy shift to a value of the corresponding electron-nucleon interaction are calculated using advanced *ab initio* electronic structure calculations [13].

In addition to accurate values, a reliable uncertainty estimation is equally important and for this a systematic method is developed, as described in detail by Haase [31]. As these (nuclear-dominated) properties cannot be derived from experiments, the same *ab initio* framework is applied to calculate the hyperfine structure constants of BaF, which concerns similar properties, but allows for direct comparison with experimental measurements. These calculations, including uncertainty estimation, and the comparison with the effective molecular hyperfine constants derived from spectroscopic measurements are presented Denis *et al.* [32]. The spectroscopic measurements are presented in Marshall [29].

1.4 The cryogenic source

The discussion so far has omitted what is arguably the most important part of the experiment; the molecular beam source. In order to reach high sensitivity, the initial molecular beam should be both intense and cold such that most molecules reside in the lowest quantum states that are used in the *e*EDM measurement. Additionally, the forward velocity of the molecules should be relatively low, such that they can be efficiently decelerated in our 4.5 meter long decelerator. To meet these requirements,

a cryogenic buffer gas-cooled beam source has been developed and characterised. This was the main task of this PhD work. In a cryogenic source, the species of interest is produced inside a cell that contains a high density of buffer gas at cryogenic temperatures. Through an orifice in the cell, the molecules and buffer gas escape into a vacuum to form a molecular beam. For many applications and many molecules and especially for radicals such as BaF, a beam produced in a cryogenic buffer gas cell has a brightness that is typically a few orders of magnitude higher than supersonic beams expanding from 'standard' pulsed valves, while its forward velocity is much smaller. The rotational temperature in a cryogenic beam is typically somewhat higher than that of standard supersonic sources.

The increased brightness in a cryogenic beam is a result of the better entrainment of the molecules in the buffer gas. In supersonic sources, BaF molecules are produced close to the nozzle, which releases a short pulse of carrier gas that expands into the vacuum [30, 33, 34]. Because of the small spatial extent of the expanding beam, only a small fraction of the ablated atoms are captured by the carrier gas. In contrast, in a cryogenic source, the local density is much higher and the volume is much larger, resulting in a larger fraction of the atoms being entrained. After being captured, the molecules slowly travel with the buffer gas towards the exit and leave the cell to form a molecular beam. The resulting beam pulses typically have a temporal distribution with a width of 1 ms, much longer than that of a supersonic beam source, which have durations below 100 μs. Therefore, while the total number of molecules produced by a cryogenic beam is much larger, the phase-space *density* is comparable to that of a supersonic source.

The lower forward velocity is due to the use of buffer gas at cryogenic temperatures. The mean longitudinal velocity of a molecular beam is $v_{\parallel} \propto \sqrt{T/m}$, with T the temperature of the gas and m the mass of the gas particles, which is effectively the mass of the buffer gas atoms. Hence, by lowering the temperature of the cell the forward velocity is reduced.

Figure 1.3 provides a literature overview of molecular sources in terms of forward velocity and molecular brightness per pulse. The main focus in the figure is on cryogenic buffer gas beam sources, separated by single- and double-stage cell designs, and, for comparison, three supersonic sources are included. This representation is chosen to achieve a clear overview of many sources, but obviously summarising a source by a single data point does not tell the complete story. More sources have been reported in literature, but they could not be included due to the lack of knowledge on the brightness and/or forward velocity. An important parameter not covered by the figure is the repetition rate of the pulsed beams, which is typically 1-2 Hz for sources that use helium as buffer gas, while 10 to 100 Hz has been reported for neon buffer gas sources.

The trends described above are clearly visible. Supersonic sources are operated

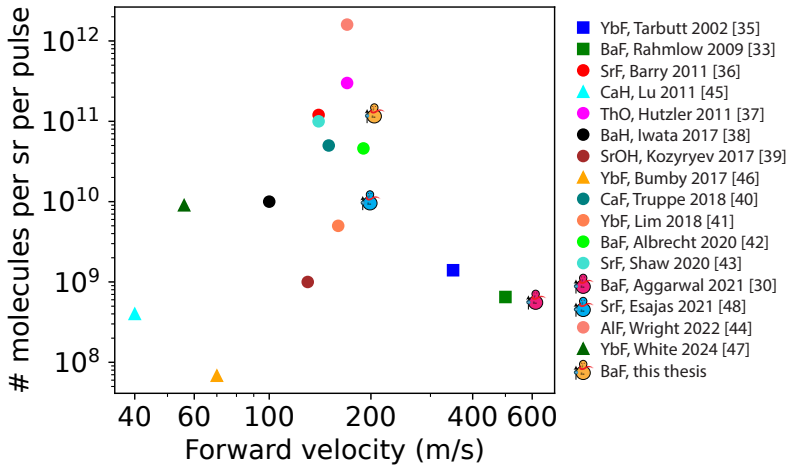

FIGURE 1.3: Overview of molecular sources in terms of brightness per pulse and forward velocity on a double logarithmic scale. In squares, rounds and triangles, supersonic sources [33, 35], cryogenic buffer gas cooled (CBGC) beam sources [36–44] and two-aperture CBGC beam sources [45–47] are shown, respectively. The 'snowman' symbols highlight the sources developed within the NL-*e*EDM collaboration [30, 48].

at relatively high temperature and provide relatively fast beams. Single-stage cell cryogenic sources provide bright beams with velocities of typically ∼150-200 m/s. A large variation of brightness is visible, which is partially due to the chosen optimisation for brightness or low velocity. The highest brightness is obtained for beams of relatively stable molecules such as ThO and AlF that have a $^1\Sigma$ ground state, while a lower brightness is observed for radicals such as BaF and SrF. Lower velocities are obtained by two-stage sources, but at the cost of reduced brightness. These sources attempt to have the best of both worlds by having a first cell containing a large-density buffer gas to efficiently capture the molecules, combined with a second cell containing a low-density buffer gas to create a slow effusive beam. Maintaining a proper balance is crucial, and first attempts resulted in beams of relatively low brightness. Recently, however, promising results have been presented by White *et al.* [47], where a similar brightness was found for the single- and two-stage source.

For the NL-*e*EDM we have designed and constructed three beam sources, indicated by a pink, lightblue, and orange snowman in Figure 1.3. Aggarwal developed a supersonic beam source for BaF molecules [30]. Esajas constructed a cryogenic source for SrF and BaF molecules [48], which is used to test and optimise the travelling wave Stark decelerator and transverse laser cooling. The third source, constructed primarily to understand and optimise the source itself, is described in this thesis. A fourth source is under construction by Ties Fikkers and will be primarily used to test the formation of

polyatomic molecules such as BaOH.

1.5 Outline thesis

The focus of this thesis is on the design and construction of a cryogenic buffer gas beam source and the analysis of the produced molecular beam of BaF, to achieve a better understanding of the source for the NL-*e*EDM experiment.

In **chapter 2**, a detailed description of the design of the source is given. To investigate the molecular beam, an advanced detection setup is necessary, which is the topic of **chapter 3**. Special attention is given to a reliable and reproducible method for determining the optical frequency used for velocity detection by measuring a Doppler shift. This was achieved by the integration of an optical frequency comb into the setup. After producing and detecting the molecular beam, **chapter 4** presents a careful analysis of the thermodynamic properties of the beam, such as velocity and density. The chapter is concluded with a detailed calculation of the number of molecules in the beam. As the longitudinal velocity is of utmost importance for optimising the brightness of the combination of the beam source and the decelerator, a sophisticated detection method for the forward velocity was developed, which is described in **chapter 5**. In addition to the forward velocity, the method revealed a strong temporal dependence of the forward velocity in the pulse. **Chapter 6** describes a careful analysis of the dependency of the source parameters on the longitudinal phase-space distribution and discusses the origin of it. The thesis is finalised in **chapter 7** with a summary of the main results.

1

Description of the cryogenic source

2

2.1 Introduction

This chapter gives a technical description of the design and performance of the cryogenic buffer gas beam source to produce a cold, slow, and intense beam of barium monofluoride (BaF) molecules.

Introducing molecules into a cryogenic cell can be done, in the case of a high enough vapour pressure, by a capillary [49–53], by laser ablation of a target containing a precursor [36–39, 42, 43, 45, 49, 50, 54–60] or by letting laser ablated atoms react with a donor gas [40, 48, 61, 62].

BaF molecules are radicals, making it difficult to produce a cold gaseous beam of them because they tend to react to BaF_2, the more stable version that also exists as a solid salt crystal. Furthermore, since BaF_2 has a boiling temperature of 2530 K [63], it cannot be easily taken from a reservoir. A method of producing gaseous BaF is to laser-ablate molecules from a BaF_2 salt target. Alternatively, barium atoms, laser

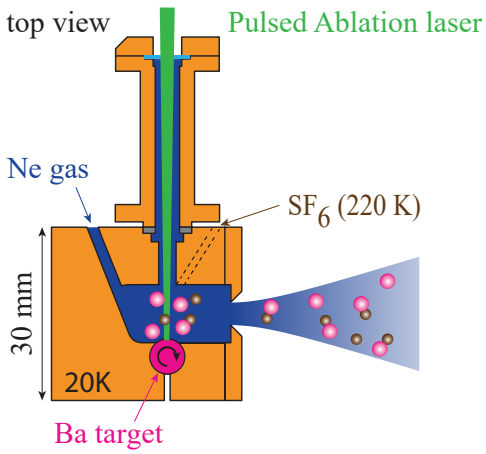

FIGURE 2.1: Schematic overview of the formation of BaF molecules in the cryogenic buffer gas cell. Barium atoms are laser ablated from a rotating solid target and react with sulfur hexafluoride molecules that are injected from the side. The molecules cool by collisions with neon gas that flows through the cell continuously. Entrained in the buffer gas, the molecules are extracted from the cell to form a diverging beam of cold molecules.

ablated from a solid barium metal, can react with a fluorine-containing gas. In our setup, we use a metal target, as it seems to give more and longer stable yield compared to the salt target [48] while producing less dust that contaminates the inside of the cell [56]. In most of the experiments, we use SF_6 as a fluorine donor gas, but recently promising results have been shown for NF_3 as a donor gas [44, 62], and we have also tested this gas to produce BaF molecules.

The process by which cold BaF molecules are formed consists of four major steps, as shown schematically in Figure 2.1. (1) Barium atoms are laser ablated from a solid target by a short laser pulse. (2) These atoms react with sulphur hexafluoride (SF_6) molecules to form BaF. This takes place inside a copper cell that is cooled to typically 20 K and through which the neon buffer gas flows continuously. By collisions with and entrained in the neon buffer gas, the BaF molecules (3) thermalise with the cold neon and (4) are extracted from the cell to form a cold beam of BaF molecules. The design of the cryogenic cell as described in the following was copied from Truppe *et al.* [40] and the design of the rest of the setup is based on the design of Esajas [48].

Note that the species of buffer gas can have a major influence on the design of the source. Typically, helium or neon is used, because of the high vapour pressure at low temperatures. Using helium and neon, a cell temperature below 4 K [40] and 20 K [37] can be achieved, respectively. As in general two-stage cryocoolers use helium as a cooling gas and consequently they can reach a minimal temperature $\sim$4 K, cryopumping neon is easily achieved through all the cold components surrounding the cell, while for helium cryopumping is more difficult due to the low sticking probability of helium at that temperature and the use of charcoal is necessary [64]. Due to the technical advantage of neon, we thus chose to build a setup that uses neon as buffer gas.

Section 2.2 describes the cryocooler and vacuum system that are necessary to cool the copper cell and to maintain a low backing pressure despite the continuous flow of buffer gas. Section 2.3 describes the tubing and control system that provides a continuous flow of neon buffer gas and SF_6 through the cell. In Section 2.4, the rotating barium target and the ablation laser are described.

2.2 A cold setup in vacuum chambers

2.2.1 Vacuum chambers and cryocooler

The vacuum system consists of three vacuum chambers; see Figure 2.2. The molecules are produced inside the 'source' chamber. This chamber is pumped by a 520 l/s turbo pump (Pfeiffer TMU 521 Y P). The molecules are detected in two other vacuum chambers that are collectively pumped by a second turbopump (Pfeiffer TMU 621 P,

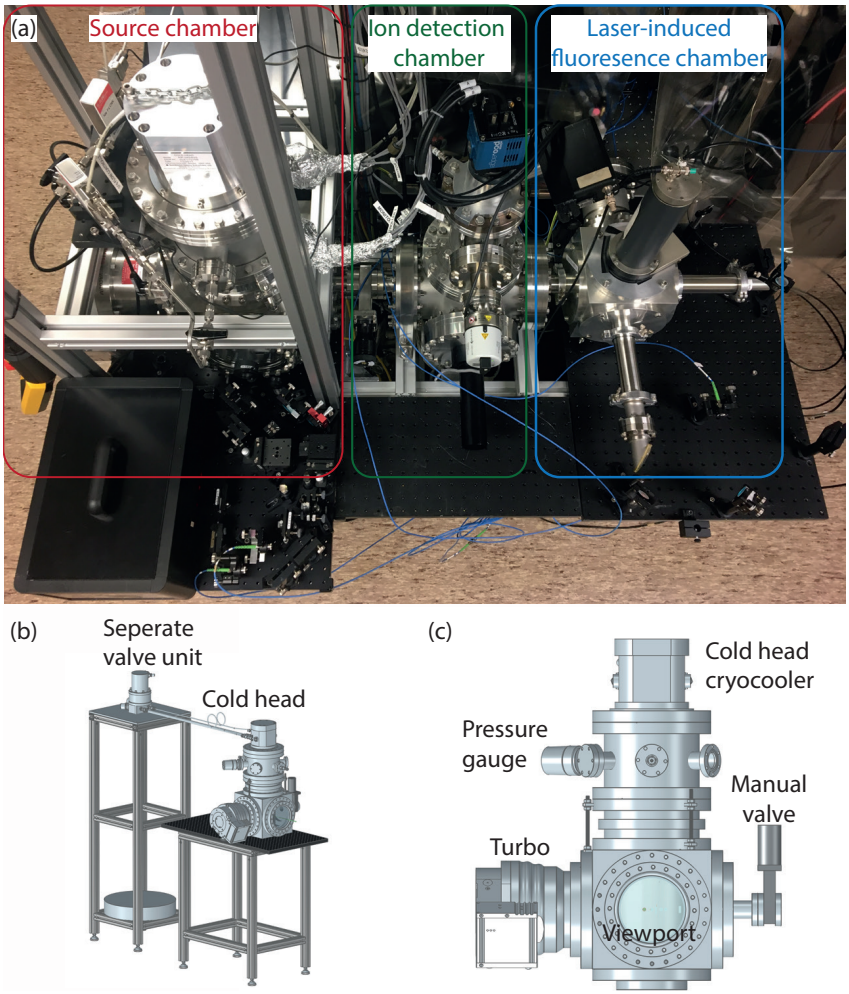

FIGURE 2.2: Overview of the vacuum chambers and cryocooler. On the left hand side is the source chamber, in the middle is the chamber that is used for ion detection and on the right hand side is a chamber where laser-induced fluorescence detection is performed. (b) Schematic drawing of the source chamber and cryocooler, with the cold head of the cryocooler attached at the top and the separate valve unit. (c) Schematic drawing of the source chamber together with the manual valve that is placed between the source chamber and the detection chambers.

520 l/s). The first chamber is used for ion detection, while the second is used to perform laser-induced fluorescence detection (see Chapter 3 for more information on these detection methods). The cold head of the cryocooler (Sumitomo Heavy Industries, cold head RP-082B2S) is attached to the top of the source vacuum chambers; see Figure 2.2(b). The cryocooler has a valve unit that is separated from the cold head to reduce vibrations. A manual gate valve is placed between the source chamber and the detection chambers to allow the source chamber to be vented while maintaining a low pressure in the detection chambers; see Figure 2.2(c). The laser beams that are used for ablation of Ba atoms and absorption detection of BaF molecules enter and exit the source chamber through two large viewports (Hositrad HHVP-6000) located on the sides of the source chamber. The detection chambers contain several small windows, placed at Brewster angle, for multi-photon ionization and laser-induced fluorescence.

The pressures in the source and ion detection chambers are monitored by two vacuum gauges: a full range gauge (Pfeiffer PKR 251) for the source chamber and a cold cathode gauge (Pfeiffer IKR 251) for the detection chambers. Together with two prevacuum pressure gauges (not visible in Figure 2.2), the recorded pressures are saved on the lab computer every 5 seconds. Additionally, the recorded pressures are added to the measurement data shot-to-shot. Although the pressure is not a critical source operation parameter (in contrast to the cell temperature or gas flow rates), recording the pressures provides useful information about the stability and operation condition of the source during measurements.

2.2.2 Inside the source chamber

The cold head consists of two cooling stages (Figure 2.3). The first and second stages reach temperatures of ~ 30 K and ~ 4 K, respectively. A cylindrical shield that is sealed at the bottom is at the top attached to each cooling stage. The outer shield (Figure 2.3(b)), a 335 mm long (divisible halfway) and 5 mm thick aluminium shield with an inner diameter of 70 mm, is attached to the first cooling stage. It prevents hot background gas and black body radiation from reaching the colder inner parts of the setup. The inner shield (Figure 2.3(c)) is a 101 mm long and 1.5 mm thick oxygen-free copper cylinder with an inner diameter of 55 mm which is attached to the second cooling stage. Its main function is to act as a pump for the neon buffer gas.

The cell, machined from oxygen-free copper, is attached to the second cooling stage (Figure 2.4). The cell has an outer dimension of 30 mm and an inner bore diameter of 10 mm, which is partly sealed by an aperture attached to the cell. In all experiments presented in this thesis, an aperture with a conical hole with a minimal diameter of 4.5 mm was used, but the exit can be interchanged to adjust the buffer gas cooling properties and extraction efficiency of the cell. The cell is placed inside the inner shield

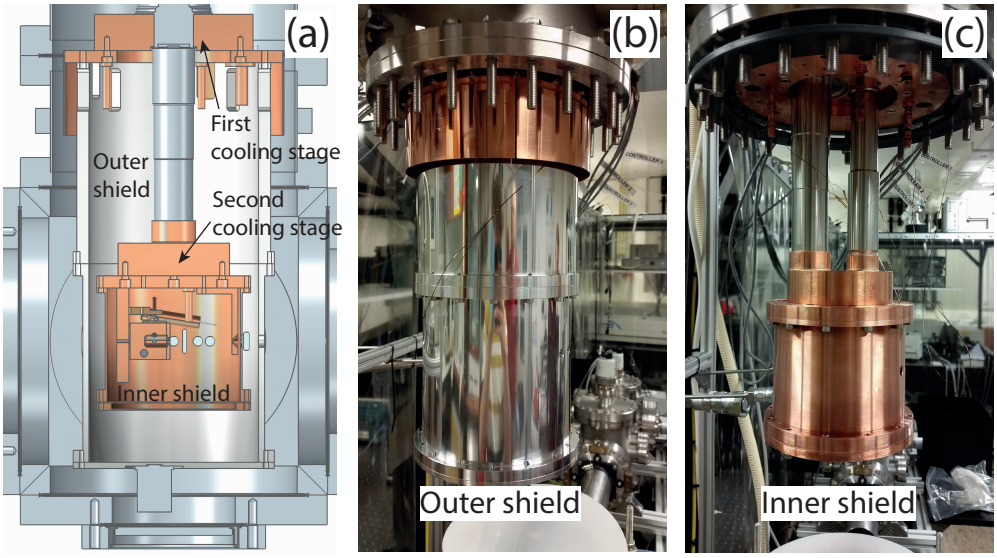

FIGURE 2.3: Cryocooler with cooling stages and shields. (a) Schematic drawing showing the outer and inner shield and their connection to the first and second cooling stages of the cryocooler, respectively. (b) Picture of the outer shield and (c) picture of the inner shield.

in such a way that the aperture is approximately in the middle of the shield, which means that there is plenty of room to the front of the aperture for adjusting the cell length and aperture. For some measurements, we have extended the inside length of the cell by placing one or two 10 mm thick copper plates, with the same 10 mm diameter hole as the cell, between the cell and the aperture.

The cell is fixed on a vertical copper plate that is attached to the mounting plate of the second cooling stage. Because neon is used as a buffer gas, the cell is kept at a temperature of $17 - 20$ K, while the second cooling stage of the cryocooler is cooled to $\sim$4 K. Therefore, the cell is thermally isolated by four 1 mm thick rings of stainless steel with a surface area of 130 mm^2. Stainless steel has a much lower heat conductivity than copper [65]. Due to the heat load of the elements connected to the cell, the cell temperature stabilises at $\sim$11 K and with active heating ($\sim$0.3 W) the cell is stabilised at the desired temperature of 17-20 K, while the second cooling stage heats up to no more than 5-6 K.

Holes in the shields are unwanted because they add to the heat load on the cell (radiative heating) and gas escaping the efficient cryo pump of the inner shield. However, a few holes are necessary. There is an aperture on the front side of the shields through which the molecular beam expands (Figure 2.4). Originally, this aperture had a diameter of 10 mm, but this lead to an increase in the pressure in the detection chamber to $\sim 1 \times 10^{-5}$ mbar. We therefore placed an extra copper aperture with a

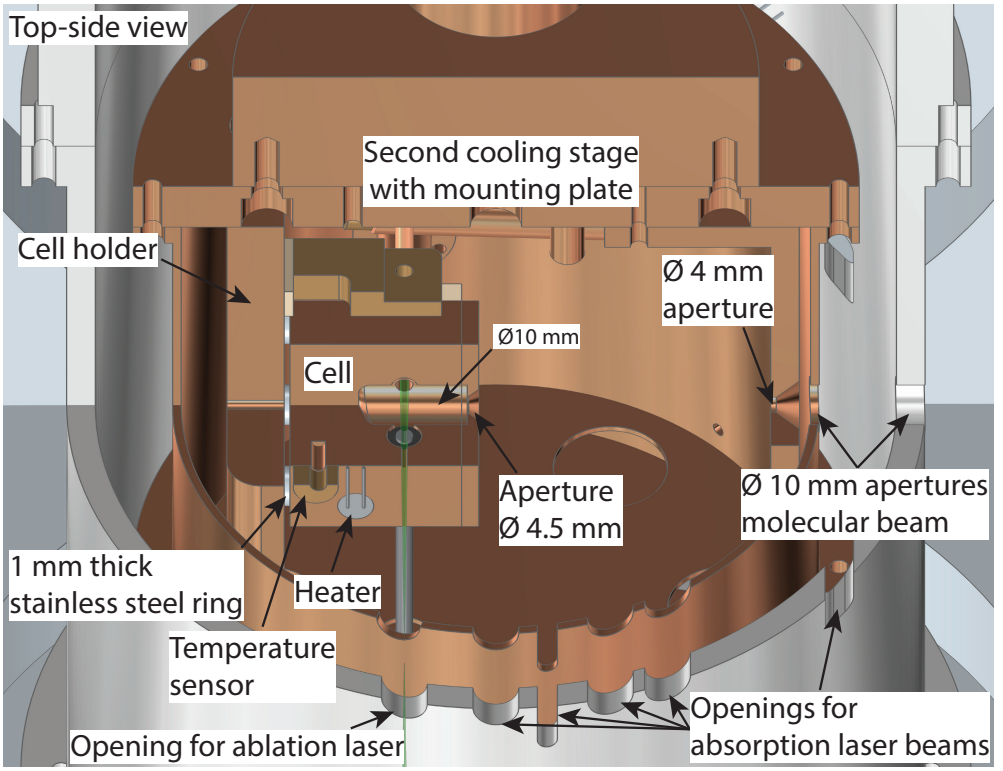

FIGURE 2.4: Schematic drawing of the inside of the inner shield. The cell is attached to the second cooling stage of the cryocooler via a copper plate and stainless steel rings. The molecular beam is extracted via a 4.5 mm diameter aperture. It exits the shields via 10 mm diameter apertures. Extra skimming of the beam is performed by placing a 4 mm aperture just before the hole in the inner shield. Other openings on both sides of the shields allow access to the source with the ablation laser and detection of the molecular beam through the absorption of laser light.

4 mm diameter before the inner shield aperture. It is mounted on the second cooling stage and has the same temperature as the inner shield[1].

The holes for introducing the ablation laser are located on each side of the inner shields (Figure 2.4). Furthermore, there are a number of apertures on each side to allow absorption laser beams to cross the molecular beam, namely in the middle of the shield, 9, 20, 30 and 60 mm further to the front, the opening at 60 mm is only in the outer shield. The 9 and 60 mm openings are vertically stretched to be able to measure the distribution of the molecular beam along the vertical direction.

The temperatures of the cell, the second cooling stage and the SF_6 tube (discussed in detail in Sec. 2.3.2) are measured with silicon diode sensors (Cryo-con S950-BB) and stabilised by a controller (Cryo-con 26-C) that drives currents through resistive

[1]The advantage of having the aperture at lower temperature is that it effectively prevents neon being back-scattered into the beam. The disadvantage is that frozen neon may clog the aperture [37].

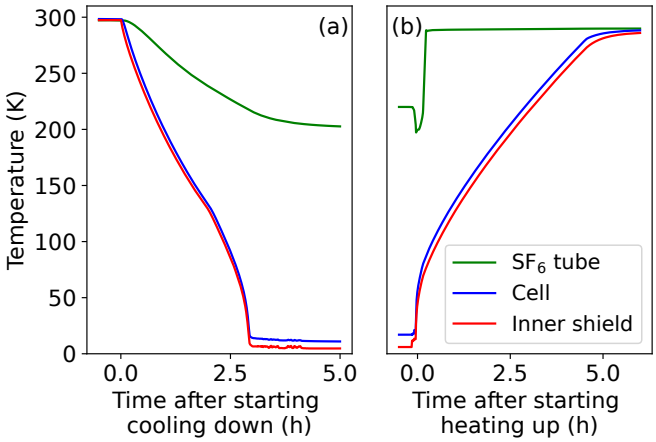

FIGURE 2.5: Temperature as a function of time for (a) cooling down and (b) heating the setup. In green, blue and red the temperature of the SF_6 tube, the cell and the inner shield.

elements, so-called 'heaters' (Cryo-con cartridge heater 3039-001). Most parts of the setup are made of oxygen-free copper, which has a very high thermal conductivity. All parts are kept as light as possible, especially the relatively large shields, to reduce the heat capacity of the system, and thereby reduce the required time to cool and heat up the setup. Cooling the setup takes about 3 hours, while heating up the setup takes about 5 hours (Figure 2.5). The relatively long time needed to heat the source is mainly due to the lack of a heating element in the outer shield. Since the setup is usually heated up overnight, this is not an issue. The temperatures are stored every 5 s and shot to shot included in the measurement data.

2.2.3 Temperature cycle to evaporate frozen neon buffer gas

The inner shield acts as an efficient pump for the continuous flow of the neon buffer gas. During operation, a layer of neon builds up that needs to be removed. Therefore, the setup is heated up every few days. This is usually done overnight, leaving the system ready for new measurements the next day. A connection to the cryocooler in the temperature control interface allows us to set a timer for turning off the heaters and starting the cryocooler. Typically, the scheme shown in Figure 2.6 is followed, which consists of four steps. In (a-d) the temperature of the inner shield and in (e-h) the pressure in the source chamber is shown.

Due to the neon that is released, the pressure in the source chamber rises to $\sim$1 bar, which is too high to keep the turbo running. Therefore, the first step is to turn off the turbo, which is currently done manually. At a pressure of $< 1 \times 10^{-7}$ mbar, the

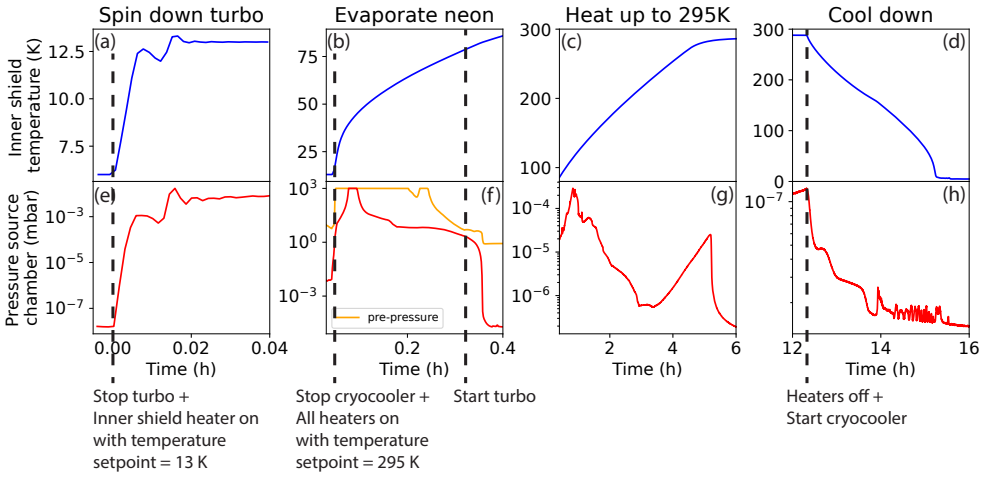

FIGURE 2.6: Heating and cooling cycle to evaporate frozen neon buffer gas. (a) First the turbo is stopped, to avoid damage during the heating process. (b) The setup is thereupon heated, which leads to the evaporation of the neon buffer gas. Within 15 minutes most frozen neon gas is evaporated and the turbo is started again. (c) To 'reset' the source, the setup is heated to room temperature. (d) After a pre-determined time, the heaters are automatically stopped and the cryocooler is started. Below each temperature graph, the corresponding pressure in the source chamber is shown. Note that the pressure curve in (e) matches the temperature curve in (a). During the first heating stage, shown in (b), the pressure drops, while during the second heating stage, shown in (c), the pressure fluctuates wildly (g). After starting the cryocooler, both temperature and pressure drop ((d) and (h), respectively).

turbo will spin down very slowly. We speed up the process by gently heating the inner shield (Figure 2.6(a)) to 13 K with a maximum heating power of 0.5 W, resulting in a moderate increase in pressure (e). This usually takes about 10 minutes (somewhat faster in the example shown in Figure 2.6).

Once the rotation speed of the turbo is below 10%, the cryocooler is turned off and all heaters are switched to 5 W, leading to a strong increase in cell temperature, SF_6 tube and inner shield (b). As a consequence, all neon is evaporated and the pressure is increased to $\sim$1 bar (f). Meanwhile, the prevacuum membrane pump remains running and after about 15 minutes the pressure decreases again. As soon as the prevacuum pressure is below 5 mbar, the turbo is turned on and the pressure in the source chamber quickly drops to below 1×10^{-5} mbar.

During the rest of the evening, the temperature of the setup is increased to room temperature (c) and remains at that temperature until a fixed time when the heaters are switched off and the cryocooler is restarted. This will return the setup to cryogenic temperatures in a few hours (d). Although the pressure fluctuates wildly during the cycle (g), it remains below the maximum pressure allowed by the turbopump.

2.3 Tubing system for neon and fluor-containing gas

The flow rates and temperatures of the gasses that are introduced into the source need to be accurately controlled. Here, the design and motivation for the main components of the gas supply are described.

To control the gas flow, three mass flow controllers are installed, which are placed between the gas cylinder and the vacuum throughput. The neon flow rate is controlled by a mass flow controller (Bronkhorst El-Flow prestige FG-201CV-AAD-22-E-DA-000) with a maximum flow rate of 70 SCCM[2]. The controller (El-Flow prestige FG-200CV-AAD-11-E-DA-000) for SF_6 gas has a maximum flow rate of 1 SCCM. As alternative fluorine donor gases, CF_4 and NF_3 could be used, and NF_3 we have briefly tested. Unfortunately, NF_3 and CF_4 are chemically incompatible with the EPDM sealing of the SF_6 flow controller, and thus a third controller (El-Flow prestige FG-200CV-AAD-22-K-DA-000, maximal 0.4 SCCM NF_3) was installed parallel to the SF_6 controller. As we have used SF_6 in almost all measurements, I will refer to the fluorine donor system as the 'SF_6' tube/controller, etc. To be able to remove residual air and refresh the gas, all tubes between the gas cylinder and the flow rate controllers and between the controllers and the vacuum chamber are connected to a membrane pump via a manual valve.

The vacuum throughputs are Swagelock VCR connections soldered onto a CF40 flange. Inside the vacuum, the neon tube has an additional VCR connection. We chose specifically for the VCR connections, because all parts closing the connection, including the gasket, are made of stainless steel and thus have the same thermal expansion, avoiding leakages in the tubes due to cooling down and heating up the setup.

2.3.1 Neon gas tube

Figure 2.7 shows three pictures of the setup, with text that highlights the neon and SF_6 components. To achieve a cold beam of molecules, the neon gas is precooled in two steps in the tube before it enters the cell. After the vacuum throughput, the first part of the neon tube is made of stainless steel, which has a relatively low thermal conductivity [66], allowing for a large temperature gradient. Subsequently, the tube is cooled to the temperature of the first stage of the cryocooler ($\sim$30 K). For efficient thermalisation, this part of the tube is made of oxygen-free copper and is wound several times around a post connected to the cooling stage. Continuing towards the cell, again a part of the tube is made of stainless steel to avoid heat load on the cell. Here, Swagelock VCR connections are placed to be able to insert the tube in the setup. The last part of the tube towards the cell is again made out of copper and spiralled

[2] 1 SCCM = 4.48×10^{17} particles s^{-1}.

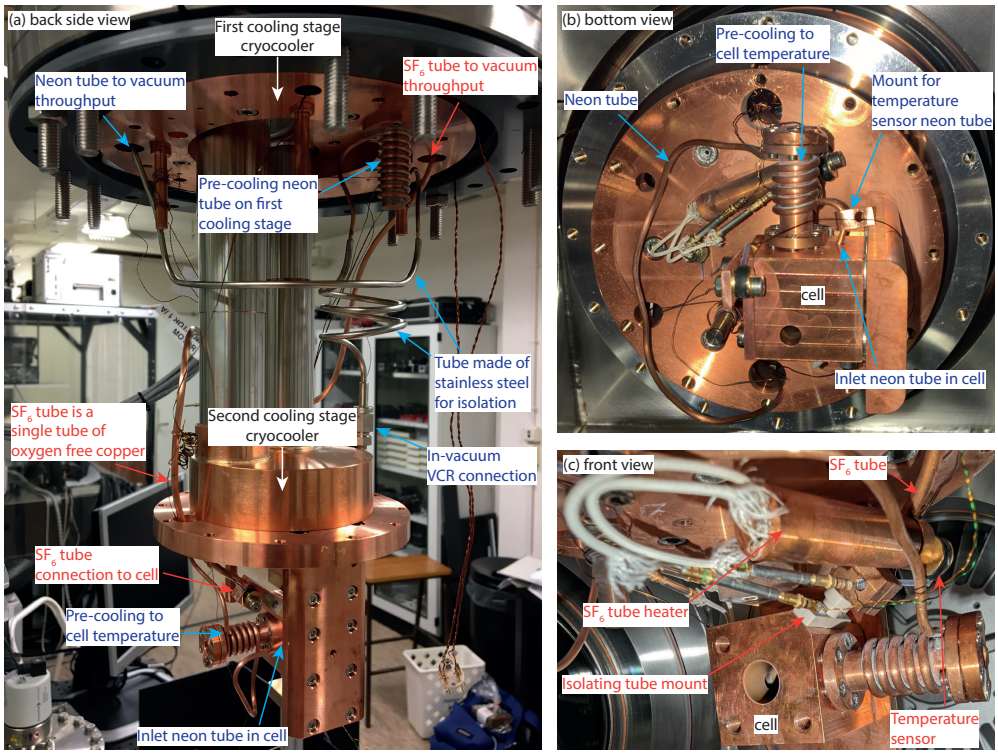

FIGURE 2.7: Pictures showing the neon and SF_6 tubes inside the source. The neon tube is pre-cooled in multiple steps while it runs from the top flange to the cell (bottom). The SF_6 tube is made out of one piece of copper. (a) The tubes between the first and second cooling stages. (b) The neon tube below the second cooling stage to the cell. (c) The SF_6 tube is injected into the cell.

around an extension tube attached to the cell to thermalise to the cell temperature; see Figure 2.7(b). I will refer to the extension tube as the 'snorkel'. Immediately after passing through the spiral, the gas is injected into the cell.

Unfortunately, the tubing system did not work as well as hoped. After operating the source for typically 5-20 hours, depending on the flow rate and temperature, the flow will slowly drop, resulting in lower pressure in the source chamber and reduced signal of the molecular beam. When the system was subsequently heated up, the pressure increased abruptly after some time. Our hypothesis is that, although the temperature of the tube remains above 20 K, the neon gas freezes inside the last part of the tube, just before the inlet of the cell. At this position the temperature is comparable to that of the cell, while the pressure is above that of the cell (as the net gas flow is towards the cell). At temperatures between 15 and 20 K, the vapour pressure of neon is 0.5 to 40 mbar [67], while the pressure inside the cell is estimated to be $\sim$0.1 mbar. Deformations in the tube can lead to pressure gradients causing the pressure to exceed

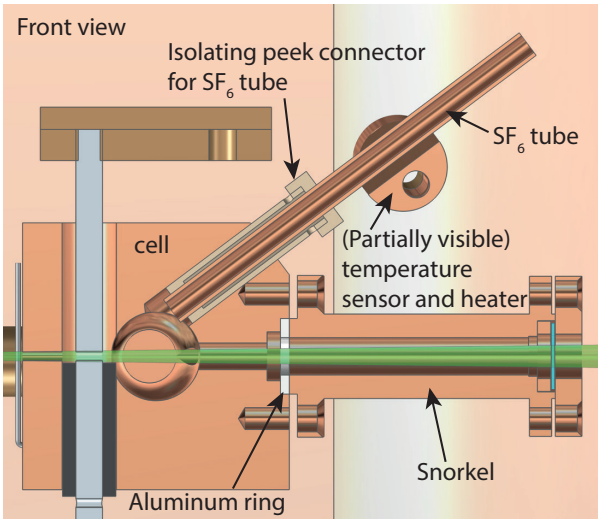

FIGURE 2.8: Front view with cut through of copper cell, snorkel and SF_6 tube insertion into the cell. The SF_6 tube is thermally isolated from the cell via a connector made out of PEEK. To reduce the freezing of neon, the neon pre-cooling snorkel is slightly thermally isolated from the cell with a 1 mm aluminum ring.

the vapour pressure locally. This leads to a build-up of solid neon inside the tube, clogging the tube, and ultimately stopping the gas flow. When heated up, the frozen neon evaporates and the gas accumulated in the tube is released at once, causing the pressure in the vacuum chamber to spike.

To address the neon tube freezing, ideally, a new neon tube with a larger inner diameter should be installed. However, as a quick fix, we have reduced the pre-cooling before the cell slightly by reducing the thermal conductivity between the cell and the snorkel with the spiral wound around it. Instead of direct contact between the two copper parts, a 1 mm thick aluminium ring, with lower thermal conductivity than copper [68], is placed in between, see Figure 2.8. To monitor the temperature of the tube, a sensor was placed on the $\sim$3 cm long tube from the helix to the cell (see Figure 2.7(b)). Before installing the extra ring, the tube had the same temperature as the cell, while afterwards, the tube was approximately 0.2-0.5 K warmer, dependent on the temperature of the cell and the neon flow rate. As a result, the source could be operated for a longer time and higher flow rate and lower temperature before becoming clogged. The intensity and velocity distribution were unaffected by the slightly increased temperature of the neon gas when entering the cell.

2.3.2 SF_6 gas tube

As SF_6 has a low vapor pressure below 200 K [3], the SF_6 line is designed differently than the neon tube. Originally, we planned to keep the temperature of the complete tube above 200 K only by heat conduction from the vacuum flange, which is at room temperature, towards the other end of the tube that is connected to the cell, using a relatively large (2 mm inner diameter) and thick (0.5 mm) oxygen-free copper tube, see Figure 2.7(a). Figure 2.8 shows how the tube is inserted into the cell but thermally isolated from the cell using a PEEK connection part, which has a low thermal conductivity at cryogenic temperatures [70]. The minimal temperature just before the cell is about 200 K, which means the passive heating works and the thermal isolation to the cell is sufficient. For additional control and better reproducibility of the temperature, we later attached a heater and temperature sensor to the tube to actively stabilise the temperature at 220 K, see Figure 2.7(c). As visible in Figure 2.8, the SF_6 is injected at an angle above the ablation laser alignment, diagonally opposite the Ba target. The distance from the opening to the aperture is the same as that of the Ba target to the aperture.

The low vapour pressure of SF_6 limits the minimal injection temperature of the molecules to $>$200 K and consequently it heats the buffer gas inside the cell. Other gases, such as NF_3 and CF_4, with similar vapour pressures at lower temperatures [71], could potentially be used as a fluorine donor gas for BaF. For NF_3, an injection temperature of 120 K has been reported [44]. To reduce the passive heating, currently limiting the injection temperature to $>$200 K, the tube should be thermally isolated from the vacuum flange.

2.4 Barium atoms

The barium atoms are laser ablated by a focused 10 Hz, 5.4 ns Nd:YAG laser (Spectra-Physics Quanta-Ray GCR-12S) that is frequency-doubled (Quanta-Ray HG-2) to 532 nm. The pulse energy used in the experiments is 4-12.5 mJ, (measured outside the vacuum). The pump energy is varied by changing the timing of the Q-switch relative to the flashlamp timing, which ensures that the laser beam properties are not affected. After filtering out residual 1064 nm light with two dichroic mirrors, a 6 mm diameter top hat beam is focused by a $f = +250$ mm lens into the vacuum chamber, see Figure 2.9(a). The lens is mounted on a translation stage, so that the position of the focus can be tuned over a distance of 50 mm and consequently the effective spot size on the target can be tuned. Typically, the focus lies about 44 mm behind the barium target, which results in a target spot size with a diameter of about 1 mm.

[3] The boiling point of SF_6 is 209.3 K [69].

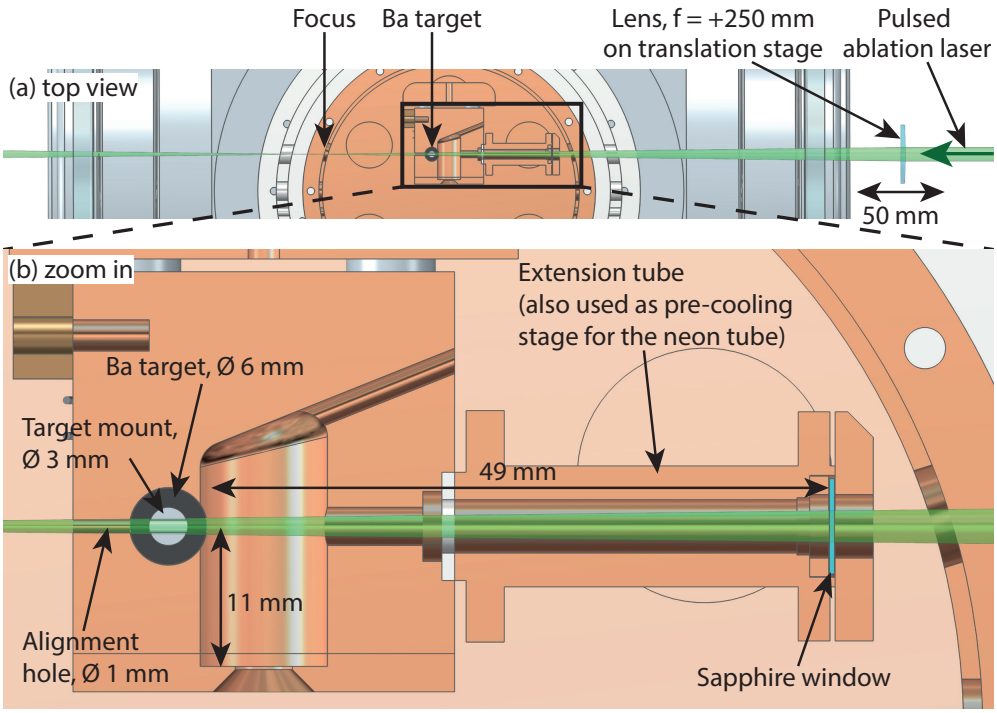

FIGURE 2.9: Alignment of the ablation laser and position of the barium target. (a) The ablation laser is focused behind the target and the position can be tuned to tune the effective size of the beam on the target. (b) Zoom in showing the cylindrical barium target in the cell.

To avoid buffer gas leaking out of the cell, the aperture through which the ablation laser enters the cell is sealed off by a small window; see Figure 2.9(b). The window is made of sapphire (Edmund Optics 7.5 mm diameter, 0.4 mm thick, uncoated), which is able to resist the heat load and thermal stress induced by the short energetic laser pulse. Reflections of the vacuum and sapphire windows are estimated to attenuate the ablation light by about 20%. Ablation of barium leads to dust, which is partially deposited on the window. To minimise the amount of dust on the window, it is placed at the end of a tube attached to the cell at a distance of 49 mm from the target. This tube is also used as the second cooling stage of the neon tube, the so-called 'snorkel', discussed before. A cylindrical barium target is positioned on the side of the cell. For the standard cell without extension, the distance from the target to the exit is 11 mm. The barium target has an inner and outer diameter of 3 and 6 mm respectively and is glued on a 3 mm diameter cylindrical target mounting axis. Behind the target, there is a hole with a diameter of 1 mm, which may be used to align the ablation laser when the target is not in place.

Typically, the molecular yield drops rapidly if ablation occurs from a single target

spot. For example, in the case of ablation of SrF_2, the molecular yield was seen to decrease by a factor of 2 after 500 to 1000 shots [36] and for the ablation of ThO_2 the yield decreased by a factor of 2 after 30000 shots [37]. To avoid this effect, the ablation spot on our target is changed from shot to shot by rotating the target and simultaneously moving the target up and down. In this way, a much larger area of the target is used. This leads to a stable signal, and the ablation yield is currently not the limiting factor for the stability of the molecular flux signal.

Figure 2.10(a) shows the complete rotation system, and in (b) and (c) details of different components are shown. (a) A small stepper motor (Phytron VSS32.200.1,2-UHVC2-4Lp), which is designed to operate in vacuum and at cryogenic temperatures, is attached to the bottom of the outer shield. At the bottom of the vacuum chamber, a CF100 viewport is installed, through which the motor rotation is monitored. (b) On the inside of the shield, the rotating motor axis is connected to a cylindrical 'guide' that has in the vertical direction a 3 mm diameter hole and a 1 mm thick slit. The part is made out of PEEK to thermally isolate the motor from the rest of the system. The target mounting axis is a solid stainless steel cylinder with a diameter of 3 mm, with at the bottom a 1 mm thick and 10 mm long 'slider', that is inserted in the slide of the guide. By means of the slider, the axis is forced to follow the rotation of the motor, while it is free to move in the vertical direction. (c) The top 25 mm of the mounting axis, has an M3 thread, and is screwed into a fixed holder so that if the motor is rotating, it will move up or down inside the threads, moving the target up or down. To reduce friction, the holder is made of brass. Brass does not react with the stainless steel axis, as aluminium would do, and is harder than copper, and thus more suitable for being used as a thread. The axis holder is connected to the cell holder, but is thermally isolated from it via a 1 mm thick plate of PEEK. This prevents the target from cooling to the second cooling stage temperature, which would mean that neon would freeze on it. In the future, the system may be improved by connecting the axis holder directly to the cell, without thermal isolation to avoid the target from heating up. Note that the thread is above the target, which is essential for reliable operation. An earlier design which had a thread below the target required frequent service because dust produced by the ablation would fall into the thread and increase the friction on the system until the motor would get stuck.

Figure 2.10(d) shows a picture of the barium target glued to the mounting axis after being used for a couple of days. A large area of the target is used for ablation. Because the effective spot size of the laser on the target turns out to be smaller than the pitch of the threading on the mounting axis, a threaded structure is ablated from the target. Ideally, for the most homogeneous ablation of the target, the spot size is (more than) two times the pitch.

Although the rotation of the motor can be seen from outside the vacuum chambers,

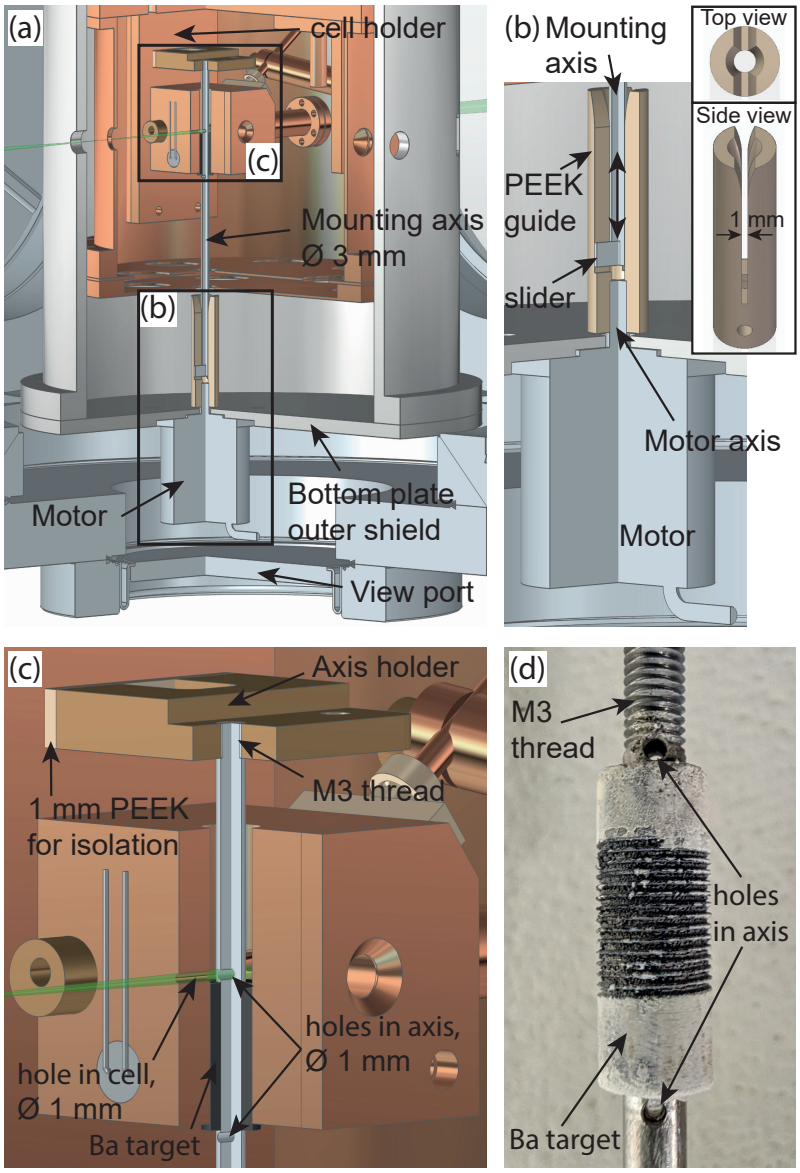

FIGURE 2.10: Drawings of the system to rotate the barium axis. (a) Overview of the complete system, with the motor attached to the bottom of the outer shield. (b) Zoom in on the lower part of the system, showing the connection, made out of PEEK, between the motor and the target mounting axis. (c) Zoom in on the top part of the system where the mounting axis is screwed onto the axis holder to move the target vertically if the axis is rotated. (d) Picture of a target after being used several days.

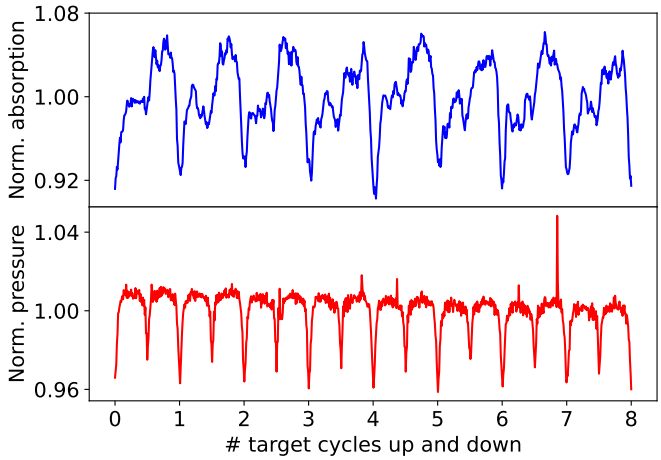

FIGURE 2.11: Molecular signal and vacuum pressure as a function of time. A repeating drop in signal and pressure is visible when the target is moved too far up or down. At those positions, buffer gas and molecules are leaking via the target shaft, because the diameter of the target axis is smaller than the diameter of the target.

the view of the vertical position of the target (holder) is blocked by the shields. To be able to derive the position without breaking the vacuum, two holes were drilled into the mounting axis. These holes have a diameter of 1 mm, are separated by 16.5 mm and are placed above and below the target; see Figure 2.10(c) and (d). If the mounting axis is rotated up or down until one of the holes overlaps with the alignment hole in the cell, some light of the ablation laser is transmitted and visible outside the vacuum chamber. An additional benefit of the holes in the axis is that these holes allow for optimising the alignment of the ablation laser while the target is in place.

The barium target fits snugly in the cylindrical shaft in the cell, while the stainless steel rod has a much smaller diameter. This means that, when the target is moved too far up or too far down, buffer gas is partially leaking out of the cell via the target shaft and less gas is leaving the cell via the aperture in the direction of the molecular beam. Consequently, when the target is translated up and down over a wide range, the molecular signal decreases around the turning points, as seen in Figure 2.11(a). The fact that this effect is related to the buffer gas that is leaking through the shaft is corroborated by the fact that the pressure in the source chamber is decreased when a minimum of signal is observed; see Figure 2.11(b). Gas that leaves the cell through the aperture has a relatively high chance of leaving the shields without freezing to it because the apertures in the shields are in the direction of the molecular beam. In contrast, gas that leaks through the target shaft will likely freeze onto the inner shield, resulting in a lower pressure in the vacuum chamber. We avoid this effect by using the

middle part of the target only, see Figure 2.10(d). In order to use the full length of the target, we would need to increase the diameter of the mounting axis just above and below the target to the same diameter as the Ba target.

Typically, the stepper motor is programmed to rotate 15 rounds up and down repeatedly. In order to quickly average out shot-to-shot fluctuations due to target inhomogeneities, the target is rotated at relatively high speed (30 rpm) resulting in a short period (60 s). The great reliability of the stepper motor ensures that even after several months, the height of the target showed no offset or drift.

This concludes the description of the source that is used to produce the cryogenic beam of BaF molecules. The next chapter will describe the detection setup to measure the properties of the beam.

2

Detection methods

3

3.1 Introduction

In the previous chapter, the mechanical design and some characteristics of the cryogenic buffer gas beam source were described. In this chapter, I will describe the optical setup, i.e. lasers, optical beam paths, and detection, that are used for detecting BaF molecules and determining essential properties of the molecular beam.

In this work, three detection techniques have been employed; (1) direct absorption, (2) multiphoton ionisation (MPI), using femtosecond laser pulses, and (3) laser-induced fluorescence (LIF).

Absorption detection was used to determine the density and brightness of the molecular beam and to measure the transverse velocity distribution. Absorption is relatively insensitive and requires a high (column) density. Because of the divergence of the beam, the density of molecules drops quickly as a function of the longitudinal distance. Therefore, absorption detection can only be used inside the cell or close to the cell exit. The main advantage of absorption detection, however, is its straightforward interpretation to retrieve the column density and the fact that it requires access for a single laser beam only, which is crucial because the cell is hidden deep inside the molecular beam setup, surrounded by heat shields.

Initially, molecules were detected by non-resonant ionisation using femtosecond laser pulses from a commercial laser system consisting of a titanium:sapphire oscillator and a chirped regenerative amplifier [72]. This technique has the advantage that it ionises all atoms and molecules in the beam which are mass selectively detected using a combination of a linear time-of-flight and a microchannel plate detector. Some preliminary measurements were made using this system, showing ion peaks at the expected masses for barium, barium-fluoride, neon, and (fragments of) sulphur-hexafluoride. The obvious disadvantage of this method is that it is not state-selective, which makes quantitative analysis additionally complicated, as the multiphoton ionisation cross sections may vary between states. Furthermore, because this method is pulsed, many measurements were necessary to measure a single time-of-flight profile of the molecular pulse. Therefore, we turned to laser-induced fluorescence with the idea of combining the measurements at a later moment. Unfortunately, due to time constraints, systematic measurements have not been performed, and MPI detection will not be discussed further in this thesis.

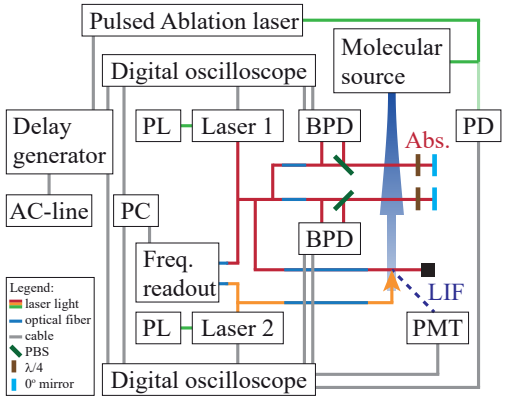

FIGURE 3.1: Overview of the detection setup. Two near-infrared continuous-wave lasers are used for absorption and laser-induced fluorescence (LIF) detection of the molecular beam. The signal, recorded by two balanced photodiodes (BPD) and a photomultiplier tube (PMT), is read out by two digital oscilloscopes and the data acquisition computer (PC). A frequency readout setup is used to read out and digitally lock the laser frequencies, see for more details Section 3.7. A delay generator triggers the ablation laser and the oscilloscopes. The exact configuration and alignment of absorption and fluorescence beams are varied between measurements. Several optical fibers are used to decouple parts of the alignment and to be able to easily change the configuration. The remaining abbreviations stand for: PL = pump laser, PD = photodiode, $\lambda/4$ = quarter waveplate.

Laser-induced fluorescence detection was used to measure the properties of the beam at 780 mm from the source exit, where the molecular beam is too dilute for absorption detection. Due to the limited detection volume, only molecules with a small transverse velocity are detected, resulting in very narrow spectral features. This was used to obtain more precise values for the molecular constants of barium fluoride.

Figure 3.1 shows a schematic of the detection setup. The main components are continuous-wave lasers, an absorption and laser-induced fluorescence detection setup, a data acquisition setup, and a setup to determine the frequencies of the lasers.

3.2 Continuous-wave lasers

For optical detection of the molecular beam, we use several transitions ranging from 791-866 nm. To generate light at these wave lengths, two widely tunable narrowband continuous-wave Ti:Sapphire Coherent 899 ring lasers are used. The two lasers have a different mirror set, resulting in a different accessible wavelength range. One of the lasers, which I will refer to as 'Laser 1', has an optical range from approximately 790 to 890 nm. The other laser, in the following 'Laser 2', spans a range from ∼720 to ∼830 nm. Both lasers are pumped with light at 532 nm from a continuous-wave Nd:YAG laser, Laser 1 by 8 W from a Sprout-G-12W and Laser 2 by ∼6 W from a

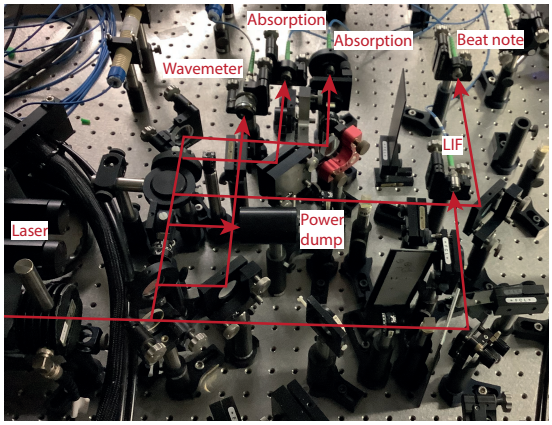

FIGURE 3.2: Picture of the optical setup to align the light of the Laser 1 into the optical fibers.

Verdi V-10. This results in ∼200 mW at 860 nm for Laser 1, and ∼200 mW at 797 nm for Laser 2. By connecting the 'external DC voltage' to the DC voltage generator that is built into the digital oscilloscopes, the frequency can be automatically scanned over a range of 12 GHz.

The emitted laser beams are split up for absorption and laser-induced fluorescence detection, for frequency readout on wavemeters, and for frequency referencing, via a beat note with the frequency comb, see Figure 3.2(b). For tuning the laser power in each beam path, a combination of a half-waveplate and a polarising beamsplitter is used. To decouple the optical alignment of the laser beam emitted by the ring laser from the alignment through the molecular beam, several polarisation-maintaining optical fibers (Thorlabs P3-780PM-FC) are used. For absorption and fluorescence detection, two linked fibers, connected via a mating sleeve (Thorlabs ADAFCPM2), are used. This allows for easily configuring the desired detection scheme, where light from both lasers can be connected to all detection beam paths.

3.3 Setup for absorption detection

Figures 3.3(a) and (b) show a schematic drawing and a picture of the absorption detection setup, respectively. The red and orange lines show two similar beam paths that are used to detect absorption along two paths at a different position along the molecular beam axis. Each of the beam paths is built up as follows: light exiting the optical fiber is split into two beams by a non-polarising beam splitter. The power of one of them is directly measured by one of the photodiodes of a balanced photodiode and is used as the reference signal for the laser power. After passing a polarising beam splitter, the second beam crosses the molecular beam, which is retro-reflected by a zero-degree

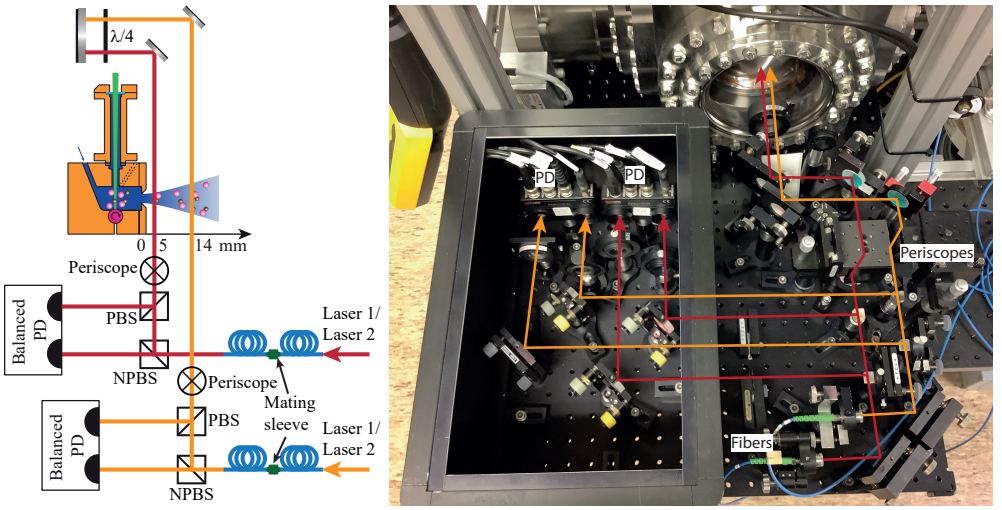

FIGURE 3.3: Absorption setup: (a) schematic overview (b) Zoom in of the picture shown in Figure 2.2.

mirror, and crosses the molecular beam a second time. As the laser beam passes the molecular beam twice, it is attenuated twice because of the absorption by molecules. The polarisation of the retro-reflected beam is rotated by 90 degrees as it passes a quarter-wave plate twice. Therefore, this beam is now reflected by the polarising beam splitter and directed to the other photodiode of the balanced photodiode. The balanced photodiode provides electronic signals for either of the two photodiodes, as well as low noise, ∼28 times amplified differential signal, which is thus very sensitive to attenuation in one of the two beam paths due to absorption of light by molecules. In order to be able to measure the molecular beam size and to optimise the absorption laser height relative to the height of the molecular beam, a periscope is used. As the laser light is retroreflected, the height of the laser through the molecular beam can be adjusted without changing the alignment onto the photodiode.

The exact distance where the laser beams cross the molecular beam can be easily varied. For measuring the divergence, the beams were positioned 5 and 14 mm after the source exit. To determine the rotational and vibrational temperature, the two absorption signals were measured at the same distance from the source exit. In this case, a small angle was introduced in the vertical plane such that both lasers crossed each other at the molecular beam axis. One of the absorption signals was measured at a fixed laser frequency to serve as a reference for the intensity of the molecular beam, while the other laser beam was scanned to address various rotational and vibrational transitions.

The attenuation of the laser light is a measure for the number of photons that are absorbed by the molecules and subsequently re-emitted via spontaneous decay in a

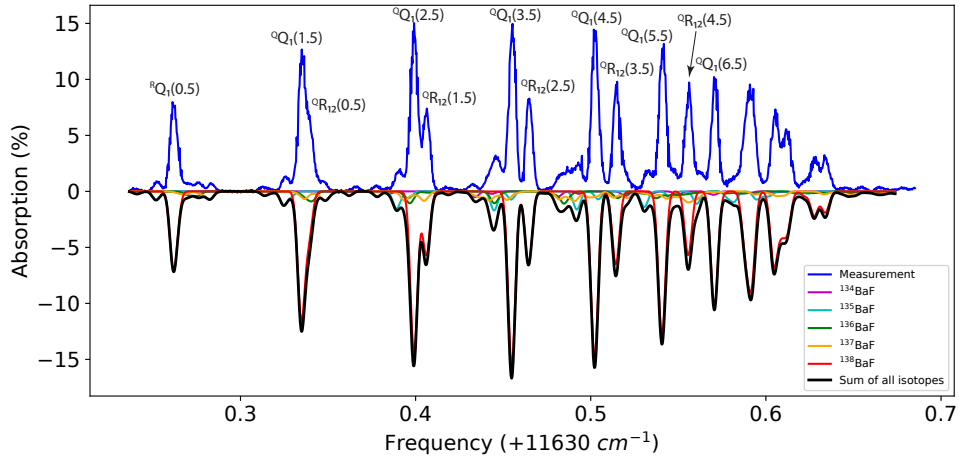

FIGURE 3.4: Absorption measurement and simulation of the ^{Q}Q and ^{Q}R rotational transitions between the vibrational ground states of the $X^2\Sigma^+$ and the $A^2\Pi_{1/2}$ electronic states. The absorption intensity is the time averaged signal over the duration of the pulse.

random direction. If the laser is on resonance, the rate at which molecules absorb photons at a given laser intensity I is given by the scattering rate R [73]:

$$R = \frac{\Gamma}{2}\frac{I/I_s}{1 + I/I_s}, \tag{3.1}$$

with $\Gamma = 1/\tau$, with τ being the natural lifetime of the transition, and I_s the saturation intensity of the transition, where we have left out the terms for a detuned laser frequency. As an intensity-dependent absorption signal complicates the analysis, the intensity is kept well below the saturation intensity.

In the absence of hyperfine, rotational or vibrational splitting, the saturation intensity for the $X \rightarrowtail A^2\Pi_{1/2}$ transition at 860 nm, with a lifetime of 57.1 ns [74], is:

$$I_s = \frac{\pi h c \Gamma}{3\lambda^3} = 5.7\ \mathrm{W/m^2} = 5.7\ \mu\mathrm{W/mm^2}. \tag{3.2}$$

If we include hyperfine, rotational, and vibrational splittings, the discussion becomes more complicated; see Section 4.8.2. In our experiments, we use a laser beam with a diameter of $\sim$1 mm ($1/e^2$) and use laser powers below 1 µW. Since this intensity is much weaker than that of the background light in the lab, the photodiodes are placed inside the black box, shown (with the cover removed) in Figure 3.3(b). The laser beams enter the box via coloured filter plates. With this box, almost no background light is detected on the photo diodes.

Figure 3.4 shows an example of an absorption spectrum. In blue, the measured

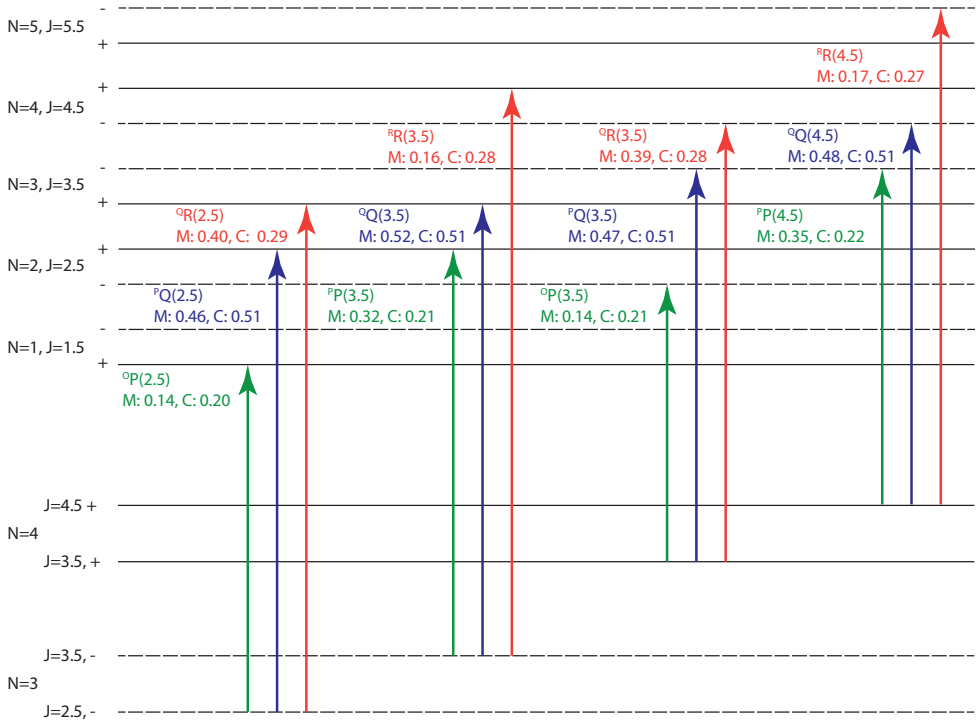

FIGURE 3.5: Rotational transitions from the $X^2\Sigma^+, N = 3$ and $N = 4$ rotational ground states to the $A^2\Pi_{1/2}$ excited states. The measured (M), in direct absorption, and calculated (C) intensity are indicated per transition and are normalized per rotational ground state. The labeling ${}^{\Delta N}\Delta J$ indicates the change in the quantum number N (the total angular momentum excluding electron and nuclear spin) and J (the total angular momentum excluding nuclear spin), respectively. O, P, Q and R indicate a change of -2,-1,0 and 1, respectively. Note that in the $A^2\Pi_{1/2}$ manifold, N is not a good quantum number [76]

${}^{Q}Q$-branch and ${}^{Q}R$-branch are depicted, which are nested into each other. In black, a simulated spectrum is shown, including the contribution of the five most dominant isotopes in different colours, taking into account their natural abundances. The simulation is performed by PGOPHER [75], using a rotational temperature of 12 K. The molecular constants for ^{138}BaF, ^{137}BaF, and ^{135}BaF are taken from Ref. [34]. For ^{136}BaF and ^{134}BaF, the molecular constants were not available with sufficient accuracy. Therefore, the molecular constants of ^{138}BaF were taken with only the origin shifted by an amount derived from a separate high-resolution measurement of the ${}^{R}Q_1(0.5)$ transition. The intensity of the simulated spectrum is scaled by setting the total intensity of the measured and simulated Q-branch to be equal.

When comparing the measurement and the simulation in Figure 3.4, it is obvious that they fit very well, but two differences are observed. Firstly, transitions from both lower and higher rotational states are more intense than expected from the simulation,

suggesting that the distribution is not well described by a single temperature. This will be discussed in more detail in Chapter 4. Secondly, on close inspection, we noticed that the ratio of the ${}^{Q}R$-branch to the ${}^{Q}Q$-branch is larger than expected from the simulation. For example, the ${}^{Q}R_{12}(2.5)$ and ${}^{Q}R_{12}(3.5)$ transitions are more intense than expected from the simulation, while the ${}^{Q}Q_{1}(3.5)$ and ${}^{Q}Q_{1}(4.5)$ transitions fit well.

To investigate this discrepancy more systematically, we have measured all 12 allowed rotational transitions that originate from the $X^2\Sigma^+, N = 3$ and $N = 4$ rotational ground states to the $A^2\Pi_{1/2}$ excited states, see Figure 3.5. From each J rotational state, a P, Q, and R transition is allowed, depicted in green, blue, and red, respectively. The relative measured (M) and calculated (C) intensity, normalised per rotational ground state is indicated. By normalising per rotational ground state, the relative intensity reflects the transition strength and does not depend on the rotational temperature. It was verified that the measured intensity does not depend on the laser polarisation. The calculation was performed by PGOPHER with the molecular constants found in Ref. [34].

The measurements presented in Figure 3.5 confirm the statement made earlier; while the measured relative intensities of the Q transitions are as expected from the simulation, the ${}^{O}P$ and ${}^{R}R$ transitions are consistently weaker than expected, and the ${}^{P}P$ and ${}^{Q}R$ transitions are consistently stronger than expected. Unfortunately, we have not (yet) found an explanation for the observed discrepancy.

3.4 Setup for laser-induced fluorescence detection

Laser-induced fluorescence detection is used to measure the forward velocity of the molecular beam and perform high-precision spectroscopy. To measure the forward velocity, we excite the molecular beam with a counterpropagating laser beam and determine the required detuning of the laser frequency to compensate for the Doppler shift; more details of these measurements will be presented in Chapter 5. For spectroscopy, detecting far from the source is beneficial as only transversely cold molecules are detected, which reduces the Doppler broadening.

Figure 3.6(a) shows a number of possible alignments, (b) shows a side view with details concerning the detection of fluorescence light by the photo-multiplier tube (PMT) and (c) an illustrating picture. As depicted in Figure 3.6(a), the molecules can be excited from either side by a laser beam (i) and (ii) or by a laser beam counterpropagating with respect to the molecular beam (iii). Both lasers can be connected via optical fibers to all optical paths, and the optimal configuration depends on the goal of measurement. Each optical path contains a polarising beam splitter to secure a linear polarisation after the optical fiber, followed by a half-waveplate to rotate the polarisation in a desired

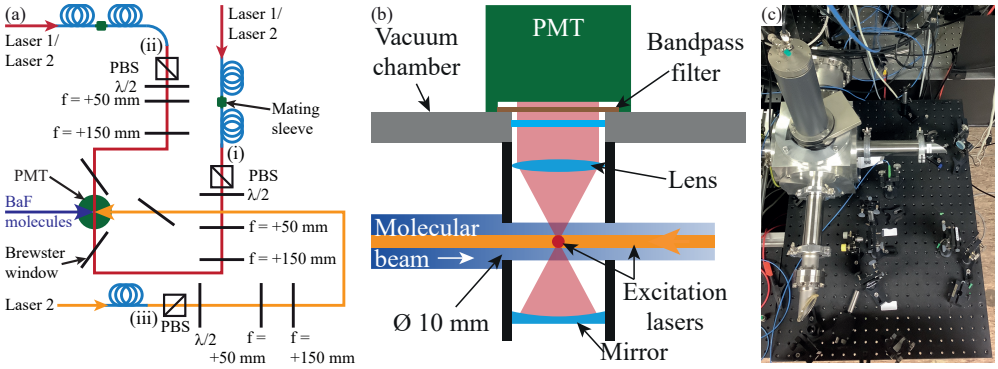

FIGURE 3.6: Laser-induced fluorescence setup. (a) A detailed overview of the optical setup, with three (i-iii) possible optical paths to connect one of the lasers to. (b) Schematic side view of the fluorescence light collection on the photo-multiplier tube (PMT). (c) A photographic image of the setup.

direction. For most measurements, the laser beams have a diameter that is slightly below 1 mm (FWHM), but for some measurements the beams were expanded to a diameter of 2.2 mm using a telescope. The beams enter the vacuum chamber through a window, placed at the Brewster angle. Fluorescence photons are detected by a PMT (Thorn EMI 9558 QB), placed above the setup.

Figure 3.6(b) shows the optical setup used to collect the fluorescence light on the PMT. Molecules are excited by one or two laser beams and emit photons in a random direction. A concave mirror is mounted below and a positive lens is mounted above the interaction zone to increase the solid angle of the detector. The collection efficiency is estimated to be 0.06, and the quantum efficiency of the PMT at 860, 815 and 414 nm, is $<$0.1, 1 and 22 %, respectively. A bandpass filter (Thorlabs FBH850-40, FBH800-40 or FBH400-40) is placed before the PMT, to filter out background light from the lab, and in the case of non-resonant detection, the excitation laser light. The holder for the collection mirror and lens has a 10 mm diameter aperture that limits the interaction zone; in practice, however, the interaction zone is determined by the size of the laser beams and the active area of the PMT. The residual Doppler shift for BaF at a forward velocity of 200 m/s is estimated to be about 2 MHz, comparable to the 2.79 MHz natural linewidth of the $X \rightarrow A^2\Pi_{1/2}$ transitions.

For measuring the longitudinal velocity of the molecular beam, Laser 1 and 2 are connected to paths (i) and (iii), respectively. As the frequency of the recorded fluorescence light is almost the sum of the excitation frequencies, a bandpass filter near 400 nm is used to filter out scattering photons originating from the laser light. This allows the beam size to be increased, which results in more signal, as the overlap of paths (i) and (iii) below the PMT scales with the diameter of the laser to the third power. For velocity measurement, both laser beam sizes are increased by using the

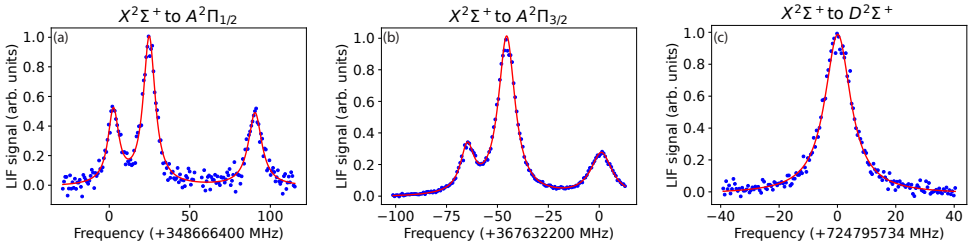

FIGURE 3.7: Three spectra showing splittings in rotational lines due to the hyperfine structure in the lowest excited electronic states of barium-fluoride. (a) and (b) show transitions from the $X^2\Sigma^+, N = 0, J = 1/2$ ground states to the lowest rotational states in the two spin-orbit components $A^2\Pi_{1/2}, J = 1/2$ and $A^2\Pi_{3/2}, J = 3/2$, respectively. (c) shows a resonant two-photon transition from the $X^2\Sigma^+, N = 0, J = 1/2, F = 1 \rightarrow D^2\Sigma^+, N = 0, J = 1/2, F = 1$ via the intermediate resonance $A^2\Pi_{1/2}, J = 1/2, F = 0$. The red solid lines show Lorentzian fits to the spectra.

telescope. More details can be found in Chapter 5.

When Doppler-free spectroscopy is performed, the laser beam(s) is aligned perpendicularly to the molecular beam. In order to eliminate residual Doppler shifts due to the alignment being non-perfect, two fibers are employed, one on each side of the fluorescence detection zone. The laser beam that is coupled out of one of the fibers, is coupled into the other fiber. During measurements, only one of the two fibers is used (either path (i) or (ii)), and these fibers are being switched between subsequent measurements. Consequently, a positive residual Doppler shift for the laser coupled out of one of the fibers, will result in an opposite Doppler shift for light traveling in the opposite direction, coupled out from the other fiber. The average value of the two measurements corresponds to the Doppler-free value.

Figure 3.7 shows three examples of spectra measured using the LIF setup with the excitation laser aligned perpendicular to the molecular beam. The high-resolution spectra reveal the hyperfine structure within rotational transitions.

3.5 Data acquisition and trigger

Digitalisation of analogue electronic signals from the photodiodes and PMT is performed by two digital oscilloscopes (Picoscope 5244D and 5444D), which are read out by the lab PC using a home-built Python-based interface. A shot-to-shot laser frequency control is included into the control software, where frequency feedback for the lasers is provided via the DC-voltage output of the Picoscope, which is connected to the 'external control' of the laser control box.

The electronic signal resulting from the detection of a photon, has a characteristic RC decay time that depends on the capacitance C, determined by the PMT, and the

input impedance R, of the oscilloscope. The latter can be modified by using a variable resistance (Thorlabs VT2). For our velocity measurements, the ideal RC-time is a compromise. A too long RC-time leads to a reduced time resolution of the observed temporal distribution of the observed molecular pulse, while a too short RC-time requires the picoscope to be set at a very high time resolution, which increases the time needed for data processing, making it necessary to reduce the repetition rate of the experiment. As a compromise, we chose an impedance of 50 kΩ, corresponding to a half-life of 8.925(18) µs. Note that the RC-time at 50 Ω impedance is 18 ns. For measurements in which the temporal information of the molecular pulse is irrelevant, i.e. for most spectroscopic experiments, the impedance of the Picoscope itself is used, which is about 0.9 MΩ.

Alternatively, photon counting could be used to measure the LIF signal. In short, using a 50 Ω resistance results in a short electronic peak that can be counted on a counter. An advantage of this technique is that any electronic background signal will not be counted and nearly background-free detection is possible. However, first quick tests showed no improved signal-to-noise ratio and it was not further investigated.

As the ablation laser is pulsed, the molecular signal is pulsed as well. The trigger for the ablation laser and oscilloscopes is provided by a delay generator (Stanford Research Systems, Inc. DG535). Because residual ground loops give rise to a background signal on the PMT, the delay generator is locked to the AC 50 Hz line frequency, such that the background signal is stable from shot to shot and is subtracted via a background measurement.

3.6 Determination of the laser frequency

The frequency of the two Ti:Sapphire ring lasers is stabilised using reference cavities. On timescales of 20 µs, a linewidth is below 50 kHz [77], but on the time scale relevant for the experiment the linewidth is broadened to about 0.8 MHz as a result of the frequency modulation employed to lock the laser to the reference cavity [78]. On longer time scales the frequency of the laser drifts due to temperature variation in the lab that changes the length of the reference cavity.

The frequency of the lasers is read out by two wavemeters (Lambdameter LM-007). The wavemeters were used to tune the lasers close to the transition frequency, however, the absolute frequency is shifted by $\sim$1.2 GHz and typically drifts by as much as 200 MHz during the day due to temperature variations in the laboratory. This drift is larger than the (FWHM) $\sim$120 and $\sim$5 MHz Doppler broadened transition widths measured with absorption or fluorescence detection, respectively. Thus, their accuracy is insufficient to warrent stable and reproducible measurements needed to characterise

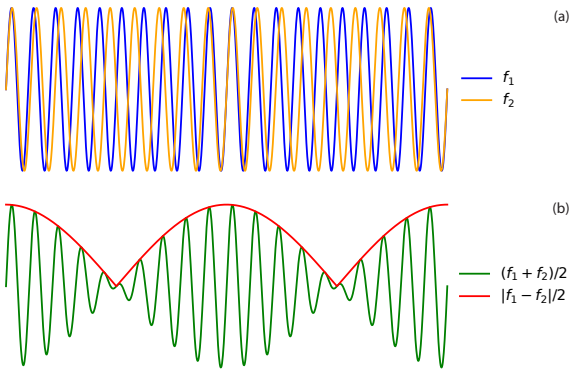

FIGURE 3.8: Illustration of the mixing of two frequencies. (a) Two frequencies f_1 and f_2 differ only marginally. (b) The beat signal of the combined frequencies. The 'beating' or envelope frequency, shown in red, corresponds to the difference of the two mixed frequencies and can be arbitrarily small.

and optimise our molecular beam source. This situation motivated us to set up a proper frequency readout and control system using a frequency comb.

3.7 Beat note with frequency comb for frequency reference and long-term stability

Optical frequencies are on the order of 10^{14} Hz, much faster than can be measured electronically. However, an interference beat note is generated if two lasers with different frequencies, $f_1 \neq f_2$, overlap on a photo detector, as illustrated in Figure 3.8. The fields combine to a product of the mean of, and the difference between the two initial frequencies:

$$\cos(2\pi f_1 t) + \cos(2\pi f_2 t) = \cos\left(2\pi \frac{f_1 + f_2}{2} t\right) \cos\left(2\pi \frac{f_1 - f_2}{2} t\right). \tag{3.3}$$

The combined signal is illustrated in Figure 3.8(b). Although the mean frequency in green is too high to detect, the amplitude beats with a frequency $f_b = f_1 - f_2$, shown as the red line. The beat frequency can be arbitrarily small by tuning the laser frequencies close to each other. When the frequency difference is on the order of MHz to GHz, the beat frequency can be measured with a fast photo-diode.

We use this method to determine the frequencies of the lasers. However, while f_b is being measured, to know f_1, we still need to know f_2, which is an optical frequency and thus too high to measure directly. We solve this problem by using a frequency comb as a reference laser.

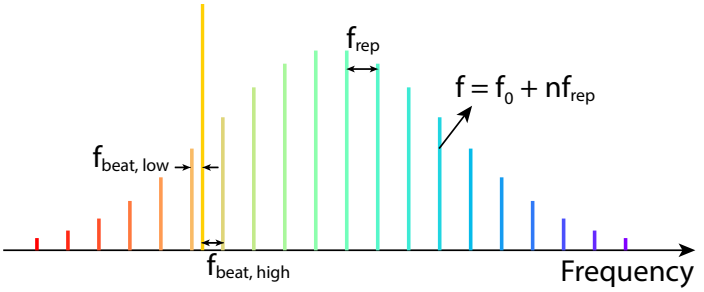

FIGURE 3.9: A picture illustrating the frequency comb spectrum. The comb modes are separated by a frequency f_{rep} and the absolute frequency f_n of each mode n follows from an integer number of f_{rep} plus an offset frequency f_0. If a laser with a certain frequency is mixed with the frequency comb, a beat frequency between the modes can be measured, with the lowest beat frequencies resulting from the frequency difference with the nearest modes.

In short, a frequency comb is a mode-locked laser with a fixed phase difference between subsequent pulses. Figure 3.9 shows the spectrum in the frequency domain, which consists of a comb of narrow frequency peaks with a well-defined frequency separation (repetition rate f_{rep}) and a well-defined offset from zero (f_0) [79, 80]. We use a Menlo Systems FC1500-250-WG frequency comb that is stabilised to a caesium clock (Microsemi CSIII Model 4301B). It has a repetition rate of about 250 MHz and a frequency offset of 20 MHz. The frequency range is in the infrared (IR) (∼1400-1800 nm), but a fraction of the initial laser light is frequency doubled to near-infrared (NIR) 700-900 nm light. The frequency doubled frequency comb has an offset equal to $2f_0 = 40$ MHz, while the repetition rate remains the same.

Due to the many modes of the comb, there is always a beat note present within $1/2 \times f_{rep} \approx 125$ MHz of the laser frequency. If the comb mode n is also known, the absolute frequency of the laser can be determined using the relation

$$f_{laser} = 2f_0 + nf_{rep} \pm f_b, \tag{3.4}$$

where the $\pm$ is written as the beat note is the same if the laser frequency is lower or higher than the specific comb mode frequency. Even without knowing the exact comb mode, as long as f_{rep} and f_0 are not changed, the beat note can be used as a frequency reference for stabilising and measuring a relative frequency shift.

To read and lock the laser frequencies, the frequencies of the beat notes are measured with a spectrum analyser (Siglent SSA3021X), which is read out by the main lab computer. The measured beat note frequency is used to derive an error signal that is converted to a voltage by our digital oscilloscopes (Picoscope 5244D and 5444D) and fed to the external voltage control of the lasers. In this way, the frequencies of the lasers are locked to the frequency combs and slow drifts are eliminated. The resulting

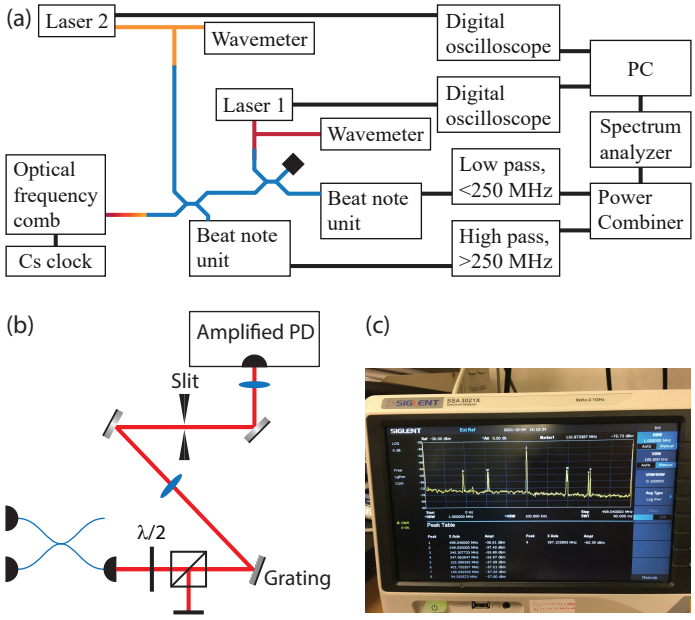

FIGURE 3.10: Frequency determination. (a) Schematic overview of the optical path and used electronics. Laser 1 and 2 are mixed with the optical frequency comb in two fiber optic couplers in series. The beat notes are measured by beat note units, frequency filtered and as a combined signal analysed on spectrum analyser and eventually to the data aquisition PC. For locking, the measured beat frequencies are compared with the set values and the laser frequencies are corrected using the DC voltage generator of the digital scopes connected to the external control of the laser box. (b) Free-space optical setup for frequency filtering before measuring the beat note with a fast amplified photodiode. (c) Picture of the spectrum analyzer, showing the 6 peaks as described in the text.

stability is on the order of a MHz, which is sufficient given that the natural linewidth of BaF in the $A^2\Pi_{1/2}$ state is 2.79 MHz. [74]. Moreover, this method allows us to scan over multiple GHz. An analogue (phase) lock to the frequency comb would result in higher stability, but scanning over a frequency range longer than f_{rep} would not be possible.

A detailed scheme for frequency readout and control is shown in Figure 3.10(a). To start, light from the doubled frequency comb is coupled into a 100 m optical fiber and sent to our laboratory. This light is mixed with a few microwatts of light from the two lasers using two 2x2 polarisation-maintaining fiber optic couplers (Thorlabs PN780R3A2) placed in series, with a mixing fraction that is wavelength dependent but is approximately 70-30 %. For the beat note of Laser 2, 70 % of Laser 2 is mixed with 30 % comb light, while the remaining 70 % comb light is mixed again with Laser 1 for the beat note of this laser. In the latter case, the mixed light also consists of some light from Laser 2, but typically the frequencies of Laser 1 and 2 are very different; thus, the

beat note of Laser 1 with the comb is not affected by Laser 2.

The beat frequency of the frequency comb with one of the lasers is measured with a fast amplified photodiode (MenloSystems APD210). For noise reduction, a small free-space optical setup is built in which the frequency comb spectrum is filtered using a grating (Thorlabs GR13-1208) and a slit, see Figure 3.10(b). To be able to readout both beat notes on a single spectrum analyser, low-pass filters (Mini-Circuits BLP-250+) are used to select frequencies below 250 MHz for the beatnote between the comb and Laser 1, while high-pass filters (Mini-Circuits BHP-300+) are used to select frequencies above 250 MHz for the beatnote between the comb and Laser 2. The filtered signals are mixed (Mini-Circuits ZFSC-2-4+) and sent to the spectrum analyser.

With the spectrum analyser set to a range of twice the repetition rate of the comb, typically 6 strong peaks are visible, see Figure 3.10(c). The two strongest peaks are the beat notes of the comb modes with each other, thus at the frequencies $f = if_{rep}$, with $i = 1, 2$. Between $f = 0$ MHz and $f = f_{rep}$, beat notes between Laser 1 and the comb mode just below (mode $n_{\text{Laser 1}}$), and just above (mode $n_{\text{Laser 1}} + 1$) are observed at frequencies given by:

$$f_{beat,low} = f_{laser} - [2f_0 + n_{\text{Laser 1}} f_{rep}], \tag{3.5}$$

and

$$f_{beat,high} = [2f_0 + (n_{\text{Laser 1}} + 1)f_{rep}] - f_{laser}. \tag{3.6}$$

Similarly, in the range between f_{rep} and $2 \times f_{rep}$, two beat notes are observed for Laser 2 with mode $n_{\text{Laser 2}} - 1$ and mode $n_{\text{Laser 2}} + 2$. These beat notes typically have a strength of 20-30 dBm above the noise level, which is more than sufficient to distinguish them from the noise.

The frequency and strength of these six peaks, possibly together with random noise peaks, are measured by the spectrum analyser and read out by the computer. Although in principle the beat frequency can be determined from either $f_{beat,low}$ or $f_{beat,high}$, both are used in the software as a criterion that $f_{beat,low} + f_{beat,high} = f_{rep}$ is a very effective tool to distinguish a genuine beat note from noise. There are a number of ranges where the frequency of the beat note cannot be resolved: close to 0 MHz, where a strong DC component is present, close to $i \times f_{rep}$ MHz with $i = 1, 2$, where the comb beats with its own comb modes and halfway, and for Laser 1 at $1/2 \times f_{rep}$ and for Laser 2 at $3/2 \times f_{rep}$, where the beat notes n and $n + 1$ overlap. If required, the frequencies in these ranges can be obtained by interpolation, as the frequency depends linearly on the control voltage.

Frequency locking is achieved by comparing the measured beat frequency with the desired frequency and changing the voltage generator set point of the digital oscilloscopes if so required. The voltage generator is connected to the external control

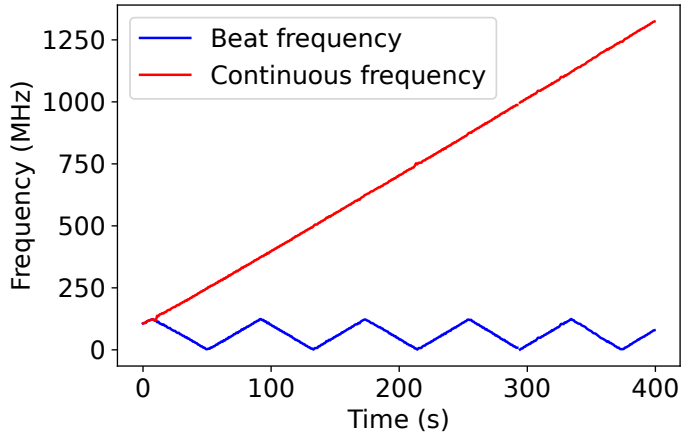

FIGURE 3.11: Measured beat note frequency while the laser is being scanned (blue line) and the corrected continuous laser frequency obtained in post-processing (red line).

of the ringlaser and by that the frequency is corrected. This results in a laser frequency stability of 2.6 and 1.6 MHz (FWHM) for Laser 1 and Laser 2 respectively, which is sufficient for detecting BaF molecules, as the natural linewidths for the electronic states $A^2\Pi_{1/2}$ and $A^2\Pi_{3/2}$ are 2.8 and 3.3 MHz [74], respectively.

When the lasers are scanned, the beat note is always below $1/2 \times f_{rep}$, and hence follows the triangular wave shown in Figure 3.11. As we know the scan direction, the beat frequency is automatically converted into a continuous frequency in post-processing.

3.8 Determination of the mode number of the nearest mode of the frequency comb for absolute frequency determination

If the resonance frequency of a transition is known a priori with an accuracy below f_{rep} or if a wavelength meter is used that has an absolute accuracy that is smaller than f_{rep}, the mode number of the nearest mode of the comb is known and the absolute transition frequency can be calculated using Equation (3.4), as f_0 and f_{rep} are known settings of the frequency comb. If this is not the case, the mode number of the nearest mode can be determined by recording the beat frequencies using different repetition rates with a mutual frequency difference that is greater than the precision of the measurements, as described in [81, 82].

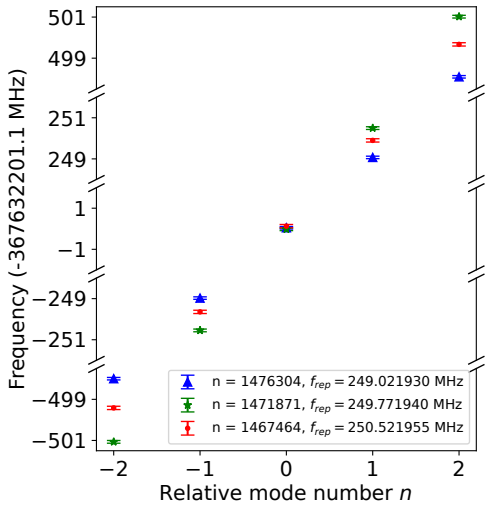

FIGURE 3.12: Absolute transition frequency calculated from measurements with three different repetition rate frequencies. The transition frequency is only consistent when the mode number of the nearest mode at a certain repetition frequency is correctly assigned. When an incorrect mode number is used, the transition is measured at a different beat frequency than expected when the repetition frequency is changed.

Figure 3.12 illustrates the method, where the $X^2\Sigma^+, N = 0, J = 1/2, F = 0 \rightarrow A^2\Pi_{3/2}, J = 3/2, F = 1$ transition is measured using repetition rate frequencies of 249.0, 249.8 and 250.5 MHz. Filling in the measured beat frequency into Equation (3.4) leads to a consistent transition frequency if the mode numbers n =1476304, 1471871 and 1467464 are used, respectively. If a lower or higher mode number is used, the calculated transition frequencies depend on the used repetition rate frequency, which is clearly wrong, as the uncertainty of the measuremt is smaller than the frequency differences between the used repetition rates.

3.9 Conclusions

This chapter introduced methods and described the setup used to perform spectroscopy on molecular beams. We have two lasers that can be locked to a frequency comb and which can be used for absorption and laser-induced fluorescence detection. In the following chapters, we will use these to characterise the molecular beam produced by the source as described in Chapter 2.

The thermodynamics of a cryogenic molecular beam

4

4.1 Introduction

This chapter covers the thermodynamic properties of the molecular beam. I will start with a qualitative description of all relevant processes and properties of the beam, followed by measurements of these properties. Combining these measurements allows us to estimate the number of molecules in the beam, by which the chapter is concluded.

4.2 Description of the molecular beam

As described in Chapter 2, molecules are formed inside a buffer gas cell and some of these leave the cell together with the buffer gas through the aperture to form a beam. Because the density of the buffer gas is typically $>10^6$ times higher than the density of the molecules, the thermodynamic properties of the molecular beam are determined by the buffer gas.

In the so-called 'effusive' regime [83], where the density of the buffer gas is low, the mean free path is long, and virtually no collisions take place at the aperture or outside the source. The velocity distribution of the molecules in the beam is the same as that inside the cell and is described by the one-dimensional Maxwell-Boltzmann distribution: i.e., the most probable forward velocity is about 145 and 52 m/s for neon and BaF at 20 K, respectively, and has a large velocity spread. The transverse velocity follows a Gaussian distribution with a zero mean velocity and a width determined by the cell temperature. Directly outside the cell, the density distribution of the beam is a flat top with a diameter equal to that of the aperture. Further away from the cell, the density decreases because of the divergence of the beam and is more accurately described by a Gaussian distribution. While the neon flow is constant, the BaF beam is pulsed as molecules are only produced shortly after the ablation pulse. The temporal profile depends on the length of the cell and density of the buffer gas.

In our experiments, we operate the source in the so-called 'hydrodynamic' regime, where the buffer gas density is higher than in the effusive regime, leading to an increased extraction efficiency [50]. In this regime, many collisions take place as the molecules pass through the aperture. This affects the molecular beam in the following way: The mean velocity of the molecules increases as the expansion becomes supersonic.

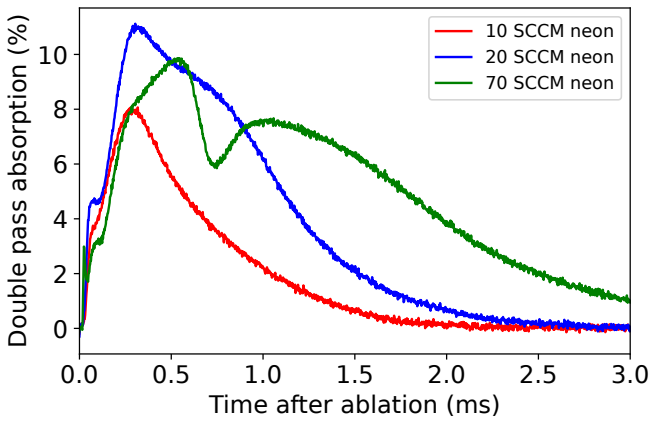

FIGURE 4.1: Absorption signal as a function of time after the ablation laser pulse for a neon buffer gas flow rate of 10, 20 and 70 SCCM.

In the longitudinal direction, the mean velocity of the molecules is determined by the velocity of the neon buffer gas, which is already larger than that of the BaF molecules because of its lower mass, but it also increases because of the pressure gradient. In the transverse direction, collisions also lead to an increase in the velocity, as the density at the molecular beam axis is larger than away from the centre line. The divergence, given by the ratio between the width of the transverse velocity distribution and the mean longitudinal velocity, may increase or decrease, depending on the exact buffer gas density [84].

In this chapter, I will first present measurements of the temporal profile, the transverse volume and divergence, and the rotational and vibrational temperature of the molecular beam. Measurements of longitudinal velocity are presented and discussed in Chapter 5 and Chapter 6. In the last part of this chapter, I will calculate the number of molecules in the molecular pulse.

4.3 Absorption signal as a function of time

Figure 4.1, shows the percentage of light absorbed by the molecular pulse as a function of time after the ablation pulse at three different flow rates of the neon buffer gas. The laser frequency is resonant with the $X^2\Sigma^+, N = 0, J = 1/2, F = 1 \rightarrow A^2\Pi_{1/2}, J = 1/2, F = 0$ $(Q(0.5))$ transition at 348 666 402.6(3) MHz [85]. After the ablation pulse, barium atoms will react with hexafluoride molecules to form bariumfluoride. The molecules will diffuse through the cell and may reach the exit by chance. At the same time, there is a net flow of buffer gas through the cell that takes the bariumfluoride molecules along. The interplay between these two processes determines the temporal

profiles observed in Figure 4.1. Before going into that, I will first discuss the dependence of these processes on the flow rate of the buffer gas.

4.3.1 Buffer gas density and flow velocity in the cell

We will first relate the density and net flow velocity in the cell to the flow of buffer gas into the cell. In an effusive regime, the particles do not collide with each other near the aperture, and they leave the cell by chance. The flow f_{out} of particles that leave the cell depends on the area of the aperture A_{a}, the mean velocity $\overline{v}$ of the atoms at the aperture and the density n_{b} of the gas:

$$f_{\mathrm{out}} = \frac{A_{\mathrm{a}}\overline{v}n_{\mathrm{b}}}{4}, \tag{4.1}$$

where $A_{\mathrm{a}} = \pi(d_{\mathrm{a}}/2)^2$ with diameter d_{a} and the factor 4 results from the integral over all velocities, selecting atoms that have a velocity towards the exit [83]. The mean velocity of the beam is given by the velocity of the thermal gas inside the cell:

$$\overline{v} = \sqrt{\frac{8k_{\mathrm{B}}T}{\pi m_{\mathrm{b}}}}, \tag{4.2}$$

with k_{B} the Boltzmann constant, T the temperature of the buffer gas inside the cell, and m_{b} the atomic mass of the buffer gas.

At the same time, the buffer gas flows into the cell from the back side at a rate f_{in} controlled by the mass flow controller. In steady state these two flow rates are equal:

$$f_{\mathrm{out}} = f_{\mathrm{in}}. \tag{4.3}$$

By combining Equation (4.1) and Equation (4.3) we find the density in the cell:

$$n_{\mathrm{b}} = \frac{4f_{\mathrm{in}}}{A_{\mathrm{a}}\overline{v}}. \tag{4.4}$$

For reference, for our cell, at a flow rate of 10 SCCM, we find a density of about 7.8×10^{15} neon atoms per cm^3.

Let us now calculate the net flow velocity of the buffer gas atoms through the cell. In steady state, the flow through the cell is equal to the flow in and out of the cell, thus we find:

$$f_{\mathrm{out}} = A_{\mathrm{c}}v_{\mathrm{flow}}n_{\mathrm{b}} = f_{\mathrm{in}} \tag{4.5}$$

which implies that the net *flow* velocity in the cell is given by:

$$v_{\mathrm{flow}} = \frac{f_{\mathrm{in}}}{n_{\mathrm{b}}A_{\mathrm{c}}} = \frac{A_{\mathrm{a}}}{A_{\mathrm{c}}}\frac{\overline{v}}{4}, \tag{4.6}$$

where $A_c = \pi(d_c/2)^2$ is the inner cell area with cell diameter d_c. At a flow rate of 10 SCCM, we find a net *flow* velocity of 7.3 m/s.

When we increase f_{in}, both the net flow velocity through the cell and the density will increase, more collisions will occur near the exit, and ultimately the flow will become hydrodynamic. One consequence of this is that the longitudinal velocity distribution of the beam will narrow, while the mean velocity increases by a maximum factor of 1.4, as discussed in Chapter 6. The exact density and flow velocities in the cell and the aperture are more difficult to determine. A larger fraction of the atoms will now leave the cell, that is, the factor 1/4 in Equation (4.1) that results from the integral over the velocities will become closer to unity. However, at the same time, the increase in the number of collisions prevents the atoms from leaving the cell at a velocity $\overline{v}$. These two effects are likely to cancel each other, resulting in an increase in density that is linear with f_{in}, while the net flow velocity in the cell remains almost constant. This argument is corroborated by our measurements of the longitudinal velocity presented in Chapter 6.

4.3.2 Pump time and diffusion time

The average time it takes to pump the molecules out of the cell with length L is:

$$\tau_p = \frac{L}{v_{flow}} \tag{4.7}$$

For our cell with an aperture and inner cell diameter of 4.5 and 10 mm, respectively, the pump time τ_p is estimated to be ~1.5 ms. From the previous discussion, τ_p is expected to be almost insensitive to the flow rate.

In contrast, the diffusion rate depends linearly on the buffer gas density in the cell and hence on the flow rate. For a cylindrical cell of length L and radius r, the time constant is given by [86]:

$$\tau_d = \frac{n_b \sigma_{b-s}}{\overline{v} G}, \tag{4.8}$$

with σ_{b-s} the collisional cross section between the buffer gas and the species of interest and G a geometric factor of the cell:

$$G \approx \frac{3\pi}{32}\left(\frac{2.405^2}{r^2} + \frac{\pi^2}{L^2}\right) = 9.2 \times 10^{-2}\ \mathrm{mm}^{-2}, \tag{4.9}$$

where we have filled in $L = 11$ mm and $r = 5$ mm for our cell.

The number of molecules inside the cell decreases exponentially in time as they are lost as soon as they diffuse to the walls of the cell, on which they will freeze, or when they escape through the aperture to form the molecular beam. The exponential decrease is reflected in the temporal distribution of the molecular beam measured at

low flow rates. When the flow rate increases, the ratio between the diffusion time and the pump time $\tau_{\mathrm{d}}/\tau_{\mathrm{p}}$ also increases, resulting in improved extraction efficiency as more molecules are pumped out of the cell before hitting the walls [50]. If entrainment is dominant, i.e. ignoring the diffusion loss, the temporal profile will approximately follow a Gaussian distribution, with a mean arrival time at the aperture given by the pump time and the spread determined by the diffusion rate. In an intermediate regime, the combination of an exponential decay and a Gaussian distribution leads to a lob-sided Gaussian distribution. Indeed, as may be observed in Figure 4.1, at higher flow rates, the number of molecules in the beam increases markedly, particularly at later times close to the pumping time estimated earlier.

In practice, the temporal profile typically shows some substructure, especially for higher flow rates. The exact nature is hard to determine, and we attribute these to overexpansion of the buffer gas; when the gas inside the cell is heated by the ablation pulse (see Chapter 6), the pressure increases above the equilibrium value, resulting in more atoms leaving the cell through the exit and less atoms entering the cell from the tubes. Upon a subsequent decrease in the temperature of the gas through conduction to the cell walls, the pressure decreases and drops temporarily below the equilibrium value. Because these fluctuations in f_{out} and buffer gas densities give rise to more or less extraction and diffusion loss, some substructure can arise in the temporal profile of the molecular pulse.

4.4 Neon-BaF collisional cross section

Using Equation (4.8), we can derive a value for the collisional cross section between neon buffer gas and BaF molecules. In an effusive regime, where the buffer gas density is low, $\tau_{\mathrm{d}} < \tau_{\mathrm{p}}$, the loss of molecules is dominated by diffusion and the decay of the signal in the tail of the time-of-flight profile is described by an exponential with the time constant τ_{d}. In Figure 4.2(a), we again show the absorption profile measured on the $X^2\Sigma^+, N = 0, J = 1/2 \rightarrow A^2\Pi_{1/2}, J = 1/2$ transition at a flow rate of 10 SCCM, but now plotted on a logarithmic scale. The orange and red lines correspond to a fit of the time constant over two different periods in the pulse. The values for the time constants for the two fits are 0.53 and 0.32 ms, respectively. The loss rate of molecules is thus larger towards the trailing end of the pulse. A similar observation was made by Skoff *et al.* [87], who compared the absorption signal of atomic lithium with that of YbF molecules within the cell and noticed that shortly after the ablation pulse the molecular signal decayed more slowly than the atomic signal. They attributed this effect on rotational cooling that replenishes the number of molecules in the lowest rotational state. The best value of the cross section therefore follows from the trailing

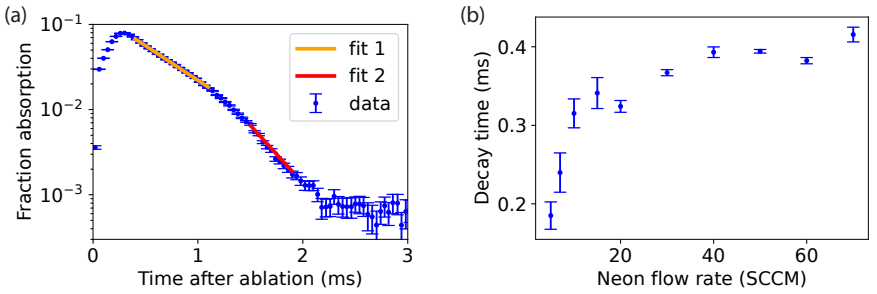

FIGURE 4.2: Exponential decay of the absorption profile reflecting the number of molecules inside the cell. In (a), the measured absorption signal as a function of time is plotted on a logarithmic scale, using a buffer gas flow rate of 10 SCCM. Two fits are performed, showing that the decay rate increases towards the end of the molecular pulse. (b) The decay time plotted as a function of the flow rate of the buffer gas. At low flow rates the loss of molecules is dominated by diffusion which increases linearly with the flow rate. At higher flow rates, the loss is dominated by pumping which does not depend on the flow rate.

end of the pulse. Filling in the numbers, using the density of Equation (4.4), gives:

$$\sigma_{\mathrm{Ne-BaF}} = \frac{\tau_{\mathrm{d}}\bar{v}G}{n_{\mathrm{b}}} = \frac{\tau_{\mathrm{d}}A\bar{v}^2G}{4f_{\mathrm{in}}} \approx 5 \times 10^{-15}\ \mathrm{cm}^2, \tag{4.10}$$

which is comparable to the value for $\sigma_{\mathrm{He-ThO}}$ reported by Hutzler *et al.* [37] and slightly smaller than $\sigma_{\mathrm{He-BaF}}$, $\sigma_{\mathrm{He-YbF}}$ and $\sigma_{\mathrm{He-SrOH}}$, presented by Bu *et al.* [60], Skoff *et al.* [87] and Kozyryev *et al.* [86], respectively.

Figure 4.2(b) shows the decay time at the end of the pulse as a function of the flow rate of the buffer gas. At low flow rates, the time constant increases linearly with the buffer gas density, as expected from Equation (4.8). This suggests that the loss at a flow rate of 10 SCCM is determined by diffusion. At higher flow rates, the loss is dominated by pumping, which does not depend on the flow rate, hence the decay time becomes constant. Note that the obtained value for the cross section can be considered to be a lower limit for the collisional cross section.

4.5 Transverse velocity

4.5.1 Transverse velocity as a function of buffer gas flow rate and distance from source exit.

In this section, I will discuss the transverse velocity distribution of the molecular beam, which was measured using absorption detection at different flow rates at two distances behind the cell exit. The intensity of the laser was set well below the saturation intensity

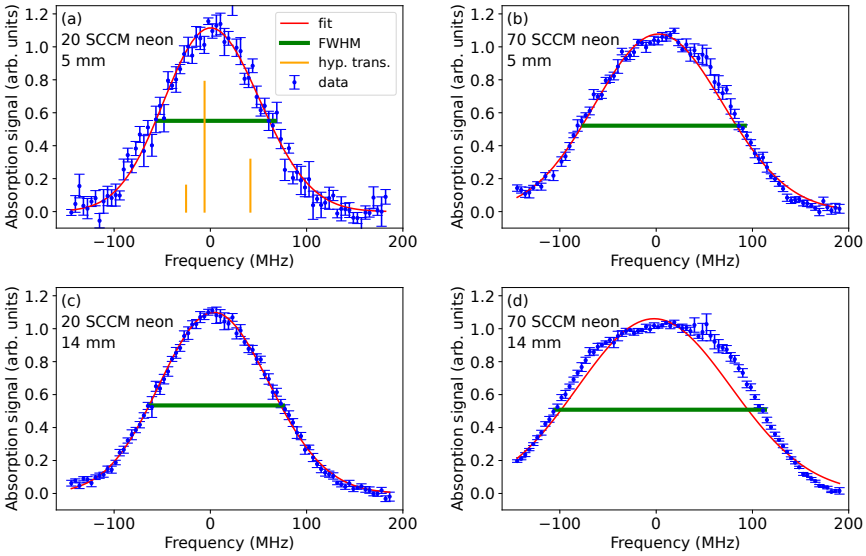

FIGURE 4.3: Absorption signal as a function of the excitation laser frequency. (a), (b) are measured $z = 5$ mm from the source exit and (c), (d) are measured $z = 14$ mm from the source exit, respectively, with (a), (c) using 20 and (b), (d) using 70 SCCM buffer gas flow rate. In blue, the measured absorption, averaged over the duration of the molecule pulse (1 ms), is depicted. The absorption features are fit using three Gaussians centered at the expected frequencies for the (hyperfine components of the) $X^2\Sigma^+, N = 0, J = 1/2 \rightarrow A^2\Pi_{3/2}, J = 3/2$ transition, illustrated in orange. In green, the FWHM is shown.

of the transition, such that the line shape is dominated by Doppler broadening and a measured frequency shift Δf relative to the zero velocity resonance frequency f can be converted into a velocity of the molecules by:

$$\Delta v_\perp = \frac{\Delta f}{f} c, \tag{4.11}$$

with c the speed of light.

In Figure 4.3(a)-(d) typical Doppler-broadened absorption spectra of a beam of molecules are presented. Panels (a) and (b) are measured 5 mm after the source exit, using a buffer gas flow rate of 20 and 70 SCCM, respectively, while (c) and (d) are measured 14 mm after the source exit with the same buffer gas flow rates. The spectra contains the three hyperfine transitions of the $X^2\Sigma^+, N = 0, J = 1/2 \rightarrow A^2\Pi_{3/2}, J = 3/2$ transition at 815 nm, illustrated in orange in Figure 4.3(a).

Two effects are visible. The transverse velocity increases (1) as a function of the distance from the source and (2) as a function of the flow rate of the buffer gas. Both effects are indicative of collisions that take place behind the exit of the cell. As the

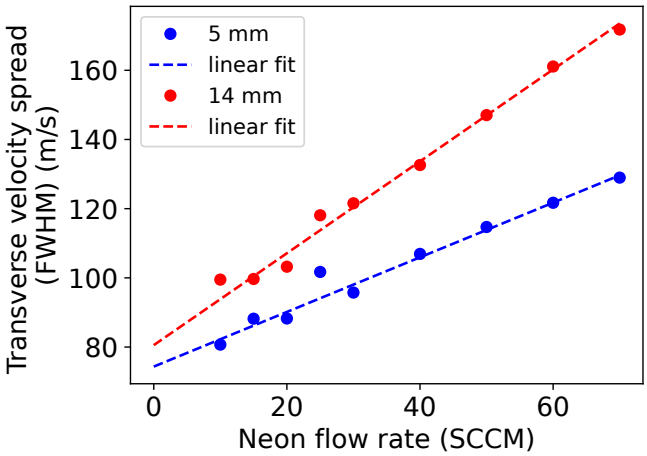

FIGURE 4.4: Transverse-velocity spread as a function of buffer gas flow rate measured 5 (blue dots) and 14 mm (red dots) behind the source exit. Collisions after the source exit leads to an increased transverse velocity spread, and a linear fit onto the data close by and far from the cell aperture is depicted by the blue and red dashed lines, respectively.

pressure at the centre line is higher than away from it, collisions convert potential energy into translational energy, leading to an increase in the transverse velocities in the same way that the longitudinal velocities are boosted during the expansion. At low flow rate and close to the cell, the measured velocity distribution reflects the Maxwell-Boltzman velocity distribution in the cell and is well described by a Gaussian with a FWHM equal to $\sqrt{\pi \ln(2)}\bar{v}_{\mathrm{BaF}} = 77$ m/s. At a higher flow rate and further from the aperture, the number of molecules with high transverse velocities is increased compared to those with low transverse velocity, and the measured distribution becomes more flat-top due to collisions with the expanding buffer gas.

The solid red lines also shown in Figure 4.3, result from Gaussian fits to the absorption profiles using the relative intensities and frequencies of the three hyperfine transitions predicted by the PGOPHER simulation of Appendix A. To account for the non-Gaussian shape, the following method is applied. First, the FWHM of the data is determined; see the green line. Subsequently, numerically, a standard deviation is determined for which the triple Gaussian functions have equal FWHM to the data. The standard deviation found in this way is taken as a measure for the transverse-velocity spread.

In Figure 4.4, the FWHM transverse velocity of the molecular beam is shown for multiple neon flow rates measured at 5 (blue dots) and 14 mm (red dots) after the exit of the source. As described by Hutzler *et al.* in Refs. [37] and [84], the transverse

velocity is expected to increase linearly with the Reynolds number Re:

$$\Delta v_{\perp} \approx \sqrt{\pi \ln(2)}\overline{v}_{\mathrm{BaF}} + \alpha Re. \tag{4.12}$$

The Reynolds number is a dimensionless parameter that corresponds to the number of collisions an atom will typically undergo while passing the aperture. It is a measure of the thermodynamic regime of the cell, i.e. for small and large Reynolds numbers, the cell is operated in the effusive and hydrodynamic regimes, respectively. The Reynolds number is approximately:

$$Re \approx \frac{2d_{\mathrm{a}}}{\lambda_{\mathrm{b-b}}} \approx \frac{8\sqrt{2}\sigma_{\mathrm{b-b}}d_{\mathrm{a}}f_{\mathrm{in}}}{A_{\mathrm{a}}\overline{v}}, \tag{4.13}$$

with $\lambda_{\mathrm{b-b}} = \sqrt{2}\sigma_{\mathrm{b-b}}n_{\mathrm{b}}$ the mean free path of the buffer gas atoms in the cell and $\sigma_{\mathrm{b-b}}$ the collisional cross section between the atoms. In Chapter 6 we have found $\sigma_{\mathrm{b-b}} \approx 1.9 \times 10^{-15}$ cm^2. For our configuration, we find that 1 SCCM corresponds to $Re = 1.9$.

The dashed blue and red lines show the result of a linear fit of the transverse velocity as a function of the buffer gas flow rate. Extrapolating the fit to zero flow leads to a transverse velocity spread close to the expected 77 m/s. The slope α of the blue and red fit corresponds to an increase of 0.42 and 0.71 m/s per Re, respectively. These values are similar to those found in Ref. [37]. As mentioned in [84], modelling the transverse velocity spread far from the aperture is more complicated due to the expansion of the beam, but typically the increase in velocity is about twice as large, which is found by the fit corresponding to the red dashed line.

4.5.2 Divergence as a function of buffer gas flow rate and distance from source exit.

Combining the mean transverse velocity $\overline{v}_{\perp}$ with the mean forward velocity $\overline{v}_{\parallel}$ gives a measure of the divergence of the molecular beam. The solid angle extended by the molecular beam is given by Ω [84],

$$\Omega = 2\pi\left(1 - \cos\left(\tan^{-1}\left(\frac{\overline{\mathrm{v}}_{\perp}/2}{\overline{\mathrm{v}}_{\parallel}}\right)\right)\right). \tag{4.14}$$

Figure 4.5 shows the solid angle as a function of the flow rate of the buffer gas, using the results of Figure 4.4 and the measurements of the forward velocity that will be presented in Chapter 6. Both the forward velocity and the transverse spread increase as a function of the flow rate, so the divergence could remain constant. However, for

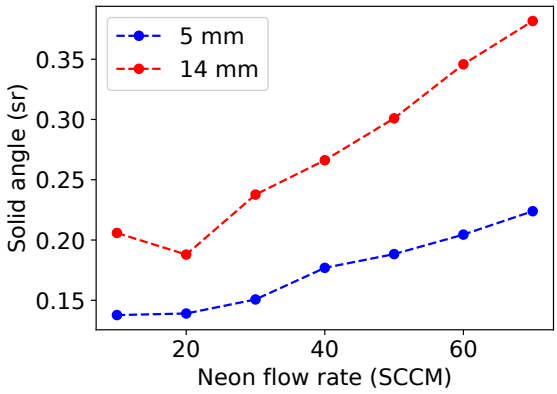

FIGURE 4.5: Divergence, given by the solid angle, of the molecular beam as a function of the buffer gas flow rate at two distances from the cell aperture as indicated in the legend.

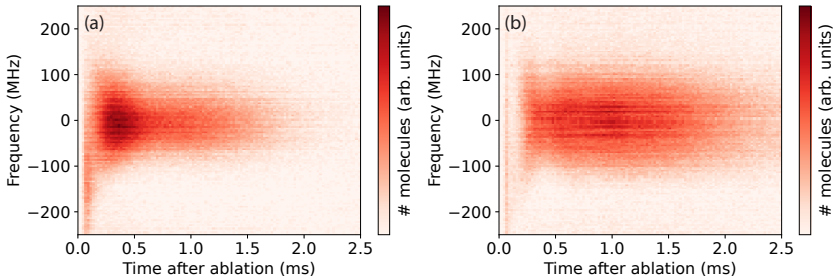

FIGURE 4.6: The absorption signal as a function of time after ablation and excitation frequency for (a) 20 and (b) 70 SCCM buffer gas flow rate.

the settings used in our source, the transverse velocity spread increases faster than the forward velocity, and the divergence is found to increase monotonously with flow rate.

4.5.3 Transverse velocity as a function of time in the molecular pulse

So far, we have analysed the transverse velocity of the complete molecular pulse by averaging the signal over the duration of the pulse. Here, we look into more detail to the temporal dynamics of the transverse velocity. Figure 4.6(a) and (b) show a heat map of the absorption signal measured 5 mm behind the cell exit as a function of the detuning from the $Q(0.5)$ transition and the time after ablation for a buffer gas flow rate of 20 and 70 SCCM, respectively. Using Equation (4.11), the frequency axis can be converted into a velocity. At 20 SCCM shown in (a), the molecular pulse is rather short, while the width of the absorption profile initially decreases and subsequently

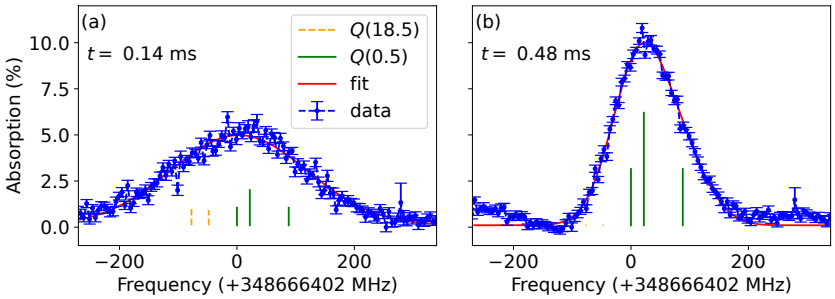

FIGURE 4.7: Absorption signals as function of the frequency close to the $Q(0.5)$ transition recorded 0.14 ms and 0.48 ms after the ablation pulse at a flow rate of 20 SCCM (blue data points). The red line results from a multi-Gaussian fit to the data using the frequencies and relative intensities of the three hyperfine transitions of the $Q(0.5)$ transition (green sticks) and the two strongest transitions of the $Q(18.5)$ transition (dashed orange sticks) as fixed parameters.

remains constant. At 70 SCCM shown in (b), the pulse is much longer and the width is significantly wider than that observed in (a). In both measurements, but most prominently in (a), shortly after firing the ablation laser, a feature may be observed at lower frequency. We attribute this feature to the $Q(18.5)$ transition, indicating that immediately after the ablation pulse a significant population was present in the $J = 18.5$ ground state.

In order to analyse these data more quantitatively, we assume that the transverse velocity is well described by a Maxwell-Boltzmann distribution, and hence fit Gaussian functions to the absorption spectrum, which are binned over short time intervals, and determine the Doppler broadening. Figure 4.7 shows two examples of such spectra recorded 0.14 ms and 0.48 ms after the ablation pulse at a flow rate of 20 SCCM. The blue points are the measured absorption data, and the red lines result from a multi-Gaussian fit using the frequencies and intensities of the (three hyperfine components of the) $Q(0,5)$ transition and the (strongest two hyperfine components of the) $Q(18,5)$ transition as fixed parameters and the amplitude and width as free parameters. Intensity and frequencies are calculated using the simulation program PGOPHER described in Appendix A. As observed, immediately after the ablation pulse, the $Q(18.5)$ transition contributes strongly to the measured signal, while at later times the contribution is virtually zero.

Figure 4.8 presents the transverse velocity spread (FWHM) as a function of time after the ablation pulse for a buffer gas flow rate of 10 to 70 SCCM as indicated in the legend. The absorption signal was binned over time intervals that varied from 40 µs shortly after the ablation pulse was fired, to 120 µs at the end of the pulse, to have optimal temporal resolution and signal-to-noise ratio. As observed, directly after the ablation laser is fired, the gas is hot and the transverse-velocity spread large. As the buffer gas

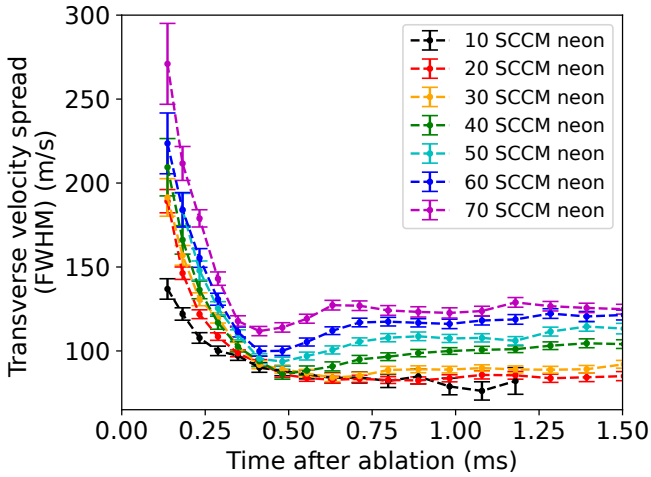

FIGURE 4.8: Transverse velocity spread as a function of time after ablation, for different neon flow rates as indicated in the legend. These measurements were performed with a slightly (10 mm) longer cell than most other measurement in this chapter.

is cooled by conduction to the cell walls, the velocity spread decreases, until about 0.7 ms, when it becomes constant. The transverse-velocity spread increases linearly with the flow rate of the buffer gas, as discussed previously. At about 0.4 ms after the ablation pulse, a dip is observed. As discussed in Section 4.3, we attribute this dip to overexpansion of the buffer gas. As the cooling rate depends on the cell length and the contamination of the cell wall (see Chapter 6), the exact timing of the dip may vary between measurements.

4.6 Transverse volume

In this section, we examine the transverse spatial distribution of the molecules. To measure the absorption signal as a function of position in the molecular beam, the horizontally aligned laser beam is moved in the vertical direction. The measured time-averaged absorption is shown with the blue dots in Figure 4.9. Note that the range of vertical positions is limited by the size of the openings in the heat shields. The signal drops with distance from the centre because of the divergence of the beam. The signal fits well with a Gaussian distribution with a FWHM beam size of 4.4 mm, shown as the solid red line. For reference, the expected measurement profile at the exit, that is filled homogeneously, is shown as the solid green line.

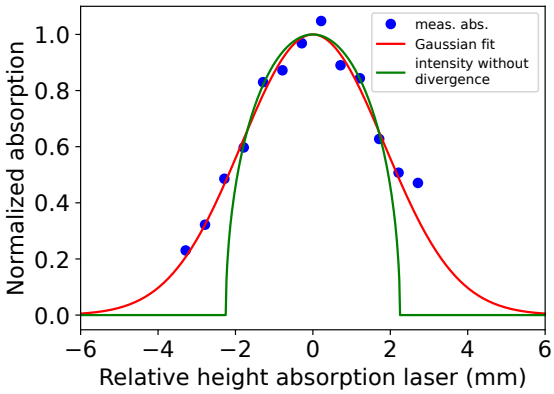

FIGURE 4.9: Spatial distribution of the molecular beam 5 mm after the cell exit, for a buffer gas flow rate of 20 SCCM, measured by moving the laser beam vertically through the molecular beam while recording the absorption.

4.7 Rotational and vibrational temperatures

4.7.1 Theory

At zero Kelvin, all BaF molecules would be in the lowest quantum state. However, at a finite temperature, the residual energy leads to some molecules populating higher energetic states. The probability of a certain hyperfine state F_i being populated drops exponentially with the energy E_i of that state:

$$p(F_i, E_i, T) = \frac{(2F_i + 1)e^{-\frac{E_i}{k_B T}}}{\sum_i (2F_i + 1)e^{-\frac{E_i}{k_B T}}}, \tag{4.15}$$

with T the rotational temperature of the molecules, k_B the Boltzmann constant and $2F_i + 1$ accounting for the multiplicity of the levels. When hyperfine structure is unresolved, F_i can be replaced by J_i.

In BaF, the first excited rotational levels have energies ranging from 0.43 cm^{-1} ($N = 1$) to 24 cm^{-1} ($N = 10$), the first excited vibrational state lies at 466 cm^{-1} and the first excited electronic state lies at 11630 cm^{-1}. In our source the temperatures are well below 20 K and we would expect only the lowest few rotational states of the vibrational ground state of the X-electronic ground state to be populated, i.e., 1 cm^{-1} corresponds to 1.4 K. Figure 4.10(a) shows a simulated population distribution per rotational number N for a rotational temperature of 2 and 6 K. For each N state, the contributions of all hyperfine states are summed. Typically, in experiments with cold molecules, a concentration of the population in a single low quantum state is

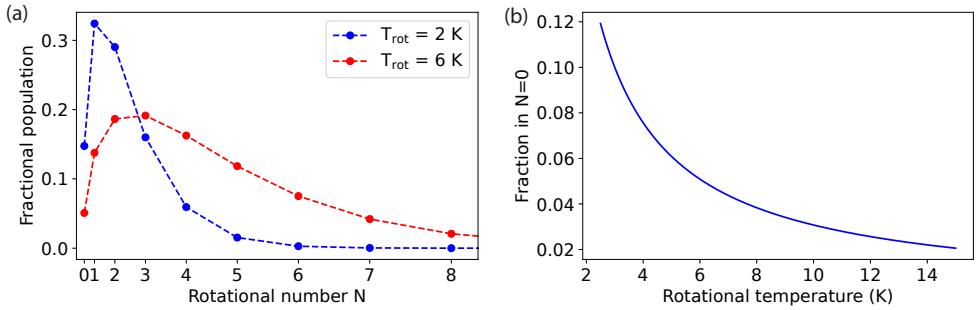

FIGURE 4.10: Calculated rotational population. (a) The population distribution spread out over different rotational states for a rotational temperature of 2 and 6 K. (b) The fraction of population in $N = 0$ state as a function of the rotational temperature.

desired. Figure 4.10(b) illustrates that lowering the rotational temperature leads to more molecules in the lowest rotational state $N = 0$.

We will see in the next sections that the vibrational and, to a lesser extent, the rotational degrees of freedom are not in thermal equilibrium with the translational degrees of freedom, and a considerable fraction of the molecules populates higher rotational and vibrational states.

4.7.2 Measurement of the rotational temperature

To determine the rotational and vibrational temperature, we measured the intensities of several rotational transitions. As discussed before, collisions take place after the first absorption position at $z = 5$ mm, and these influence the properties of the beam, particularly at a high flow rate of the buffer gas. As collisions are also expected to influence the rotational and vibrational distribution, we have performed our measurements as a function of the buffer gas flow rate both at 5 and 780 mm after the source exit using absorption and fluorescence detection, respectively. Furthermore, we have investigated whether increasing the length of the cell changes the rotational and vibrational temperature.

In principle, the rotational temperature can be obtained from any set that contains transitions from different rotational states. The natural choice would appear to measure the Q-branch of the $X^2\Sigma^+$-$A^2\Pi_{1/2}$ transition at 860 nm shown in Figure 3.4 which can be recorded in a single frequency scan with our Ti:sapph lasers. However, analysis of the absorption spectrum is complicated by many overlapping rotational lines from different isotopes of BaF. Therefore, we chose to measure the population in lowest $J = N + 0.5$ states using the ${}^SR$-branch of the $X^2\Sigma^+ \rightarrow A^2\Pi_{3/2}$ transition near 815 nm, because this branch is well isolated from other branches (except for the ${}^SR(1.5)$-transition).

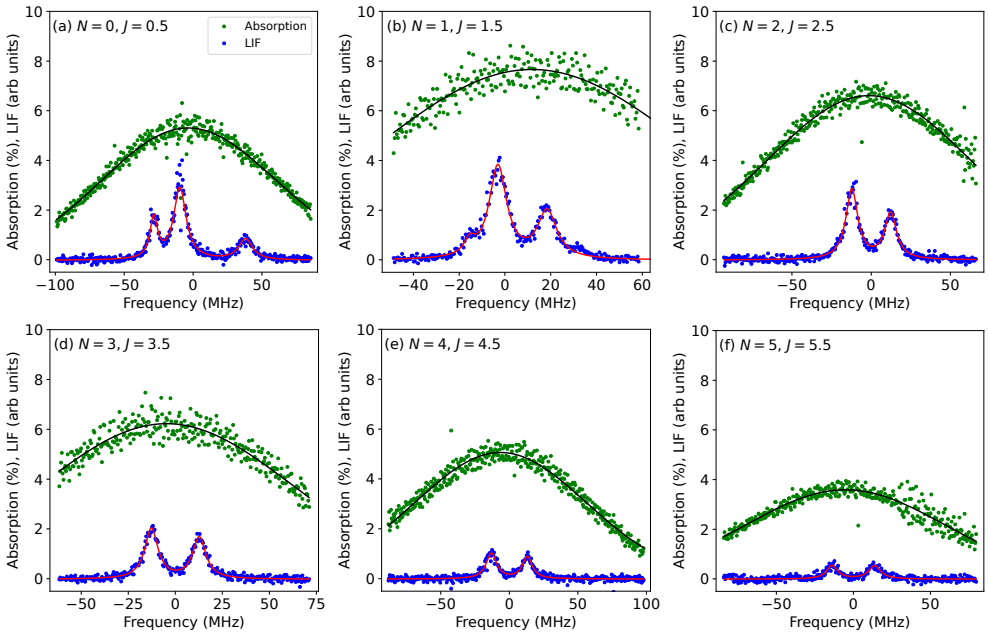

FIGURE 4.11: Spectra of the ${}^{S}R$-branch with from (a) to (f) the transitions originating from the $N = 0, J = 0.5$ to $N = 5, J = 5.5$ rotational ground states, respectively. The molecular beam is measured close by ($z = 5$ mm) and far from ($z = 780$ mm) the source exit using absorption (green) and LIF (blue) detection, respectively. Each data point originates from a single molecular beam pulse.

4

Using a transition at 815 nm results in about an order of magnitude more signal because of the increased quantum efficiency of our PMT at shorter wavelengths.

To reduce the effect of source fluctuations, the absorption signal from a second laser, which is locked on the ${}^{Q}Q(4.5)$ transition from $X^2\Sigma^+$ to the $A^2\Pi_{3/2}$ manifold, is used as reference. The fluorescence and absorption signals are shot-to-shot corrected by the reference signal, which means that short- and long-term fluctuations of the BaF yield are eliminated. The effects of a possible variation of the rotational temperature during the measurements are minimised by randomising the order in which measurements of different rotational levels and flow rates are performed.

Figure 4.11(a-f) shows the intensity of the absorption (green) and LIF (blue) as a function of the laser excitation frequency while scanning over the ${}^{S}R$ transitions originating from the $N = 0, J = 0.5$ to $N = 5, J = 5.5$ rotational ground states, respectively. Three hyperfine transitions are observed to originate from the rotational ground state $J = N + 0.5$. For $N = 1$ and higher, a fourth ${}^{S}S$ transition is possible, but this transition is well (>110 MHz) separated from the other transitions. For ${}^{S}R(2.5)$ and higher, the hyperfine splitting in the excited state is too small to resolve [32]. In Table 4.1 the transition frequencies are given.

TABLE 4.1: Measured transition frequencies between the $X^2\Sigma^+, v = 0$ and the $A^2\Pi_{3/2}, v = 0$ manifolds starting from different rotational states in the ground state. A residual Doppler shift of 0.5 MHz, resulting from the laser beam not being perfectly at right angles with the molecular beam, is subtracted. The listed uncertainty is the maximum difference between the transition frequencies obtained from spectra taken with flow rates between 30 and 70 SCCM. No systematic analysis of residual Stark and Zeeman shifts was performed. The last column gives the difference between the measured transition frequencies and those calculated using PGOPHER with the constants given in Appendix A. All frequencies are in MHz.

Lower state		Upper state	Frequency	Unc.	Diff.
$N = 0, J = 0.5, F = 1$	$\rightarrow$	$J = 1.5, F = 1$	367632135.1	0.3	0.7
$F = 1$	$\rightarrow$	$F = 2$	367632154.2	0.1	0.7
$F = 0$	$\rightarrow$	$F = 1$	367632200.9	0.2	0.1
$N = 1, J = 1.5, F = 2$	$\rightarrow$	$J = 2.5, F = 2$	367650903.8	0.5	0.8
$F = 2$	$\rightarrow$	$F = 3$	367650916.4	0.2	1.1
$F = 1$	$\rightarrow$	$F = 2$	367650938.0	0.1	0.9
$N = 2, J = 2.5, F = 3$	$\rightarrow$	$J = 3.5, F = 4$	367669431.8	0.7	1.3
$F = 2$	$\rightarrow$	$F = 3$	367669455.9	0.3	1.3
$N = 3, J = 3.5, F = 4$	$\rightarrow$	$J = 4.5, F = 5$	367687700.4	0.6	1.6
$F = 3$	$\rightarrow$	$F = 4$	367687726.0	0.2	1.7
$N = 4, J = 4.5, F = 5$	$\rightarrow$	$J = 5.5, F = 6$	367705721.2	0.7	1.4
$F = 4$	$\rightarrow$	$F = 5$	367705747.4	0.5	1.1
$N = 5, J = 5.5, F = 6$	$\rightarrow$	$J = 6.5, F = 7$	367723493.7	1.3	0.3
$F = 5$	$\rightarrow$	$F = 6$	367723521.5	2.0	0.9
$N = 6, J = 6.5, F = 7$	$\rightarrow$	$J = 7.5, F = 8$	367741019.0	0.9	-0.3
$F = 6$	$\rightarrow$	$F = 7$	367741046.5	1.3	-0.6

Due to the geometry, Doppler broadening on the transitions measured by LIF is negligible, and the spectra are well described by a Lorentzian profile. The intensity of the hyperfine transitions is found by fitting multi-Lorentzian functions to the fluorescence data, shown as the solid red lines. The transitions measured in absorption, on the other hand, is strongly Doppler broadened, and its intensity is determined by a multi-Gaussian function, with the centre frequencies and relative amplitudes determined by the fit results of the hyperfine spectra, and as free parameters the width and total amplitude. It may be observed that the measured frequency range does not cover the complete line form of the absorption spectrum, but as most fit parameters are fixed by the hyperfine transitions, the amplitudes are nonetheless determined reliably. Even with this limited frequency range, the set of measurements took about 4 hours to complete.

4.7.3 Fit of rotational temperature

To determine the rotational temperature, several methods of data treatment have been applied. Firstly, the absorption and fluorescence signals are divided by the transition

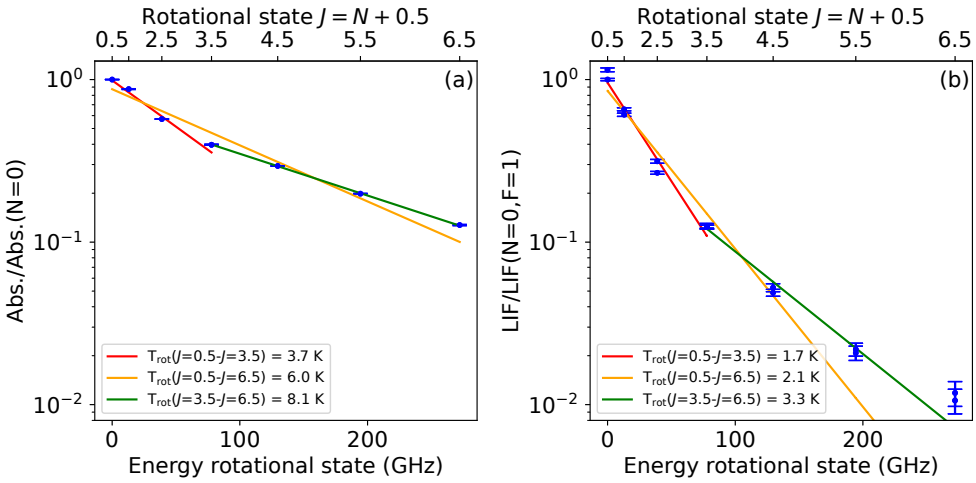

FIGURE 4.12: Fits of the rotational temperature for flow rates of (a) 20 and (b) 70 SCCM neon, measured close by and far from to the cell exit using absorption and LIF detection, respectively. The population is normalized to the population in the $J = 0.5$ states. Between the absorption and LIF detection, the population in high rotational states is cooled to lower rotational states.

strength obtained from the PGOPHER simulations, to find the population per rotational and hyperfine state, respectively. Secondly, the population is divided by the multiplicity to find the population per m_J and m_F states, because this leads to a simple exponential decay in the signal as a function of the energy of the ground state. The results are shown as the blue data points in Figure 4.12. In (a) the absorption signal measured with a flow rate of 20 SCCM is shown, while (b) shows the fluorescence signal measured with a flow rate of 70 SCCM. These measurements correspond to the most extreme conditions, that is, a few (a) or many (b) collisions. The absorption and fluorescence data are normalised to the population in a single m_J state or a single m_F state of $J = 0.5$, for clarity.

When plotted on a logarithmic scale as a function of the energy, according to Equation (4.15), the data should follow a straight line. As may be observed, this is not the case. We attribute this discrepancy to the fact that the cross-sections for inelastic (i.e., rotational state changing) collisions depend strongly on N. Typically, the cross-section drops with an increasing amount of energy that is transferred to translational energy. This is called the 'energy gap law' [83]. For high N, the energy spacing of the states is larger than for low N and consequently the cross-section for high N is smaller than that for low N. After a finite number of collisions, the population in higher states is larger than expected from the translational temperature. The higher the N state, the more pronounced the difference.

The solid orange lines in Figure 4.12(a) and (b) show the results of a linear fit

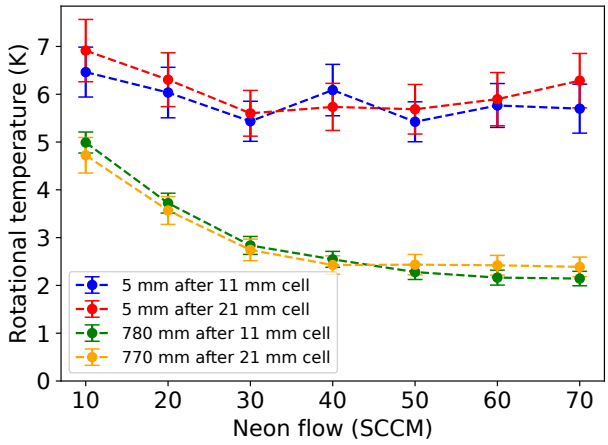

FIGURE 4.13: Rotational temperature as a function of the flow rate of the buffer gas, measured near the source exit (red and blue data points) and far away from the source exit (yellow and green data points) for cells with a length of 11 or 21 mm.

taking into account all measured rotational states resulting in a rotational temperature of 6.0 and 2.1 K, respectively. The solid red lines show the result of fits to the absorption and fluorescence data where only rotational levels up to $J = 3.5$ are taken into account, resulting in a rotational temperature of 3.7 and 1.7 K, respectively. Using only the rotational levels from $J = 3.5$ to $J = 6.5$ result in temperatures of 8.1 and 3.3 K, respectively. In the following, we will use the rotational temperature found by fitting over all measured states.

Figure 4.13 shows the rotational temperature as a function of buffer gas flow rates between 10 and 70 SCCM, measured for a cell length of 11 and 21 mm at a distance from the source exit of 5 and 780 mm (short cell) or 4 and 770 mm (long cell). Several trends are visible. First of all, the rotational temperature is lower far from the source, indicating substantial collisions beyond 5 mm of the source exit. Secondly, the rotational temperature strongly depends on the flow rate, with lower temperatures observed at high flow rates. This is particularly obvious in measurements taken far away from the source. Thirdly, within the uncertainty, no difference is observed between the short and long cells, indicating that a small decrease in the initial temperature of the buffer gas, although important for the exact longitudinal velocity of the beam (*vide infra*), does not have a big influence on the rotational temperature.

4.7.4 Rotational temperature as a function of time in the pulse

As we have seen in Section 4.5.3 and will see in Chapter 6, the temperature of the buffer gas is heated by the ablation laser pulse and cools via conduction to the cell

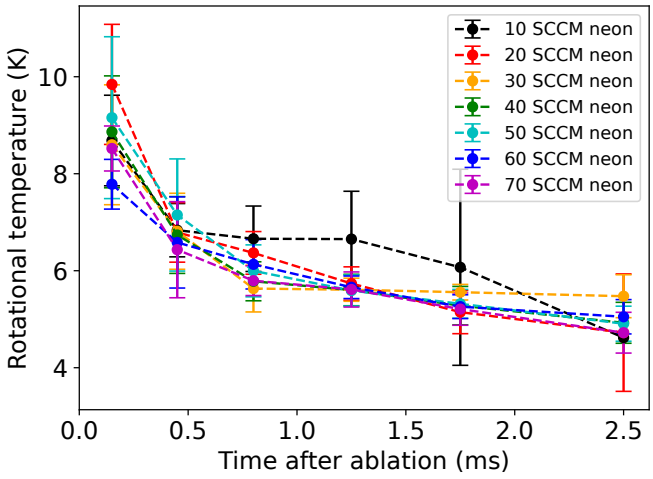

FIGURE 4.14: Rotational temperature as a function of time after firing the ablation pulse for flow rates of 10 to 70 SCCM neon. A drop in rotational temperature with time is visible, but within the limited resolution, no effect of the buffer gas flow rate is found.

walls with a typical time constant of a few hundred microseconds (depending on the cleanliness of the cell (*vide infra*)). In Figure 4.14, we show the rotational temperature, measured 5 mm after the source exit using absorption detection, as a function of time after ablation for 7 buffer gas flow rates. Due to the complex analysis and limited data, the measurements have been divided into time bins of typically 0.5 ms. As expected, the rotational temperature is higher at the beginning of the pulse. No clear dependence on the flow rate of the buffer gas is observed.

4.7.5 Vibrational temperature

In this section, we will look at the vibrational temperature, which is determined in a similar way as the rotational temperature. Three sets of transitions are measured, the $X^2\Sigma^+, v = i, N = 0, J = 1/2 \rightarrow A^2\Pi_{3/2} v = i, J = 3/2$, with $i = 0, 1, 2$, and the transition frequencies are given in Table 4.2, which also includes the hyperfine transitions of the $X^2\Sigma^+, v = i, N = 0, J = 1/2 \rightarrow A^2\Pi_{1/2} v = i, J = 1/2$, with $i = 0, 1$ transitions. Intensities are corrected for small differences in the Franck-Condon factors [15]. The blue and red data points in Figure 4.15 show the population of $v = 1$ and $v = 2$ normalised to that of $v = 0$ for flow rates of 20 and 70 SCCM. Panels (a) and (b) present the population 5 and 780 mm after the cell exit measured in absorption and fluorescence, respectively. The dashed lines show linear fits to the populations in $v = 0$ and $v = 1$ from which a vibrational temperature of 392 and 340 K is derived

TABLE 4.2: Measured transition frequencies between the $X^2\Sigma^+$ and the $A^2\Pi$ manifolds starting from the lowest rotational level of different vibrational levels in the ground state. Residual Doppler shifts are minimized by using a Doppler free measurement scheme as described in Section 5.4. The listed uncertainty corresponds to the maximum difference between spectra taken with vertical and horizontal polarized light. No systematic analysis of residual Stark and Zeeman shifts is performed. All frequencies are in MHz.

Lower state		Upper state	Frequency	Unc.
$v=0, F=1$	$\rightarrow$	$A^2\Pi_{1/2}, v=0, J=1/2, F=0$	348666402.6^a	0.3
$F=1$	$\rightarrow$	$F=1$	348666424.4^a	0.3
$F=0$	$\rightarrow$	$F=1$	348666490.0^a	0.3
$v=1, F=1$	$\rightarrow$	$A^2\Pi_{1/2}, v=1, J=1/2, F=0$	347728600.6	0.2
$F=1$	$\rightarrow$	$F=1$	347728622.3	0.5
$F=0$	$\rightarrow$	$F=1$	347728687.5	0.4
$v=0, F=1$	$\rightarrow$	$A^2\Pi_{3/2}, v=0, J=3/2, F=1$	367632135.1^a	0.3
$F=1$	$\rightarrow$	$F=2$	367632154.2^a	0.1
$F=0$	$\rightarrow$	$F=1$	367632200.9^a	0.2
$v=1, F=1$	$\rightarrow$	$A^2\Pi_{3/2}, v=1, J=3/2, F=1$	366678862.6	0.3
$F=1$	$\rightarrow$	$F=2$	366678881.9	0.2
$F=0$	$\rightarrow$	$F=1$	366678927.6	0.2
$v=2, F=1$	$\rightarrow$	$A^2\Pi_{3/2}, v=2, J=3/2, F=1$	365722742.4	0.4
$F=1$	$\rightarrow$	$F=2$	365722761.2	0.2
$F=0$	$\rightarrow$	$F=1$	365722806.8	0.7

[a] These transitions are used in the PGOPHER fit described in Table A.1.

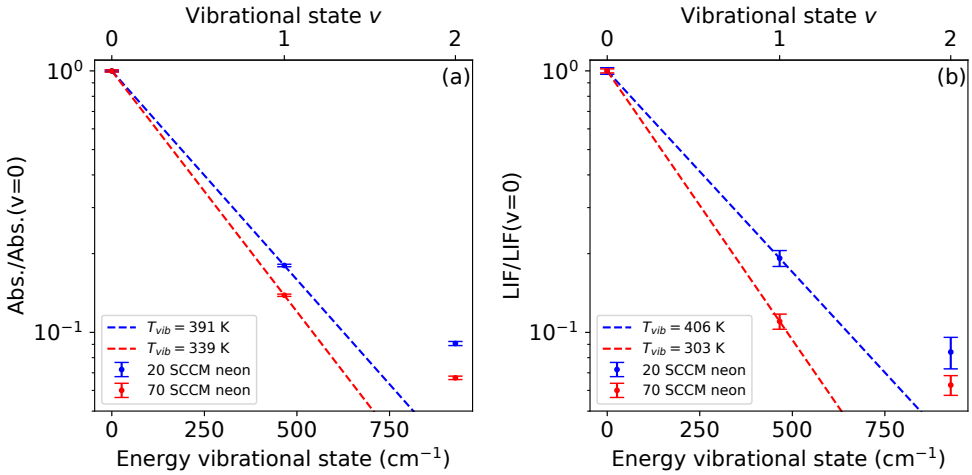

FIGURE 4.15: Population in $v = 0, 1, 2$ vibrational states relative to the population in $v = 0$ for flow rates of 20 and 70 SCCM, measured (a) close to (5 mm) and (b) far away (780 mm) from the source exit, respectively. The dashed lines show linear fits to the populations in the $v = 0$ and $v = 1$ from, which a vibrational temperature is derived.

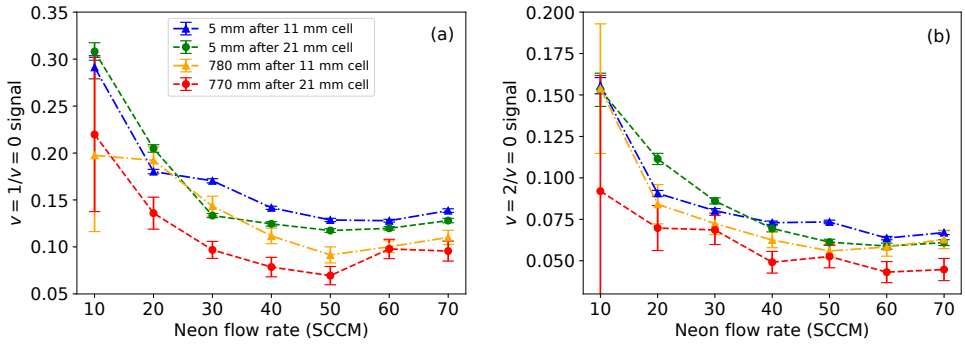

FIGURE 4.16: Population in the (a) $v = 1$ and (b) $v = 2$ vibrational state relative to the population in the $v = 0$ state as a function of buffer gas flow rate. A longer distance from the source exit and or extending the internal cell length leads to a lower population in high vibrational states.

at 5 mm behind the exit and 408 and 304 K at 780 mm behind the exit for flow rates of 20 and 70 SCCM, respectively. If the data for $v = 2$ were included in the fit, the temperature would be even higher. The high vibrational temperatures are explained by the energy gap law, i.e. the large amounts of vibrational energy cannot be taken away in translational energy, thus the cross-section for vibrational state-changing collisions is even smaller than that of rotational state-changing collisions. For low flow rates, no further vibrational cooling takes place between 5 and 780 mm from the cell exit, at higher flow rates the vibrational temperature decreases only slightly.

Figure 4.16 shows in more detail the effect of the distance from the source exit, the flow rates of the buffer gas, and the cell length on the vibrational population. Panel (a) shows the $v = 1/v = 0$ population, while panel (b) shows the $v = 2/v = 0$ population. These measurements confirm the previous observations. Somewhat surprisingly, extending the cell length has a significant effect on the vibrational temperature, whereas it had little effect on the rotational temperature. This may be understood from the fact that in a longer cell more collisions take place within the cell when the temperature of the buffer gas is close to that of the cell (typically 20 K) which is below the vibrational temperature (but above the rotational temperature) in the beam.

4.8 Number of molecules in a pulse per solid angle

In the previous sections, we have analysed multiple measurements that describe the thermodynamics of the molecular beam. In this section, we will use these methods to estimate the absolute number of molecules in a molecular pulse using absorption detection. Firstly, the density of the molecular beam is estimated. As the molecular

yield is pulsed, the temporal peak density is determined. Additionally, we notice that, because of collisions and divergence, the density is inhomogeneous, and therefore we determine the spatial peak density on the molecular beam axis. We include molecules that are not resonant with the laser frequency. Secondly, we will determine the total number of molecules of a molecular pulse, taking into account the inhomogeneous density in the transverse and longitudinal directions. Finally, in all experiments, we are interested in the number of molecules that pass through a certain aperture (typically 10 mm) at a certain distance (typically >1 m) from the molecular beam source. To be able to estimate the number of molecules far from the source, we determined the number of molecules per solid angle. This also provides a number that can be conveniently used to compare our source to other molecular beam sources. Our analysis closely follows that of Wright et al.[44] to estimate the number of aluminumfluoride molecules from their source.

The numbers shown in this section are for a molecular beam produced using typical source parameters, i.e. 8 mJ ablation pulse energy, 0.03 SCCM SF_6 flow rate, 20 SCCM neon buffer gas flow rate.

4.8.1 Density from absorption detection

The Beer-Lambert law describes how the intensity of a beam of light drops exponentially with increasing optical path length l through a molecular beam with homogeneous density n:

$$I = I_0 e^{-nl\sigma_{\mathrm{abs}}}, \tag{4.16}$$

with I the intensity of the attenuated laser beam after propagating through the medium, I_0 the initial intensity of the laser beam and σ_{abs} the absorption cross-section of the molecules, which contains all information about the transition strength. In the case where the laser beam crosses the molecular beam with width Δx multiple times M, we can use that $l = M\Delta x$. Typically, in our measurements, $M = 2$.

Our molecular beam has an inhomogeneous density over the spatial beam profile of the absorption laser, and in that case, the transmitted intensity is equal to:

$$I = I_0 e^{-\sigma_{\mathrm{abs}} M \int n(x)dx}, \tag{4.17}$$

with $n(x)$ the density as a function of position along the direction of the laser beam, which we define as the x-direction.

In terms of the fraction of absorption of light A, we find:

$$A = \frac{I_0 - I}{I_0} = 1 - e^{-\sigma_{\mathrm{abs}} M \int n(x)dx}. \tag{4.18}$$

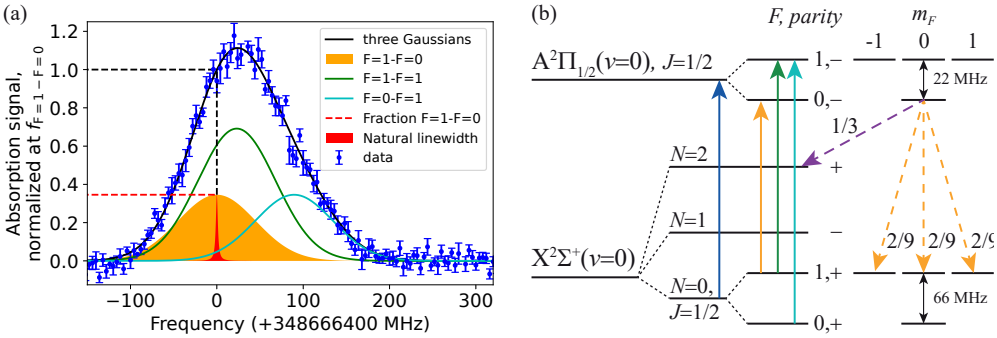

FIGURE 4.17: Rotational and hyperfine transitions between the $X^2\Sigma^+, v = 0, N = 0, J = 1/2$ and $A^2\Pi_{1/2}, v = 0, J = 1/2$ rotational states. (a) Measured absorption spectrum (blue) and fitted spectrum (black) containing three hyperfine transitions (orange, green, light blue) as indicated in the energy diagram of (b). The branching ratios are found in Ref. [91].

The average molecular density over an optical path length between a and b is:

$$\bar{n} = \frac{1}{\sigma_{\text{abs}} M \int_a^b dx} \ln\left(\frac{I_0}{I}\right) = \frac{1}{\sigma_{\text{abs}} M \int_a^b dx} \ln\left(\frac{1}{1-A}\right). \tag{4.19}$$

4.8.2 Absorption cross-section

The absorption cross section σ_{abs} contains all the information about the molecule-light interaction. For a closed (atomic) transition with equal multiplicity in the ground and excited states, the absorption cross-section is equal to [88]:

$$\sigma_{\text{abs, closed trans.}} = \frac{\lambda^2}{2\pi} = 1.18 \times 10^{-13}\ \text{m}^2 \tag{4.20}$$

with $\lambda = 860$ nm, the laser excitation wavelength. This remarkably simple formula describes the absorption process as a collision between a fuzzy ball (the photon) with a radius about equal to λ and an atom that is small compared to λ [89, 90].

Equation (4.20) only holds for closed transitions. However, the excited (molecular) state that we address, the $A^2\Pi_{1/2}, J = 1/2$ state, can decay to other states. The absorption cross-section is then multiplied by the ratio of multiplicity in the excited and ground states and the branching ratios:

$$\sigma_{\text{abs}} = \frac{\lambda^2}{2\pi} \frac{2(J,F)_{\text{e}} + 1}{2(J,F)_{\text{g}} + 1} \xi \mathcal{FC}_{v(0,0)}, \tag{4.21}$$

where $(J,F)_{\text{e}}$ and $(J,F)_{\text{g}}$ are the rotational or hyperfine excited and ground states, respectively. ξ is the rotational branching ratio and $\mathcal{FC}_{v(0,0)}$ the Franck-Condon factor,

Transition $A \to X$	$\frac{2(J,F)_e+1}{2(J,F)_g+1}$	ξ
$J = 1/2 \quad \to N = 0$	2/2	2/3
$J = 1/2 \quad \to N = 2$		1/3
$J = 1/2, F = 0 \to N = 0, F = 1$	1/3	6/9
$J = 1/2, F = 1 \to N = 0, F = 0$	3/1	2/9
$J = 1/2, F = 1 \to N = 0, F = 1$	3/3	4/9

TABLE 4.3: Branching ratios and multiplicity of the three hyperfine transitions between the $A^2\Pi_{1/2}, J = 1/2$ and the $X^2\Sigma^+, N = 0, J = 1/2$ states. Values found in Ref. [91].

the vibrational branching ratio between the $A^2\Pi_{1/2}, v = 0$ and $X^2\Sigma^+, v = 0$ manifolds, which is 0.9601 in BaF [15].

For the rotational transition $A^2\Pi_{1/2}, v = 0, J = 1/2 \to X^2\Sigma^+, v = 0, N = 0, J = 1/2$, the branching ratio $\xi = 2/3$, because 1/3 of the molecules decay to $N = 2$, see Table 4.3. Note that although the absorption laser drives molecules from the ground to the excited state, we show here the transition from an excited state to a ground state as the branching ratios are determined by the spontaneous decay channels.

Doppler broadening and hyperfine structure

Figure 4.17(a) shows an absorption spectrum, where the laser frequency is scanned over the $X^2\Sigma^+, N = 0, J = 1/2 \to A^2\Pi_{1/2}, J = 1/2$ rotational transition. The blue points show the amount of light absorbed, averaged over the duration of the molecule pulse. Figure 4.17(b) presents the corresponding energy diagram, with the blue arrow indicating the rotational transition.

Because of the transverse velocity of the molecular beam, the transition is Doppler broadened, hiding its hyperfine substructure. However, we know from our own narrow-line fluorescence measurements (see Table 4.2 and Figure 3.7(a)) that the energy splitting due to the hyperfine structure is comparable with the Doppler broadening, thus ignoring the hyperfine structure would lead to an overestimation of the Doppler broadening. To find the correct Doppler broadening, a triple Gaussian function is fitted with fixed amplitude ratios and frequency offsets and a common line profile representing broadening, resulting in the black curve in Figure 4.17(a). The individual contributions of the three hyperfine transitions, $F = 1 \to F = 0$, $F = 1 \to F = 1$ and $F = 0 \to F = 1$, are shown in orange, green, and cyan, respectively. In this specific measurement, fitting a single Gaussian function would lead to an overestimation of the Doppler broadening of $\sim$10 MHz.

As the hyperfine splitting is similar to the Doppler broadening, at a specific excitation frequency, the contributions of each of the hyperfine transitions to the total absorption

signal vary. This means that using the rotational branching ratio is not correct. Instead, the branching ratios for the different hyperfine transitions are determined; see Table 4.3.

The fraction η of the measured signal that can be attributed to a specific hyperfine transition varies with excitation frequency, as Doppler broadening causes some, but not complete, overlap of hyperfine transitions. At the frequency of the resonant transition $F = 1 \rightarrow F = 0$, this transition contributes $\eta \approx 34$ % to the total absorption signal of molecules in $N = 0$. In Figure 4.17(a) this fraction is highlighted by normalising the absorption signal at the mean $F = 1 \rightarrow F = 0$ transition frequency. Without hyperfine structure, the $F = 0 \rightarrow F = 1$ transition would contribute much stronger and only 1/4 of the signal could be attributed to the $F = 1 \rightarrow F = 0$ transition.

Using the branching ratios of the $F = 1 \rightarrow F = 0$ transition, we calculate the number of molecules in the $F = 1$ hyperfine state. The number of molecules in the $N = 0, J = 1/2$ *rotational* ground state, also includes the molecules in the $F = 0$ hyperfine state. Therefore, we should multiply the calculated number of molecules in the $F = 1$ by:

$$\chi = \frac{2F_{F=1} + 1 + 2F_{F=0} + 1}{2F_{F=1} + 1} = \frac{4}{3}, \tag{4.22}$$

taking into account the multiplicity of the hyperfine states.

In conclusion, to determine the number of molecules in the rotational state $N = 0, J = 1/2$, we measure the absorption at the $F = 1 \rightarrow F = 0$ resonant frequency, use $\eta \approx 34$ % of the measured signal and multiply by a factor $\chi = 4/3$.

4.8.3 Including non-resonant molecules

It may be clear from Figure 4.17(a), that most molecules (orange area) are *not* resonant with a single laser frequency (red area). To include the non-resonant molecules, we have to multiply the number of resonant molecules by a factor α such that:

$$\alpha \int (\text{resonant}) = \int (\text{Doppler broadened}) \tag{4.23}$$

$$\alpha \int (\text{Lorentzian}) = \int (\text{Gaussian}) \tag{4.24}$$

$$\alpha \frac{\pi \gamma_{\text{FWHM}}}{2} = \frac{D_{\text{FWHM}} \sqrt{2\pi}}{2\sqrt{2\ln(2)}}, \tag{4.25}$$

with γ the natural linewidth, which is defined as the FWHM of the Lorentzian distribution [92] and D_{FWHM} the FWHM width of the Gaussian Doppler broadened distribution.

Consequently, α:

$$\alpha = \frac{1}{\sqrt{\pi \ln(2)}} \frac{D_{\text{FWHM}}}{\gamma_{\text{FWHM}}} \approx 0.68 \frac{108}{2.79} = 26. \tag{4.26}$$

The term:

$$\frac{1}{\sqrt{\pi \ln(2)}} = 0.68 \tag{4.27}$$

is necessary to account for the different shapes of the frequency distributions. The factor 26 tells us that for every molecule that is resonant with the frequency of the laser beam, there are 26 times more molecules (in the same state) that are not resonant. If one uses a transition to a short-lived excited state (for instance, the $A^1\Pi$ state in aluminumfluoride [44]), at the same column density the measured absorption is much stronger, but α will be correspondingly smaller. Note that Doppler broadening leads to absorption of light via other transitions, but we have corrected for this via the η factor described before.

4.8.4 Peak absorption and density

Combining the previous sections and using Equation (4.19), we find, for a peak absorption of 12% (see Figure 4.1, 20 SCCM neon), a peak density:

$$n = \frac{1}{M}\frac{1}{l\sigma_{\mathrm{abs}}}\eta\chi \ln\left(\frac{1}{1-A}\right)\alpha \approx 6.3 \times 10^9 \text{ molecules/cm}^3 \tag{4.28}$$

in the $N = 0, J = 1/2$ rotational ground state, including non-resonant molecules. Here we assume an optical path length of the laser beam through the molecular beam of 4.5 mm, which is the diameter of the aperture of the cell.

4.8.5 Number of molecules in a pulse

The number of molecules follows from the integration of the spatially dependent density over the volume of the molecules. We define the x direction to be the direction of the absorption laser, which is aligned horizontally and perpendicular to the molecular beam. The y-direction is vertically perpendicular to the molecular beam. The z-direction is in the forward-moving molecular beam direction.

We find than that the total number of molecules is:

$$\mathcal{N} = \int\int\int dxdydz \frac{1}{M\Delta x(y)}\frac{1}{\sigma_{\mathrm{abs}}}\eta\chi \ln\left(\frac{1}{1-A}\right)\alpha. \tag{4.29}$$

In the z-direction, i.e. the forward direction, the effective beam size follows integrating the time of flight of the molecular pulse of Figure 4.1, multiplied by the forward velocity $v_\parallel$:

$$\int dz\, n(z) = \int n(t) v_\parallel dt, \tag{4.30}$$

where we simplify the calculation by assuming that $v_{\parallel}$ is time independent. In Chapter 6 we show that this is not completely the case, but the error made in this calculation of the brightness is expected to be small. From a Gaussian fit on the velocity distribution, we find a mean forward velocity of 207 m/s.

In the transverse direction, the exact molecular density is hard to estimate but, as we shall see, it is not necessary to know. The relevant parameter is the total absorption signal in the x and y-direction combined and this follows from the integral over the molecular beam size measurement presented in Figure 4.9:

$$\int\int n(x,y)dxdy \propto \int A(y)dy = \sqrt{\pi}\sigma_y A(y=0) = 3.3A(y=0). \tag{4.31}$$

The integral in the x-direction drops out, as a single-pass optical path length is always equal to the effective transverse beam size.

Rewriting Equation (4.29) gives the number of molecules per pulse:

$$\mathcal{N} = \frac{\sqrt{\pi}\sigma_y}{M}\frac{1}{\sigma_{\rm abs}}v_{\parallel}\eta\chi\int \ln\left(\frac{1}{1-A(t)}\right)dt \;\alpha \approx 1.8\times 10^{10}\ \text{molecules} \tag{4.32}$$

in the $N=0, J=1/2$ rotational ground state with a repetition rate of 10 Hz.

4.8.6 Brightness of the molecular beam

To estimate the number of molecules far from the source exit and to facilitate comparisons with the literature, we will now calculate the brightness using the solid angle derived with Equation (4.14). In our situation, the beam has a transverse velocity $v_{\perp}$ of 93 m/s (FWHM) and a mean forward velocity $v_{\parallel}$ of 207 m/s and hence a solid angle of 0.15 sr. This leads to a brightness $\mathcal{B}$ of the source in the ground state $N=0$ of:

$$\mathcal{B} = 1.2\times 10^{11}\ \text{molecules/sr/pulse}, \tag{4.33}$$

with a repetition rate of 10 Hz.

4.8.7 Discussion on the brightness as a function of distance from the source.

We have measured the molecular signal close to the cell exit using absorption detection and far from the source using LIF detection. The absorption signal is used to calculate the absolute number of molecules, due to the robust method presented above. In Chapter 6 we will focus on the information that can be obtained from the fluorescence signal. Here we verify that the intensities measured with both methods as a function of the flow rate of the buffer gas are consistent. In Figure 4.18 the signals measured

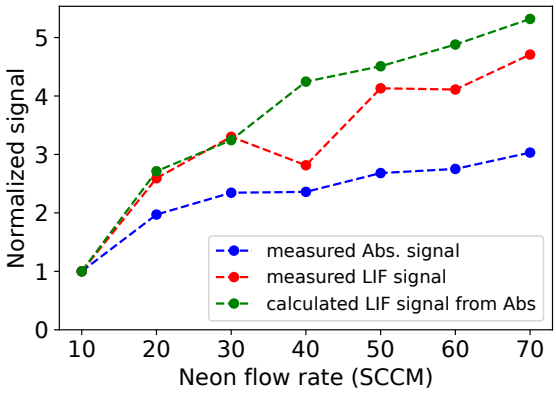

FIGURE 4.18: Comparision between the Absorption and LIF signal as a function of buffer gas flow rate. Due to collisions, the divergence and rotational temperature changes. The effect is smallest for low buffer gas flow rates and therefore the intensity is normalized for the signal measured at 10 SCCM neon flow. Taking into account the measured divergence and rotational cooling, the strength of the LIF signal is calculated from the absorption signal, which is well in agreement with the measured LIF signal.

with the absorption detection (blue data) and LIF detection (red) data are presented, normalised to the data measured with a flow rate of 10 SCCM. It may be observed that, at high flow rates, the fluorescence signal is relatively much stronger than the absorption signal. For a long time, this presented us with a puzzle, but this is explained by the measurements presented in Section 4.5 and Section 4.7.

In Section 4.5 and Section 4.7, we have seen that collisions take place after the absorption measurement at 5 mm from the source exit, leading to increased beam divergence and to a higher population in the rotational state $N = 0$, respectively. These effects have the opposite effect on the brightness of the beam, but while the extra divergence is almost constant with the buffer gas flow rate, the population in $N = 0$ increases significantly for higher flow rates. The green data points are the result of multiplying the absorption signal with the correction factors obtained from the measurements in Section 4.5 and Section 4.7. As may be observed, the green line is close to the measured LIF signal. The difference observed at high flow rates is likely due to losses caused by collisions with the background gas as a result of the limited pumping capacity.

4.9 Conclusions

In this chapter, I have analysed the molecular beam in detail, focussing on the transverse velocity distribution, the rotational and vibrational temperatures, the density and the

absolute number of molecules in the beam. The longitudinal velocity is the topic of Chapter 5 and Chapter 6. An overview of all molecular beam properties will be given in the final chapter Chapter 7.

5 A method to determine the phase-space distribution of a pulsed molecular beam

5.1 Abstract

We demonstrate a method to determine the longitudinal phase-space distribution of a cryogenic buffer gas cooled beam of barium-fluoride molecules based on a two-step laser excitation scheme. Temporal resolution is achieved by a transversely aligned laser beam that drives molecules from the ground state $X^2\Sigma^+$ to the $A^2\Pi_{1/2}$ state around 860 nm, while the velocity resolution is obtained by a laser beam that is aligned counter-propagating with respect to the molecular beam and that drives the Doppler shifted $A^2\Pi_{1/2}$ to $D^2\Sigma^+$ transition around 797 nm. Molecules in the D-state are detected background-free by recording the fluorescence from the $D - X$ transition at 413 nm. A temporal resolution of 11 μs and a velocity resolution of 6 m/s is obtained. In order to calibrate the absolute velocity, we have determined the Doppler free transition frequencies for the $X - A$ and $X - D$ transitions with an absolute accuracy below 0.3 MHz. The high resolution of the phase-space distributions allows us to observe a variation of the average velocity and velocity spread over the duration of the molecular beam pulse. Our method hence gives valuable insight into the dynamics in the source.

5.2 Introduction

Cold molecules offer unique possibilities for precision tests of fundamental physics theories [5, 10, 11] , quantum technology [93–96], and studies of quantum effects in molecular collisions [97, 98]. Successful methods to create cold molecules include the deceleration of molecular beams using electric fields via the Stark effect [18, 19], magnetic fields via the Zeeman effect [19, 99, 100], and laser cooling using near resonant light [101–103]. The phase-space density – the number of molecules per position and velocity interval – of decelerated molecular beams is proportional to, and for Stark and Zeeman deceleration limited by, the phase-space density of the initial beam [19]. Therefore, the success of deceleration techniques depends crucially on

This chapter is based on Maarten C. Mooij *et al.* "A method to determine the phase-space distribution of a pulsed molecular beam", 2025 *J. Phys. B: At. Mol. Opt. Phys.* **58** 015303

the brightness of the initial beam. Furthermore, as there is a compromise between the number of molecules that are decelerated and the deceleration rate, it is highly desirable that the beam has a low initial velocity. An effective way to create intense, slow beams of molecules and molecular radicals is the so-called cryogenic buffer gas cooled beam source, first introduced by Maxwell *et al.* [49] and further developed by Patterson *et al.* [50], van Buuren *et al.* [52], Hutzler *et al.* [37], Truppe *et al.* [40] and others. Over the last few years, we have constructed a cryogenic buffer gas cooled beam source that provides barium monofluoride (BaF) molecules for an experiment that will search for the electron's electric dipole moment (*e*EDM) [12]. In the experiment, BaF molecules will be decelerated using a 4.5 m long travelling-wave Stark decelerator. In order to decelerate a reasonable fraction of the molecular beam, the velocity spread of the initial beam should be small, while the average forward velocity should be below $\sim$200 m/s[12]. Note that, the length of the decelerator needed to bring molecules to rest scales with the initial velocity squared; if, instead of 200 m/s, the velocity of the beam would be 230 m/s, we would need a decelerator with a length of 6 m in order to have the same acceptance. Therefore, accurate knowledge of the velocity distribution is crucial while optimising the intensity of the source.

A simple and general way to obtain the longitudinal velocity distribution is by measuring the time-of-flight profile of the molecular beam at two positions along the molecular beam path. The average velocity of the beam is determined from the time difference in the mean of these distributions, while the velocity spread is determined from the difference of their widths. This method works well if the molecular beam pulse is short compared to the flight path or if the velocity of the molecules is independent of the time they exit the source and accurately described by a Gaussian distribution [104].

A more direct method to measure the velocity distribution is by measuring the Doppler shift of a transition using a laser beam that is counter-propagating with respect to the molecular beam. A downside of this method is that molecules will already be excited and may decay into dark states before the detection zone is reached. This effect will limit the signal strength that is obtained. Furthermore, as slow molecules are more likely to be pumped away, the measurement may not accurately reflect the true velocity distribution [46]. Optical pumping can be reduced by introducing a small angle between the molecular beam and the laser [36], which however, complicates the interpretation of the measurement as in this situation the detection volume will not be well defined. A more serious problem arises when the hyperfine splitting of the observed transition is comparable to the Doppler profile, resulting in different velocity components being excited at the same frequency of the light. In such a case, the integrated velocity distribution of the beam can still be obtained by a deconvolution procedure, but it is not possible to measure the velocity distribution at a specific time in the pulse.

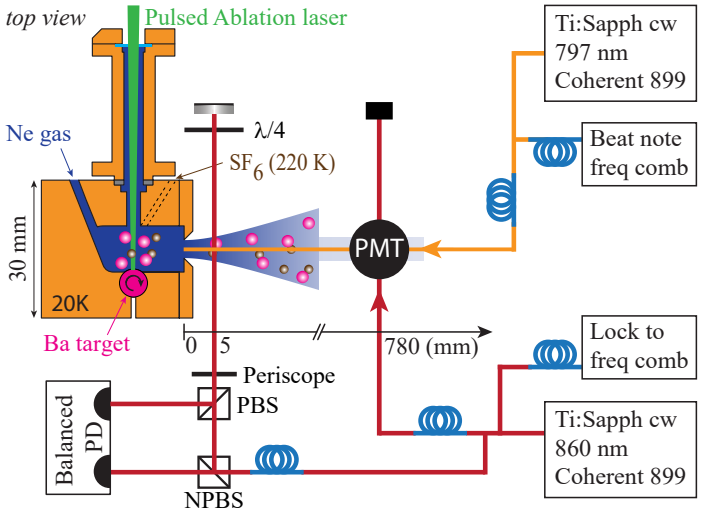

FIGURE 5.1: Schematic view of the experimental setup showing the cryogenic buffer gas cooled beam source and the lasers used for absorption and fluorescence detection. Barium monofluoride molecules are created inside the cell and expand into the vacuum to form a molecular beam. The performance of the source is monitored via absorption detection 5 mm behind the cell. The phase-space distribution of the beam is recorded 780 mm after the cell using a two-step laser excitation scheme. In the first step, BaF is brought to an excited state, independently of their forward velocity, but at a well-defined position along the molecular beam path using a laser beam that is perpendicular to the molecular beam. In the second step, the longitudinal velocity of molecules in this excited state is measured using a laser beam that is counter-propagating with respect to the molecular beam. Fluorescence back to the ground state is measured using a photomultiplier tube (PMT).

In this paper, we use a two-step laser excitation scheme, that was pioneered by Barry *et al.* [105] and Hemmerling *et al.* [106] to study the velocity distribution of laser cooled beams of SrF and CaF, respectively. In the first step, molecules are brought to an excited state, independent of their forward velocity, at a well-defined position along the molecular beam path using a laser beam that is perpendicular to the molecular beam. In the second step, the longitudinal velocity of molecules in this excited state is measured using a laser beam that is counter-propagating with respect to the molecular beam. This scheme avoids the problems mentioned above. We use this method to determine the phase-space distribution of a cryogenic buffer gas cooled beam source of BaF molecules with high accuracy.

5.3 Method

Figure 5.1 shows a schematic of our method including the top-view of our cryogenic buffer gas cooled beam source and the optical beam paths. The design of our cryogenic

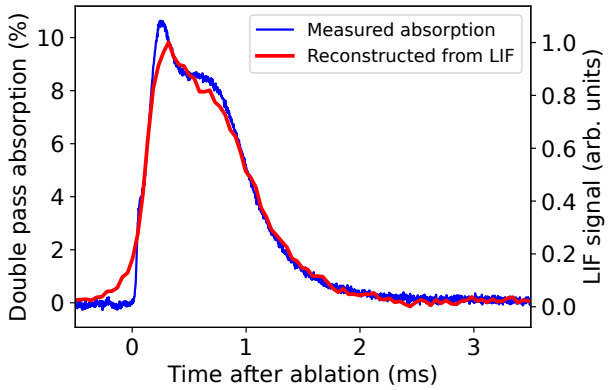

FIGURE 5.2: Simultaneously measured absorption and reconstructed fluorescence data as a function of time after ablation. The blue line presents the double-pass laser absorption signal measured 5 mm behind the exit of the source. The red line corresponds to the time-of-flight of the molecules that is reconstructed from the phase-space distribution measurement further downstream the molecular beam path, with the vertical scale adjusted to match the absorption measurement.

source is based on that of Truppe et al. [40]. The heart of our setup is formed by a cubical copper cell kept at a temperature of around 20 K using a 2-stage cryo-cooler (Sumitomo Heavy Industries, cold head RP-082B2S). A continuous flow of pre-cooled neon is passed through the cell at a flow rate of 20 standard cubic centimeter per minute (SCCM) [2]. Within the cell, barium atoms are ablated by a pulsed Nd:YAG laser (532 nm, 5 ns pulse, 10 Hz, 8 mJ per pulse) from a rotating solid Ba target. The barium atoms in the plasma plume react with sulphur hexafluoride (SF_6) molecules, that are injected into the cell with a flow rate of typically 0.03 SCCM from a copper tube that is kept at a temperature of 220 K. The BaF molecules created in this reaction are cooled via collisions with the neon atoms and form a molecular beam by expanding through a 4.5 mm diameter orifice into vacuum. The cell is surrounded by a copper and an aluminium shield, at temperatures of 6 K and ∼30 K, respectively. Besides acting as heat shields, these cylinders provide the necessary pumping capacity to allow pressures on the order of 10^{-2} mbar inside the cell, while maintaining a pressure below 10^{-6} mbar in the molecular beam chamber.

To monitor the performance of the source, the BaF molecules are detected using absorption 5 mm behind the cell on the $X^2\Sigma^+, N = 0, J = 1/2 \rightarrow A^2\Pi_{1/2}, J = 1/2$ transition using a laser beam with a full with at half maximum (FWHM) diameter of 1 mm and a power of ∼1 µW near 860 nm from a Ti:Sapphire laser. Figure 5.2 shows a typical absorption measurement (blue curve) together with a time-of-flight

[2] 1 SCCM = 4.48×10^{17} particles/s

measurement that is reconstructed from laser-induced fluorescence measurements recorded simultaneously (red curve), which will be discussed later. The absorption profile displays a pronounced feature at early times that may be understood by looking at the phase-space distribution presented in Section 5.6. The absorption signal can be converted into an absolute number by taking into account the spatial and velocity distributions of the beam in the longitudinal and transverse directions, using a procedure that is similar to the one described by Wright *et al.* [44]. The duration of the molecular beam pulse is about 1 ms and the peak absorption is 10% (double pass), which corresponds to $1.9(6) \times 10^{10}$ BaF molecules in the $N = 0$ state per pulse and $1.3(5) \times 10^{11}$ molecules per sr per pulse.

At a distance of 780 mm from the source, in a second, differentially pumped, vacuum chamber, the molecules are excited by light from two Ti:Sapphire lasers (Coherent 899) that are referenced to a frequency comb (Menlo Systems FC1500-250-WG) that is stabilized to a caesium clock (Microsemi CSIII Model 4301B). The beat note of the lasers with the frequency comb is recorded every molecular shot with a Siglent SSA3021X spectrum analyser with an accuracy of typically 1.1 MHz. One of the lasers is aligned perpendicular to the molecular beam and is resonant with the $X^2\Sigma^+ \rightarrow A^2\Pi_{1/2}$ transition around 860 nm, while the other laser is aligned to be counter-propagating with respect to the molecular beam and resonant with the $A^2\Pi_{1/2} \rightarrow D^2\Sigma^+$ transition around 797 nm. The frequency of the second laser is red-shifted with respect to the transition frequency to compensate for the Doppler shift. From this detuning, we can infer the longitudinal velocity of the molecules. Note that, rather than two subsequent one-photon transitions, the excitation process can be described as a two-photon transition from the X to D-state that is enhanced by the intermediate A-state. Any detuning of the laser that is used to drive the $X - A$ transition, can be compensated by an equal but opposite detuning of the laser that is used to drive the $A - D$ transition. Therefore, frequency stabilization of both lasers is equally important.

Figure 5.3 shows the energy levels of ^{138}BaF relevant for our experiment. The lowest rotational level of the $X^2\Sigma^+$ manifold, the $N = 0, J = 1/2$ state, is split into two hyperfine components, $F = 0$ and $F = 1$, due to the nuclear spin of the fluorine atom. The two components are separated by 65.8 MHz [107]. We drive a transition from the $X^2\Sigma^+, N = 0, J = 1/2, F = 1$ state to the $A^2\Pi_{1/2}, J = 1/2, F = 0$ state using light around 860 nm. In the A-state, the $F = 0$ and $F = 1$ levels are separated by 21.87 MHz [32], sufficiently large to selectively drive a transition to the $F = 0$ level using a laser beam that is perpendicular to the molecular beam. From the $A^2\Pi_{1/2}, J = 1/2, F = 0$, we drive a transition to the $D^2\Sigma^+, N = 0, J = 1/2, F = 1$ around 797 nm using a second laser that is aligned to be counter-propagating with respect to the molecular beam. Note that, while the hyperfine splitting in the D-state

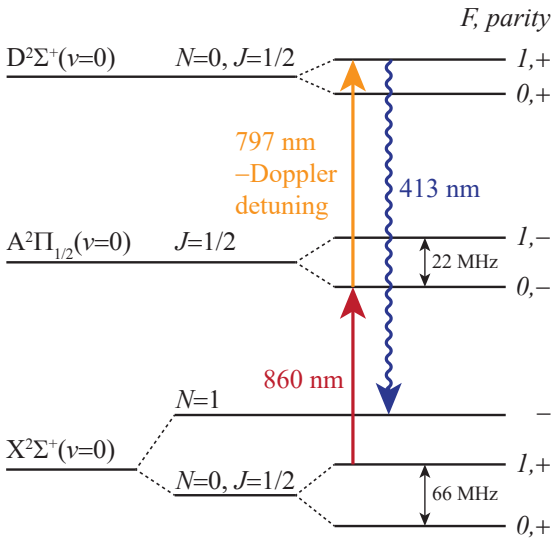

FIGURE 5.3: Energy level scheme of ^{138}BaF showing the relevant energy levels. Barium fluoride molecules are exited to the D-state using two lasers around 860 nm and 797 nm. Molecules are detected using the fluorescence from the D-state back to the X-state at 413 nm.

is small, we can be sure to drive a single transition as the $A^2\Pi_{1/2}, J = 1/2, F = 0 \rightarrow D^2\Sigma^+, N = 0, J = 1/2, F = 0$ transition is not allowed[3].

Once excited to the D-state, part of the molecules will decay back to the ground state by emitting a photon at 413 nm which is efficiently detected using a photomultiplier tube (PMT) (Thorn EMI 9558 QB). A bandpass filter around 400 nm (Thorlabs FBH400-40) is used to filter out scattered photons from the laser beams and unwanted fluorescence, resulting in a nearly background-free detection [108].

The laser used for driving the $X - A$ transition has a power of typically 0.1 mW in a beam with a FWHM diameter of 2.2 mm, corresponding to a peak intensity of ~ 2 mW/cm^2. This intensity is sufficient to obtain a good signal-to-noise ratio, while avoiding off-resonant excitation. The laser used for driving the $A - D$ transition has a power of about 10 mW in a beam with a FWHM diameter of 2.2 mm, corresponding to a peak intensity of $\sim 2\times10^2$ mW/cm^2. This intensity is sufficient to obtain a good signal-to-noise ratio, while avoiding power broadening which would lead to a decrease of the velocity resolution. Note that the intensity of the laser used to drive the $A - D$ transition is 100 times larger than that used to drive the $X - A$ transition as the

[3]We have explicitly looked for hyperfine structure in the D state by using the $A^2\Pi_{1/2}, J = 1/2, F = 1$ as intermediate state but were unable to resolve it within our experimental linewidth of 5 MHz (FWHM). The mean transition frequency from X via $A, F = 0$ to only $D, F = 1$ agrees within the uncertainty of 170 kHz to the mean frequency when measuring a transition from X via $A, F = 1$ to both $D, F = 0, 1$.

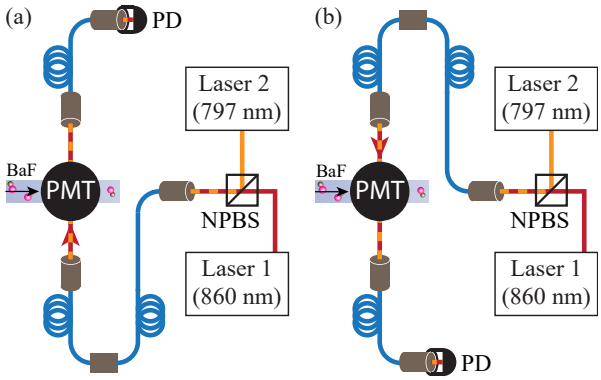

FIGURE 5.4: Experimental scheme for overlapping the path of two counter-propagating laser beams, which is used for measuring Doppler-free transition frequencies in a molecular beam. Two lasers are combined using a non-polarizing beam splitter (NPBS) and are coupled into an optical fiber. Using a mating sleeve, this fiber is connected to a second fiber that brings the light to the right-hand side (a) or the left-hand side (b) of the molecular beam setup. After crossing the molecular beam, the laser beams are coupled into a third optical fiber which is connected to a photodiode (PD). By exchanging the first fiber with the photodiode, we can reverse the direction of the light, and hence the sign of the residual Doppler shift.

excitation process needs to compete with the rapid decay of the A-state (which has a lifetime of 57.1 ns [74]) back to the ground state.

Essential for our method is that molecules are only excited to the D-state at the exact location where the two lasers overlap; the laser that addresses the $X - A$ transition, which is aligned perpendicular to the molecular beam, determines the spatial resolution along the molecular beam axis and hence the temporal resolution, while the laser that addresses the $A - D$ transition, which is aligned counter-propagating with respect to the molecular beam, determines the velocity resolution. In this way, problems with optical pumping are avoided.

5.4 Doppler free transition frequencies

It is important to know the exact (Doppler-free) transition frequency of the $X - D$ transition accurately, as we relate the measured Doppler shifted frequency to the velocity. We have also measured the Doppler-free transition frequency of the $X - A$ transition to ensure that the 860 nm laser is aligned perfectly perpendicular to the molecular beam axis.

Figure 5.4 shows the setup used to determine the Doppler-free transition frequencies. Using a non-polarizing beam splitter (NPBS), the two lasers used for driving the $X - A$ and $A - D$ transitions are coupled into a single optical fiber. Using a mating sleeve, this fiber is connected to a second fiber that brings the light to the right-hand side

TABLE 5.1: Measured transition frequencies of the $X - D$ and $X - A$ transitions with standard deviation. The $A - D$ transition frequency is found by taking the difference between the $X - D$ and $X - A$.

Transition	Frequency (MHz)
$X^2\Sigma^+, N = 0, J = 1/2, F = 1 \rightarrow D^2\Sigma^+, N = 0, J = 1/2, F = 1$	724795734.10(14)
$X^2\Sigma^+, N = 0, J = 1/2, F = 1 \rightarrow A^2\Pi_{1/2}, J = 1/2, F = 0$	348666402.6(3)
$A^2\Pi_{1/2}, J = 1/2, F = 0 \quad \rightarrow D^2\Sigma^+, N = 0, J = 1/2, F = 1$	376129331.5(3)

(shown in Figure 5.4(a)) or the left-hand side (shown in Figure 5.4(b)) of the molecular beam setup. The laser beams are subsequently coupled out of the fiber and aligned such that they cross the molecular beam below the PMT. After crossing the molecular beam, the laser beams are coupled into a third optical fiber which is connected to a photodiode. Typically, 10 % of the light that exits the second fiber is collected back into the third fiber. By exchanging the first fiber with the photodiode, we can reverse the direction of the light, i.e., we can switch between the situation depicted in Figure 5.4(a) and Figure 5.4(b). This procedure ensures that the path followed by the lasers in Figure 5.4(a) and Figure 5.4(b) exactly overlap. We estimate that the angle between the two laser beams coming from opposite directions is below 5×10^{-3} degrees, which for a 200 m/s beam corresponds to an uncertainty on the Doppler-free $X - A$ transition frequency of below 10 kHz. Our method is a simplified version of the one recently employed by Wen *et al.* [109] to perform spectroscopy in a beam of metastable helium.

The fact that the beam paths overlap does not imply that the lasers are exactly perpendicular to the molecular beam, i.e. the $X - D$ transition frequency measured with the laser beam coming from the right side might be Doppler shifted. However, this Doppler shift will be opposite to the one measured with the laser beam coming from the left side. The Doppler-free $X - D$ transition frequency is found by taking the average of the two measurements. The spectra were fitted to a Lorentzian function with a width of $\sim$5 MHz resulting from the transverse velocity spread of the beam and the finite lifetime of the D-state. We have performed several of these measurements, using both vertical and horizontal polarization, over multiple days. The error is conservatively taken to be 0.3 MHz, the maximum deviation of the weighted mean. This error is mainly limited by the lack of control over magnetic and electric fields in the interaction zone. The Doppler-free $X - A$ transition was obtained by following the same procedure, but by leaving out the filter in front of the PMT and having the 797 nm laser blocked.

The obtained transition frequencies are listed in Table 5.1 with the standard deviation quoted between brackets. Our value for the $X^2\Sigma^+, N = 0, J = 1/2, F = 1 \rightarrow D^2\Sigma^+, N = 0, J = 1/2, F = 1$ transition may be compared with the term energy determined by Effantin *et al.* [110] from fluorescence spectra of highly excited rotational levels in the D-state. Our value is two orders in magnitude more accurate

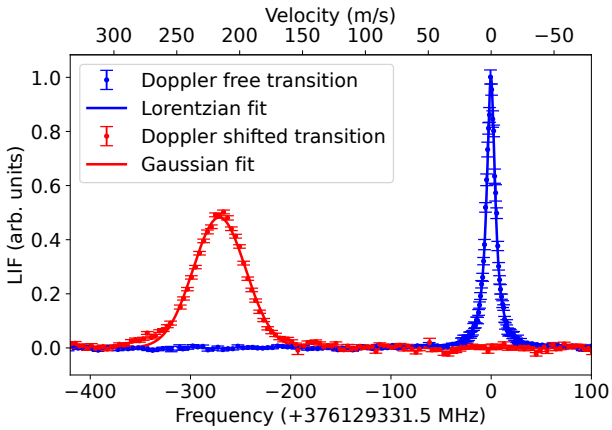

FIGURE 5.5: Doppler free and Doppler shifted spectrum of the $A - D$ transition (vertical axis not to scale). Fluorescence at 413 nm is detected while the frequency of the laser that drives the $A-D$ is scanned and the other laser is locked to the $X-A$ transition frequency. The red data shows the result when the laser beam to drive the $A - D$ transition is counter-propagating with respect to the molecular beam and the laser beam to drive the $X - A$ transition is perpendicular, while the blue data shows the result when both lasers are aligned perpendicularly to the molecular beam. At a certain frequency molecules with a specific longitudinal velocity are Doppler shifted into resonance, as indicated on the top axis. The Doppler-shifted and Doppler-free data are fitted with a Gaussian and a Lorentzian function, respectively.

and deviates by ∼700 MHz from the value found by Effantin *et al.*. Our value for the $X^2\Sigma^+, N = 0, J = 1/2, F = 1 \rightarrow A^2\Pi_{1/2}, J = 1/2, F = 0$ transition is in good agreement with, but two orders in magnitude more accurate than the one found by Steimle *et al.* [34] and Rockenhäuser *et al.* [111]. The $A^2\Pi_{1/2}, J = 1/2, F = 0 \rightarrow D^2\Sigma^+, N = 0, J = 1/2, F = 1$ transition is found by subtracting the second and first entry of Table 5.1.

5.5 Doppler shifted transition frequencies

In this section, we will discuss a measurement of the Doppler profile, by using a laser beam counter-propagating with respect to the molecular beam to drive the $A - D$ transition. First, we ensure that the laser beam that drives the $X - A$ transition is aligned to be perfectly perpendicular to the molecular beam by minimizing the frequency difference between the measurements taken with the laser beam from either side. In our velocity measurements, the frequency difference between left and right was typically ∼300 kHz, corresponding to an error in the measured velocity of ∼0.1 m/s. Furthermore, we ensure that the laser that drives the $A - D$ transition is perfectly counter-propagating with respect to the molecular beam by aligning it onto the orifice

of the source. We estimate the angle between the molecular beam and the laser beam to be below 0.3 degrees. This corresponds to an error in the measured velocity of below 3×10^{-3} m/s. Finally, we fix the frequency of the laser that drives the $X - A$ transition to the value listed in Table 5.1 and scan the frequency of the laser that drives $A - D$ transition, while monitoring the fluorescence yield at 413 nm.

A typical result of such a measurement is shown by the red data points in Figure 5.5. We scan rapidly (within 4 minutes) over the frequency range and average multiple (20 in this case) scans, to average out source fluctuations caused mainly by variation of the barium yield as a function of the rotation of the ablation target. The error bar shown in the figure represents the standard error of the mean of the signal. The spectrum is fitted by a Gaussian function with a mean detuning of (minus) 271 MHz and a full width at half maximum (FWHM) of 61 MHz. From this, we find a mean forward velocity for the molecular beam equal to $\overline{v} = -c(\overline{f} - f_0)/f_0 = 216$ m/s, with f_0 being the $A - D$ Doppler-free resonance, $\overline{f}$ the Doppler shifted resonance frequency and c the speed of light. Similarly, we find that the FWHM velocity spread of the molecular beam is 49 m/s. Note that the velocity distribution is not perfectly described by the Gaussian fit which is indicative for complex dynamics going on in the source discussed in more detail in Section 5.6.

For reference, we also show a spectrum recorded when both lasers are aligned perpendicular to the molecular beam (blue data) corresponding to the Doppler-free transition. This measurement confirms there are no other features in the spectrum that might complicate the interpretation of the velocity measurement.

It is obvious from the measured average velocity that the molecular beam is strongly boosted during the expansion and becomes supersonic – for reference, the mean thermal velocity of BaF molecules and neon atoms at 20 K is 52 m/s and 145 m/s, respectively. This is also obvious from the velocity spread that corresponds to a longitudinal temperature in the moving frame equal to 8 K, significantly below the temperature of the cell.

5.6 Measuring the phase-space distribution of a cryogenic buffer gas cooled beam

Rather than summing the fluorescent signal of the molecules over the pulse duration, such as done in Figure 5.5, we may also plot the velocity as a function of time, as is depicted on the right-hand side of Figure 5.6. As may be expected, there is a correlation between the time the molecules arrive at the detector and their velocity, i.e., faster molecules arrive earlier and slower molecules arrive later. As the velocity and time-of-flight are measured independently of each other, the phase-space distribution can be

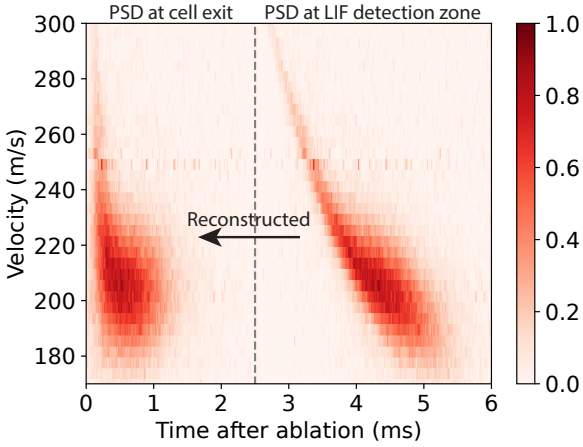

FIGURE 5.6: Phase space distribution (PSD) of the molecular beam at two positions along the molecular beam path. On the right-hand side is plotted, the fluorescence signal of the molecules, recorded by the PMT at a distance of 780 mm from the source. On the left-hand side is plotted, the phase space distribution, reconstructed at the exit of the source. The horizontal line observed at 250 m/s is due to difficulties in determining the frequency of the laser that drives the $A - D$ transition when its beat note with the frequency comb is equal to the repetition rate of the frequency comb.

reconstructed at any position z along the molecular beam path, and most interestingly, at the source exit by using the expression $t(z = 0) = t(z = L_{\mathrm{det}}) - L_{\mathrm{det}}/v$, with L_{det}=780 mm. This reconstructed phase space distribution is shown on the left-hand side of Figure 5.6. As may be observed, the correlations between the arrival time and velocity are much reduced, but are still clearly present. Particularly, it is observed that at the beginning of the pulse, the velocity of the molecules is significantly larger than later in the pulse. This is attributed to the limited heat conduction of the wall of the cell; the temperature of the neon buffer gas is increased by the ablation pulse and it takes typically a few hundred microseconds before this heat is transferred to the cell. In a separate paper [112], we present a detailed discussion of this process and how it is affected by the source parameters. The time-resolution of the recorded phase-space distribution is limited by the time the molecules take to traverse the laser beam that drives the $X - A$ transition and the RC time of the detection system, which add up to $\sim$13 μs. From the sharpest features observed, we deduce an upper limit of the velocity resolution of $\sim$6 m/s, limited by the natural linewidth of the $X - D$ transition or any remaining power broadening. The time-resolution of the reconstructed phase-distribution is dominated by the velocity resolution and is about 120 μs. Note that, we chose to present the phase-space distribution in a time-velocity diagram at a certain position along the molecular beam path as this naturally illustrates the thermodynamics that takes place inside the cell after the ablation pulse is fired. Furthermore, a (more

traditional) diagram of the position velocity distribution of the beam plotted at a specific time would result in some molecules having a position upstream from the source, which is rather unphysical.

As a check of the validity of our method, we have also reconstructed the phase-space distribution at the longitudinal position where the absorption laser crosses the molecular beam. The red curve in Figure 5.2 shows the integrated velocity distribution while the blue curve shows the absorption profile measured simultaneously (averaged over the full duration of the measurements, i.e. over $\sim$10000 shots). The vertical axes have been adjusted such that the amplitudes of the two curves are the same. Although small differences may be observed, the overall agreement is excellent when the neon flow rate is 20 SCCM. The main difference is that sharp features are washed out due to the limited velocity resolution of the fluorescence measurements, causing the non-physical result that BaF signal is observed before the ablation laser is fired. When the neon flow rate is increased, the density in the beam is such that collisions are still taking place after crossing the absorption laser. In this case, the two profiles will be less similar, as is indeed observed in our measurements.

5.7 Conclusions

We have demonstrated a method to determine the longitudinal phase-space distribution of a cryogenic buffer gas cooled beam of barium-fluoride molecules via a two-step laser excitation scheme. Our method allows for a straightforward interpretation, avoiding issues such as optical pumping or an ill-defined interaction region that limit techniques based on one-photon excitation schemes while having a superior resolution compared to techniques based on time of flight measurements. We obtain a temporal and velocity resolution of 11 μs and 6 m/s, respectively, limited by the size of the laser beam driving the $X - A$ transition and the spectral resolution of the $A - D$ transition. This unique resolution allows us to reconstruct the phase space distribution at the exit of the source which reveals the dynamics taking place in the source. Understanding this dynamics is crucial for optimising the intensity of the source at a low forward velocity. In a separate paper[112], we use the two-step laser excitation scheme demonstrated here to study the influence of various source parameters on the velocity distribution of our beam in detail.

6 Influence of source parameters on the longitudinal phase-space distribution of a pulsed cryogenic beam of barium fluoride molecules

6.1 Abstract

Recently, we have demonstrated a method to record the longitudinal phase-space distribution of a pulsed cryogenic buffer gas cooled beam of barium fluoride molecules with high resolution. In this paper, we use this method to determine the influence of various source parameters. Besides the expected dependence on temperature and pressure, the forward velocity of the molecules is strongly correlated with the time they exit the cell, revealing the dynamics of the gas inside the cell. Three observations are particularly noteworthy: (1) The velocity of the barium fluoride molecules increases rapidly as a function of time, reaches a maximum 50-200 μs after the ablation pulse and then decreases exponentially. We attribute this to the buffer gas being heated up by the plume of hot atoms released from the target by the ablation pulse and subsequently being cooled down via conduction to the cell walls. (2) The time constant associated with the exponentially decreasing temperature increases when the source is used for a longer period of time, which we attribute to the formation of a layer of isolating dust on the walls of the cell. By thoroughly cleaning the cell, the time constant is reset to its initial value. (3) The velocity of the molecules at the trailing end of the molecular pulse depends on the length of the cell. For short cells, the velocity is significantly higher than expected from the sudden freeze model. We attribute this to the target remaining warm over the duration of the molecular pulse giving rise to a temperature gradient within the cell. Our observations will help to optimize the source parameters for producing the most intense molecular beam at the target velocity.

This chapter is based on Maarten C. Mooij *et al.* "Influence of source parameters on the longitudinal phase-space distribution of a pulsed cryogenic beam of barium fluoride molecules", 2024 *New J. Phys.* **26** 053009

6.2 Introduction

Molecular radicals offer a number of unique possibilities for precision tests of fundamental physics theories [5, 10, 11] and quantum technology [93, 95, 96, 113]. Traditionally, these molecules are created using ovens [114], resulting in samples at relatively high temperatures which are of limited use for these applications. Rotationally and translationally cold samples of radicals have been produced by entraining laser-ablated species in a supersonic expansion of a carrier gas. In this way bright, $> 10^9$ molecules per steradian per pulse in a single rotational level, and short, < 20 µs, beam pulses have been generated, see for instance [30] and references therein. The mean forward velocity of these beams is determined by the carrier gas and is typically around 600 m/s when using argon and 300 m/s for xenon [35].

A radically different approach for creating intense beams of molecules and molecular radicals is the so-called cryogenic buffer gas beam source, first introduced by Maxwell *et al.* [49] and further developed by Patterson *et al.* [50], van Buuren *et al.* [52], Barry *et al.* [36], Hutzler *et al.* [37, 84] and others. In this method, molecules are introduced into a cold cell by a capillary [49–53], by laser ablation of a target containing a precursor [36–39, 42, 43, 45, 49, 50, 54–60] or by letting laser ablated atoms react with a donor gas [40, 48, 61, 62]. The hot molecules are cooled by collisions with cold helium or neon buffer gas. After many collisions, a fraction of the molecules escapes the cell to form a molecular beam. The dimensions of the cell and the flow rate of the buffer gas determine the pressure within and are chosen in such a way that a significant fraction of the molecules is thermalized before hitting the wall of the cell. It was shown by Patterson *et al.* [50] that by operating the source at a high flow rate, the molecules are more efficiently extracted from the cell, resulting in a more intense molecular beam. At the same time, the higher flow rate leads to a supersonic boost at the exit of the cell, resulting in a faster molecular beam. Typical beam intensities above 10^{11} molecules per sr per pulse in a low rotational state have been reported with forward velocities below 170 m/s [36, 37]. In order to have an efficient extraction while avoiding a supersonic boost to occur, two-stage cryogenic buffer cells have been investigated [45, 50]. Truppe *et al.* [40] introduced a cell design that was optimized for creating relatively short ($\sim$300 µs) but intense molecular beams.

Over the last few years, we have constructed a pulsed cryogenic buffer gas cooled beam source that provides barium monofluoride (BaF) molecules for an experiment that will search for the electron's electric dipole moment (*e*EDM) [12]. In the experiment, the BaF molecules will be decelerated to below 30 m/s using a 4.5 m long travelling-wave Stark decelerator [21]. There is a trade-off between the deceleration strength and the acceptance of the decelerator [19]. In order to decelerate a reasonable fraction of the beam with the current setup, we need a bright beam with an initial velocity

not too far above 200 m/s. Note that, the required length of the decelerator scales with the velocity squared; if the velocity of the initial beam would be 230 m/s instead of 200 m/s, we would need a decelerator with a length of 6 m, to have the same acceptance. Therefore, understanding what determines the velocity of our source and how the source can be optimized for slow beams is of the utmost importance.

Recently we have demonstrated a sensitive method to determine the forward velocity of a buffer gas cooled beam of barium fluoride molecules as a function of time after the ablation pulse, i.e. the longitudinal phase-space distribution of the beam, based on a two-step laser excitation scheme [85]. This method is similar to the one used by Barry *et al.* [105] and Hemmerling *et al.* [106] to study the velocity distribution of laser cooled beams of SrF and CaF, respectively. Here we present a detailed study of the phase-space distribution of a buffer gas cooled beam of barium fluoride as a function of various source parameters. Our paper is organized as follows: in Section 6.3, we introduce our source in detail, followed by an explanation of the so-called sudden freeze model that predicts the dependence of the velocity on the temperature and pressure of the buffer gas, and a recap of our detection method. In Section 6.4, we present measurements of the phase-space distributions while varying source parameters such as the power of the ablation laser, the repetition rate, the temperature of the cell, the flow rate of the SF_6, the operation time, the flow rate of the neon buffer gas and the cell length. Finally, in Section 6.5, we summarize our findings.

6.3 Method

6.3.1 Formation of the molecular beam

Figure 6.1 shows a schematic of our setup including a top-view of our cryogenic buffer gas beam source and the laser beam paths. The design of our cryogenic source is based on that of Truppe *et al.* [40] and Esajas [48]. The heart of our setup is formed by a cubical copper cell kept at a temperature of around 20 K using a 2-stage cryo-cooler (Sumitomo Heavy Industries, cold head RP-082B2S). A continuous flow of pre-cooled neon is passed through the cell with a flow rate of 10-70 standard cubic centimeter per minute (SCCM) [1].

The beam of BaF molecules is formed in four steps: (i) Inside the cell, barium is ablated by a pulsed Nd:YAG laser (532 nm, 5 ns pulse, 10 Hz, typically 8 mJ per pulse measured outside the vacuum) from a rotating solid Ba target. (ii) The barium atoms react with sulphur hexafluoride (SF_6) molecules that are injected into the cell from a copper tube kept at a temperature of 220 K and with a flow rate of typically 0.03 SCCM. (iii) The BaF molecules created in this reaction are cooled via collisions with neon

[1] 1 SCCM = 4.48×10^{17} particles/s

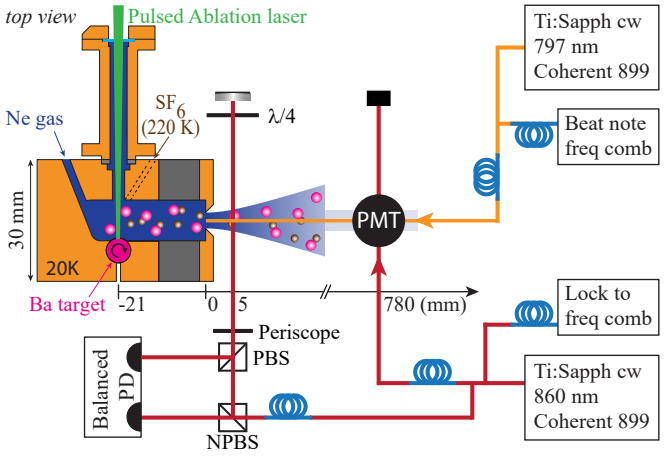

FIGURE 6.1: Schematic view of the experimental setup showing the cryogenic buffer gas beam source and the lasers used for absorption and fluorescence detection. Barium monofluoride molecules are created by letting sulphur hexafluoride molecules react with barium that is ablated from a solid barium rod inside a copper cell that is cooled to 20 K. The molecules cool by collision with neon gas inside the cell, and expand through a 4.5 mm diameter orifice to form a molecular beam. The distance between the target and the exit of the cell can be adjusted by inserting an extension tube between the cell body and the front plate. In the standard cell, the extension tube is absent and the distance between the target and the exit is 11 mm, the figure depicts the situation when a 10 mm long tube is inserted (indicated in gray). The phase-space distribution of the beam is recorded 780 mm after the cell using a two-step laser excitation scheme. Fluorescence back to the ground state is measured using a photomultiplier tube (PMT).

atoms that is continuously flown through the cell with a flow rate of typically 20 SCCM. (iv) They form a molecular beam by expanding through a 4.5 mm diameter orifice into the vacuum. The cell is surrounded by a copper and an aluminium heat shield, at temperatures of 6 K and ∼30 K, respectively. These heat shields also provide the necessary pumping capacity to allow pressures on the order of 10^{-2} mbar inside the cell, while maintaining a pressure below 10^{-6} mbar in the molecular beam chamber. The typical values of the source parameters stated here are the *reference values*, which are used in all measurements presented below, unless a different value is explicitly mentioned.

6.3.2 Beam velocity as a function of pressure and temperature of the carrier gas

In this section, we will summarize some theory required to understand the dependence of the molecular beam velocity on the temperature and pressure of the buffer gas. If the source is operated at a very low buffer gas flow rate (for our cell well below 10 SCCM)

and hence low density, the effusive regime prevails and the molecules leave the exit without colliding with the buffer gas. Consequently, the velocity distribution of the molecules in the beam reflects the temperature inside the cell, corresponding to 52 m/s for BaF molecules and 145 m/s for neon atoms. In practice, we use a much higher flow rate to ensure that the molecules are entrained in the buffer gas and are pumped out of the cell before they have a chance to diffuse to the cell walls. In this so-called hydrodynamic regime many collisions between neon atoms and BaF molecules occur while they leave the cell. As the pressure inside the cell is higher than outside, these collisions lead to a net force that accelerates the neon atoms and barium fluoride molecules along the beam axis and lowers the longitudinal velocity spread of the beam. In this situation, the velocity of the molecules in the beam depends both on the temperature of the cell and the density of the neon gas. To make this statement more quantitative, we summarize here a derivation to relate the temperature, velocity and flow rate, which is based on the derivations of Pauly [83] and Hutzler *et al.* [37].

An isentropic expansion of a high-pressure gas into a vacuum leads to the conversion of internal energy into directed flow energy. In our case, the gas is composed of a mixture of the neon buffer gas, SF_6 and all molecules produced inside the cell, but since the neon accounts for over 99% of the gas, the beam is well described by an expansion of pure neon gas in which the molecules are taken along. When the distance from the source is large compared to the diameter of the exit of the cell, $z \gg d_{\mathrm{exit}}$, the density in the beam, $n(z)$ decreases quadratically with distance:

$$n(z) \approx C \frac{n_0 d_{\mathrm{exit}}^2}{z^2} \tag{6.1}$$

with n_0 the density in the cell and C is a constant that is ∼0.25 for an effusive beam and ∼0.15 for a supersonic beam [83]. The density in the cell is a function of the flow rate, f, the size of the aperture $A = \pi d_{\mathrm{exit}}^2/4$, and the mean velocity of the beam, $\overline{v}$, and is given by [36]:

$$n_0 = \frac{4f}{A\overline{v}}. \tag{6.2}$$

The decrease in density is accompanied by an increase in the most probable velocity, $v_{\mathrm{mp}}(z)$, and a decrease in the temperature, $T(z)$, along the beam. For a mono-atomic gas such as neon, it can be derived that [115]:

$$v_{\mathrm{mp}}(z) = v_\infty \left[1 - \left(\frac{T(z)}{T_0}\right)\right]^{1/2} = v_\infty \left[1 - \left(\frac{n(z)}{n_0}\right)^{2/3}\right]^{1/2}, \tag{6.3}$$

with T_0 being the stagnation temperature of the gas in the cell. If all energy is converted, the temperature of the beam becomes zero, and the forward velocity becomes $v_\infty(T_0) = \sqrt{5k_{\mathrm{B}}T_0/m}$, with m the mass of the buffer gas. In practice, the

conversion process becomes increasingly slower while the density in the beam – and hence the collision rate – becomes smaller with distance from the exit of the cell. Consequently, the most probable velocity of the beam will be smaller than v_∞. In the so-called 'sudden freeze' model [83], it is assumed that the expansion stops abruptly at a certain distance from the source, from which point on the neon atoms and BaF molecules follow ballistic trajectories. The exact position, z_0, of this 'quitting surface' is found by setting Z_2, the integral over the remaining two-body collisions after passing this surface, equal to 1:

$$Z_2 = \int_{z_0/d_{\rm exit}}^{\infty} dZ_2 = 0.0465\sqrt{\frac{8}{\pi}}\overline{\sigma}_{\rm eff} n_0 d_{\rm exit}^{8/3} z_0^{-5/3} = 1, \tag{6.4}$$

with $\sigma_{\rm eff,\ b-b}$ being the effective (temperature averaged) cross-section between buffer gas atoms. The numerical constant in the equation can be found from simulations [83], but its exact value is unimportant for our purpose. Combining the above equations with Equation (6.2) that relates the density in the cell to the flow rate, f, we find:

$$v_{\rm mp}(f, T_0) = v_\infty(T_0)\left[1 - a\left(\frac{f}{v_\infty(T_0)}\right)^{-4/5}\right]^{1/2}, \tag{6.5}$$

with $a = 0.33(\overline{\sigma}_{\rm eff}/d_{\rm exit})^{-4/5}$. This relation can be used to determine the temperature of the gas inside the cell, T_0, from measurements of the mean velocity as a function of the flow rate. [2]

6.3.3 Detection

To monitor the performance of the source, the BaF molecules are detected using absorption directly behind the cell on the $X^2\Sigma^+ \rightarrow A^2\Pi_{1/2}$ transition using ~ 1 μW of light at 860 nm in a 1 mm diameter beam. The absorption signal can be converted into an absolute number by taking into account the spatial and velocity distributions of the beam in the longitudinal and transverse directions, using a procedure that is similar to the one described by Wright *et al.* [44]. At the reference settings the peak absorption is typically 10% (double pass), which corresponds to $1.9(6) \times 10^{10}$ BaF molecules in the $N = 0$ state per pulse and $1.3(5) \times 10^{11}$ molecules per sr per pulse. At a distance of 780 mm from the source, the molecules are excited by light from two Ti:Sapphire lasers (Coherent 899) that are referenced to a frequency comb. One of the lasers is aligned perpendicular to the molecular beam and is resonant with the $X^2\Sigma^+ \rightarrow A^2\Pi_{1/2}$ transition at 860 nm, while the other laser is aligned to be counter-propagating with respect to the molecular beam and resonant with the $A^2\Pi_{1/2} \rightarrow D^2\Sigma^+$ transition around 797 nm. The frequency of this second laser is red-shifted with respect to the

[2] In this derivation, the flow velocity of the neon gas, which is 7-10 m/s in our experiments, is neglected.

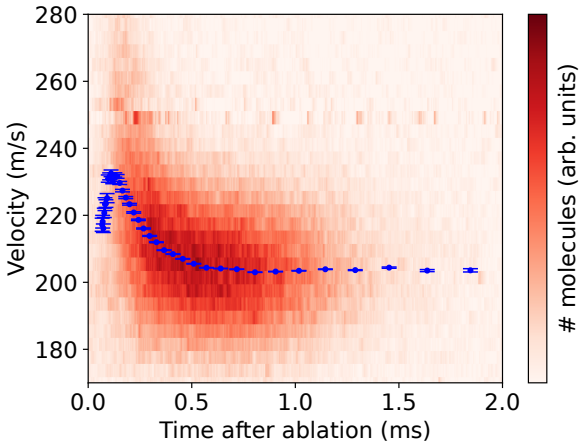

FIGURE 6.2: Phase-space distribution of the molecular beam reconstructed at the exit of the source. The blue data points represent the mean velocities resulting from a Gaussian fit to the data at specific times. The horizontal line observed at 250 m/s is due to difficulties in determining the frequency of the laser that drives the $A - D$ transition when its beat note with the frequency comb is equal to the repetition rate of the frequency comb.

transition frequency to compensate for the Doppler shift. From this detuning, we infer the longitudinal velocity of the molecules. More information on this method can be found in [85].

Once excited to the D-state, part of the molecules will decay back to the ground state by emitting a photon at 413 nm which is efficiently detected using a photomultiplier tube (PMT). A 40 nm wide band-pass filter around 400 nm is used to filter out scattered photons from the laser beams and unwanted fluorescence, resulting in a nearly background-free detection [108].

Figure 6.2 shows a typical measurement of the phase-space distribution reconstructed at the exit of the source [85]. In order to be able to compare phase space distributions taken at different settings, we sum the reconstructed velocity distribution at the exit of the cell over a time interval that increases from 2 μs at the beginning of the pulse to about 250 μs at the end of the pulse and fit these with a Gaussian function. The mean velocity is shown as the blue data points that overlay the measured phase space distribution. The error bars represent the uncertainty from the fit.

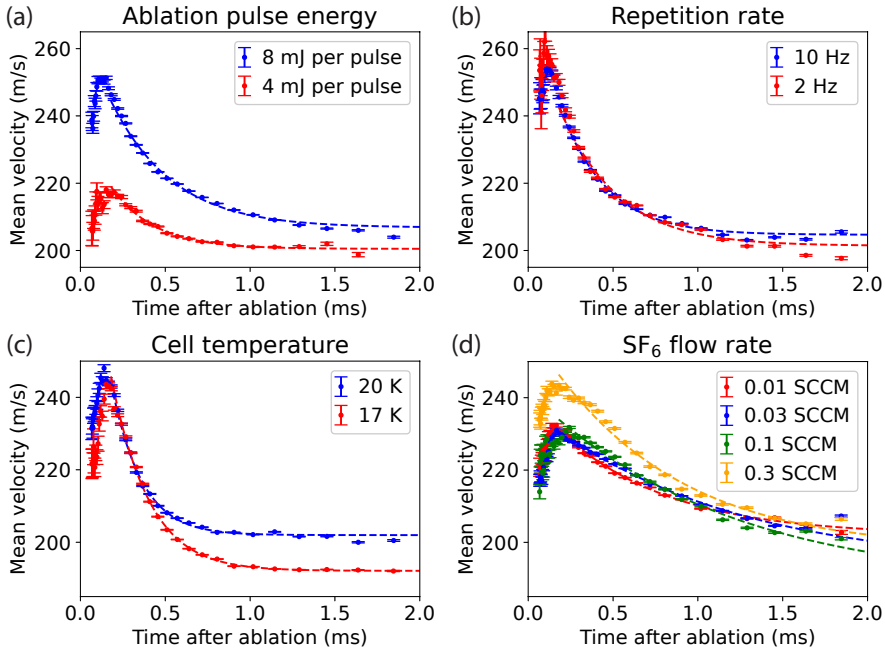

FIGURE 6.3: Mean velocity of the molecular beam as a function of time for different values of (a) the ablation pulse energy, (b) the repetition rate, (c) the cell temperature and (d) the SF_6 flow rate as indicated in the figure. All measurements are taken using a neon buffer gas flow rate of 20 SCCM. The blue data points in all sub-figures are different measurements taken at the reference settings. The dashed lines results from fits using Equation (6.6).

6.4 Characterization of the cryogenic buffer gas beam source

In this section, we will discuss the dependency of the longitudinal phase-space distribution of the molecular beam on various source parameters in order to understand the dynamics within the cell. We will vary these parameters one at a time around the reference values. In Section 6.4.1, we will study the influence of the ablation power, the repetition rate, the temperature of the cell and the flow rate of the SF_6. In Section 6.4.2, we will discuss the influence of the operation time. In Section 6.4.3, we will discuss the influence of the neon flow rate and finally in Section 6.4.4, we will investigate how the phase space distribution of the beam changes when the length of the cell is increased.

6.4.1 Influence of the ablation pulse energy and repetition rate, cell temperature and SF_6 flow rate

Figure 6.3(a) shows the mean velocity of BaF molecules as a function of time after the ablation pulse while using ablation pulse energies of 8 mJ (blue data points) and 4 mJ (red data points). As observed, the velocity first increases and reaches a maximum $\sim$0.1 ms after the ablation pulse and then decreases. At 8 mJ, the velocity increases to above 250 m/s, whereas at 4 mJ, the velocity peaks at about 220 m/s. The number of molecules exiting the source is decreased by about a factor of 3 when the pulse energy is decreased from 8 mJ to 4 mJ.

The fact that the velocity of the molecules is lower in the trailing end of the molecular beam does not seem surprising, given that barium fluoride molecules are produced at very high temperatures [116] and require a minimum number of about 50 collisions [117] before being cooled by the cold neon buffer gas. Naively, we may expect that the molecules that exit the cell shortly after the ablation pulse have had less collisions and are faster than molecules that exit the cell later. This is however *NOT* what we see. Our measurements show that molecules leaving the cell immediately after the ablation pulse have comparable velocities to those at the tail of the pulse, while those that exit the cell 50-200 μs after the ablation pulse, are faster. We deduce from this that, *at any time during the pulse*, the BaF molecules are in thermal equilibrium with the buffer gas. As the mean flow velocity of the buffer gas and BaF molecules are the result of the expansion of the gas inside the cell, the velocity reflects the initial temperature of the buffer gas inside the cell. The observed correlation between the velocity and time reflects the sharp increase in temperature of the buffer gas due to the hot ablation plume and the subsequent decrease in temperature via conduction to the walls and collisions with the cold neon gas that is continuously flown into the cell. This hypothesis is consistent with the $\sim$50 μs thermalisation time expected at the neon densities in our cell and also with earlier observations of Skoff *et al.* [87]. Note that the cell body is not expected to heat up significantly by a single ablation pulse[3], hence we conclude that the limiting factor is the heat conduction of the neon gas to the cell walls. This will be discussed further in Section 6.4.2. It may be observed that even after 1.5 ms the mean velocity measured with an ablation energy of 8 mJ per pulse is still slightly higher than that measured with 4 mJ per pulse. We will come back to this difference in Section 6.4.4.

Figure 6.3(b) shows the mean velocity of BaF molecules as a function of time measured at the same ablation energy of 8 mJ per pulse, but with a repetition rate of 10 Hz (blue data points) or 2 Hz (red data points). As expected, the measured

[3]From the mass of the cell body and the heat capacity of copper at 20 K [118], we estimate that the temperature of the cell body increases by $\sim$5 mK due to a single laser pulse with an energy of 8 mJ.

velocities early in the pulse are very similar, but the velocity in the tail of the molecular pulse drops to a slightly lower velocity, indicating that the temperature of the cell may be slightly lower when operated at 2 Hz instead of 10 Hz.

Figure 6.3(c) shows the mean velocity of BaF molecules as a function of time measured when the copper cell is kept at 20 K (blue data points) or 17 K (red data points). Again, the measured velocities early in the pulse are very similar, but the velocity in the trailing end of the molecular pulse drops to a lower velocity when the cell is kept at a lower temperature. This shows that the source is ideally operated at the lowest possible cell temperature. The minimal temperature is determined by the requirement that the pressure anywhere in the system is above the vapour pressure of neon at that temperature. We observe that at a cell temperature below 20 K, the neon line becomes completely clogged within $\sim$1 hour, which we attribute to a small kink in the neon supply line.

Figure 6.3(d) shows the mean velocity of BaF molecules as a function of time measured when the SF_6 flow rate is varied from 0.01 SCCM to 0.3 SCCM. When the SF_6 flow rate is kept below 0.1 SCCM, the heat introduced by the SF_6 that is injected into the cell through a copper tube kept at a temperature of 220 K, is apparently negligible. Note that the number of barium fluoride molecules produced with these flow rates is similar.

If it is assumed that, after the initial rise, the temperature decreases exponentially, the velocity of the molecular pulse can be fitted to a simple exponential function of the form:

$$v(t) = \sqrt{v_{\mathrm{f}}^2 + (v_{\mathrm{i}}^2 - v_{\mathrm{f}}^2)e^{-t/\tau}}, \tag{6.6}$$

with v_{i} and v_{f} being the initial and final velocities, respectively, and τ a characteristic time constant. These fits are shown as the dashed lines in Figure 6.3. As may be observed, the fitted characteristic time constants between the sets of measurements presented in panels (a)-(d) are rather different, which we blame on the cell being operated for extended times. In the next section, we will study this effect in more detail.

6.4.2 Influence of the operation time

In order to study the effect of the operation time, we thoroughly cleaned the copper cell using acetic acid and subsequently measured the phase space distribution at the same setting for 12 hours distributed over three consecutive days. At the end of each day, the source was heated up to 295 K to remove particles that are frozen to the cell and heat shields. Figure 6.4(a) shows measurements taken after operating the source for 0.5 hour to 10 hours. The dashed lines, also shown in the figure, are fits to the data using Equation (6.6). The inset shows the resulting time constants from these fits

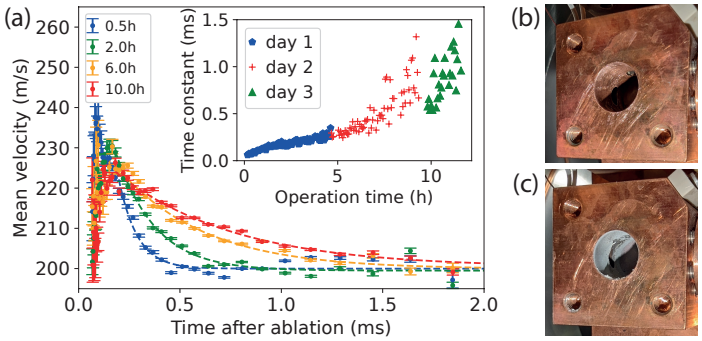

FIGURE 6.4: The effect of operation time. In (a), the mean velocity as a function of time is shown after operating the source for a time period as indicated. When the source is operated for extended times, the exponential decrease of the velocity becomes increasingly slower, resulting in a larger time constant as shown in the inset. (b) and (c) are two pictures of the cell with the front plate removed that are taken before and after measuring the data shown in (a), respectively. It is clear that the cell wall becomes covered with a substantial layer of dust.

as a function of operation time. During the approximately 12 hours of operation, the measured time constant increased from below 100 µs to above 1 ms, which we attribute to barium, barium-sulfides and other reaction products, covering the walls of the cell. This dust decreases the thermal conductivity between the cell and the neon buffer gas. Cleaning the cell resets the source, while simply heating the cell to remove neon and SF_6 ice, has no effect on the measured velocity distribution. Figure 6.4(b) and (c) show photographs of the cell without front aperture, taken before and after measuring the date shown in Figure 6.4(a), respectively, clearly showing the contamination that builds up on the cell wall. The fact that the time constant changes during the operation of the source complicates the systematic study of the source considerably, forcing us to change parameters as quickly as possible while keeping an acceptable signal-to-noise ratio. Similar observations were made by Wright *et al.* [44] in their experiments on AlF. Using NF_3 instead of SF_6 as a fluorine donor, they observed the same yield but with a significantly slower cell degradation. In our experiments on BaF, NF_3 gave a significantly smaller yield and was not studied further.

6.4.3 Influence of the neon flow rate

In this section we will discuss the effect of the neon flow rate. Figure 6.5 shows the reconstructed phase-space distributions at the exit of the cell for buffer gas flow rates between 10 and 70 SCCM (a-g) along with the signal integrated over velocity (h) or time (i). Five trends are observed with higher flow rate: (i) The intensity and (ii) the pulse length of the molecular beam increase, as does the (iii) the characteristic time constant that describes the exponential decrease in temperature in the tail of the

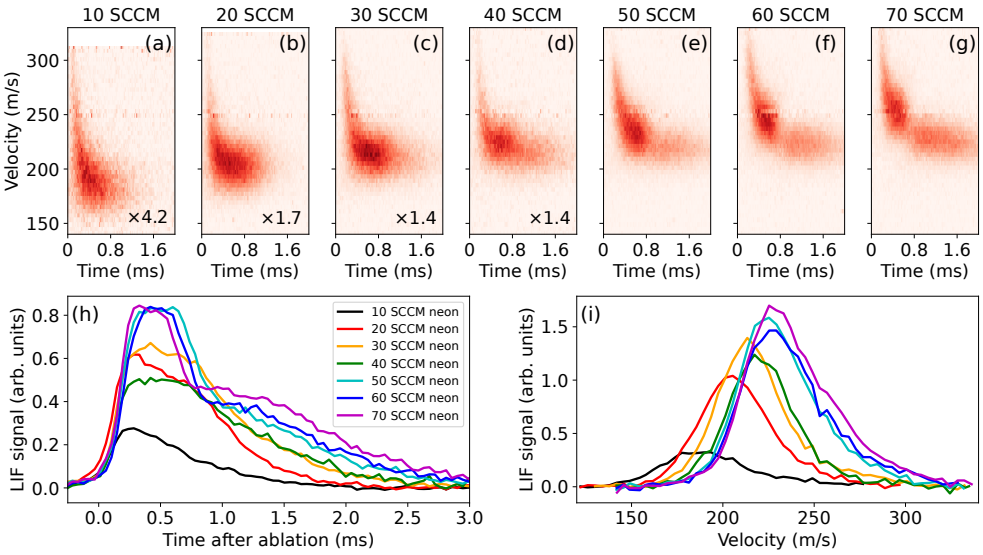

FIGURE 6.5: Phase-space distribution of the cryogenic beam for different neon flow rates. Panels (a-g) show the reconstructed phase-space distribution at the source exit, where $t = 0$ corresponds to the time that the ablation laser is fired. At low neon flow rates, the intensity has been multiplied with a factor as indicated in the panel. Panels (h) and (i) show the reconstructed intensity at different flow rates integrated over velocity and time, respectively. A number of trends are observed with higher flow rate, as described in the main text.

pulse. Furthermore, (iv) the mean velocity of the beam increases, while the (v) velocity spread decreases. The first two effects, which are most obvious from Figure 6.5(h), are attributed to the increased diffusion time at higher neon densities, which reduces the loss of molecules frozen to the cell walls and leads to more efficient extraction from the cell. These effects have been discussed in detail by Patterson and Doyle [50]. The third effect is expected from the fact that the thermal diffusivity of the neon buffer gas decreases with increased density. Finally, the fourth and fifth effects are due to the beam becoming more supersonic when the neon density in the cell is increased and will be analysed in more detail in the remainder of this section. Before doing this, there is one more observation worth noting. At higher flow rates, a dip in intensity is observed in the time of flight curves presented in Figure 6.5(h) around 0.8 ms after the ablation pulse. We do not have a clear explanation for this effect yet [4].

As discussed in Section 6.3.2, the mean velocity and translational temperature of the molecular beam depend on the temperature and pressure of the neon buffer gas inside the cell, which in turn depends on the neon flow rate. The blue data points in Figure 6.6(a) show the final forward velocity, v_{f}, derived from fitting Equation (6.6)

[4] A possible expansion is discussed in Section 4.3 which was written at a later time.

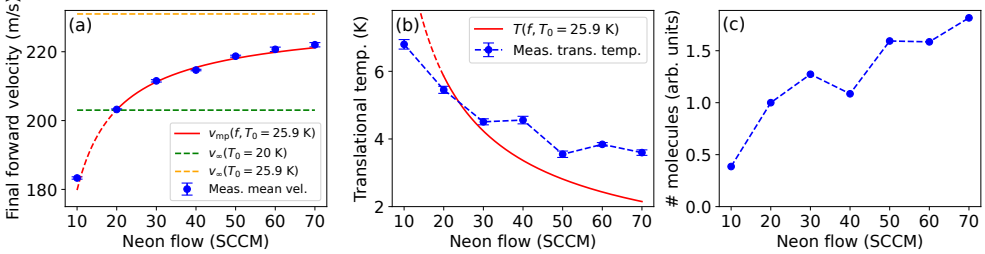

FIGURE 6.6: Velocity (a), temperature (b) and intensity (c) as a function of flow rate. (a) The blue data points show the final velocity, v_f, in the tail of the molecular beam as a function of the neon flow rate. The solid/dashed red line shows a fit of Equation (6.5) to the data for flows between 20 and 70 SCCM from which we determine the terminal velocity v_∞, shown as the dashed orange line, and the temperature of the buffer gas, T_0, which is 25.9 K in this case. For completeness, the green dashed line shows the expected terminal velocity at a cell temperature of 20 K. (b) The blue data points show the measured translational temperature, together with the prediction at 25.9 K. (c) Number of BaF molecules in the $X^2\Sigma^+, v = 0, N = 0, J = 1/2$ ground state.

to the mean velocity, as a function of time for each of the phase-space distributions presented in Figures 6.5(a-g). The error bar of the data displays the uncertainty of this fit. The red solid line is a fit of Equation (6.5) to this data from which we determine T_0 and the terminal velocity $v_\infty(T_0)$, shown as the orange dotted line [5]. In Figure 6.6(b), the blue data points show the corresponding velocity spreads translated into a temperature [6]. The solid red line shows the expected translational temperature from Equation (6.3) at T_0 found from the fit to the data in (a). As may be observed, the model fits the measured mean velocities (and to a lesser extent) the translational temperature well, however, from the fit parameter, $v_\infty(T)$, we find that the buffer gas temperature in the tail of the molecular beam is 25.9 K, significantly above the temperature of the cell of 20 K. This is a somewhat surprising result, given that on these time scales the buffer gas appears to have reached thermal equilibrium with the walls, while from the measurements performed at lower repetition rate, shown in Figure 6.3(b), it is seen that the temperature of the cell returned (close) to its set value within 100 ms. We conclude from this that some part of the cell remains hot during the molecular pulse and only relaxes on a timescale 10-50 ms. We believe that it is in fact the barium target that remains hot. More evidence for this will be presented in the next section.

It would be insightful to determine the temperature of the buffer gas not only at

[5] From this fit we find a collision cross-section $\sigma_{\mathrm{Ne-Ne}} = 1.9 \times 10^{-15}$ cm^2, which is slightly larger than found by a simple hard-sphere model: $\sigma_{\mathrm{hs,Ne-Ne}} = 7.5 \times 10^{-16}$ cm^2 [83].

[6] Note that the rotational temperatures determined in Section 4.7 are more in line with the red curve, suggesting that the translational temperatures are overestimated, partially because the translation velocity spread becomes comparable to the resolution of our method.

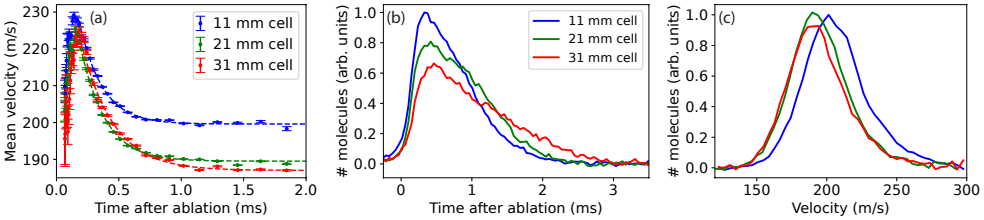

FIGURE 6.7: (a) Mean velocity as a function of time, (b) time-of-flight and (c) velocity distribution for three different target to aperture distances. The velocity in the tail of the molecular pulse is seen to decrease significantly, while the intensity is comparable.

the tail but at any time during the molecular beam pulse. However, this is complicated by the fact that the cooling rate towards the wall depends on the neon density in the cell and hence the flow rate. If we take the velocity measured at a flow rate of 70 SCCM to be the terminal velocity, we find that, at its peak, the temperature of the buffer gas is increased to about 40 K at an ablation pulse energy of 8 mJ/pulse. This is a lower limit for the temperature.

Figure 6.6(c) shows the brightness of the beam of barium fluoride molecules in the $X^2\Sigma^+, v = 0, N = 0, J = 1/2$ ground state as function of the neon flow rate found by integrating the phase-space distributions shown in Figures 6.5a-g. As may be observed, the number of molecules increases by about a factor of 4.7 when the neon flow rate is increased from 10 to 70 SCCM. Note that, the sudden freeze model (presented in Section 6.3.2) predicts that the intensity does not depend strongly on the neon flow rate, as the slight increase of the relative population in the $N = 0$ state due to the lower rotational temperature at high neon flow rates, is compensated by a the increased divergence of the beam [36]. The observed intensity increase at higher flow rate is attributed to the increased efficiency in extraction of the molecules from the cell [50]. The fact that the forward velocity and intensity follow the same trend is a coincident.

6.4.4 Influence of the target to aperture distance

So far, all measurements presented in the paper were performed with the standard cell that has a distance of 11 mm between the ablation target and the source exit. In this section, we will study what happens when the cell is extended to 21 or 31 mm. Figure 6.7(a) presents the mean velocity as a function of time, while (b) and (c) present the intensity integrated over velocity or time, respectively. The ablation power, cell temperature, neon and SF_6 flow rates are set to the reference values. All measurement were taken after the cell was operated for 2 hours. Increasing the target to aperture distance to 21 mm results in a longer molecular pulse that has a significantly lower velocity at the tail of the molecular pulse, while the number of molecules in the beam

is comparable. Extending the cell further reduces the velocity but leads to a drop in the number of molecules by about 10 %. Note that, using Equation (6.5) at 20 K and a neon flow rate of 20 SCCM, the expected mean velocity for molecules exiting our cell is 178 m/s.

We attribute the observed dependence of the velocity on the distance from target to aperture on the occurrence of a heat gradient in the cell. After the ablation pulse, the heat deposited in the ablated barium atoms is transferred to the buffer gas within 100 μs and is subsequently cooled away by the cell within a few ms. On the other hand, the heat deposited in the barium rod is transferred to the buffer gas at a slower rate and the target remains at elevated temperatures during the entire molecular pulse. Increasing the distance between the target and the exit results in the neon gas at the exit being closer to the cell temperature and the molecular beam being slower. This effect also explains the observed dependence of the final velocity on the ablation power, as was discussed in Section 6.4.1.

6.5 Conclusions

We presented measurements of the phase-space distribution of a cryogenic buffer gas beam of BaF. We observe a strong correlation of the mean forward velocity of the BaF molecules at the time they exit the source which is attributed to the neon buffer gas being warmed up by the plume of hot atoms released from the target by the ablation pulse and subsequently being cooled down via conduction to the cell walls. When the cell is operated for a longer period of time, the walls of the cell become covered with a layer of isolating dust which increases the time constant associated with the exponentially decreasing temperature of the neon gas. The barium target remains at elevated temperatures on a much longer time scale, resulting in a higher mean velocity than expected from the sudden freeze model. This velocity can be lowered by extending the length of the cell. Some of the observations above have been reported before, but our new method to accurately measure the phase-space distribution of the beam in combination with the stability and reproducibility of our cell allowed us to analyse these effects in great detail. As optimization of the source amounts to a compromize between brightness and a low forward velocity, a good understanding of the heating processes is pivotal for an optimal choice of the source parameters. In future work, we plan to also study the effect of the size and shape of the cell exit.

Summary and general discussion 7

The purpose of my Ph.D. project was to construct a source for a dense and cold beam of BaF molecules, to analyse the molecular beam produced, and to understand the behaviour of the source to find an optimal working condition, in order to improve the NL-*e*EDM measurement.

After introducing the electric dipole moment of the electron and the design of the NL-*e*EDM experiment in **chapter 1**, the thesis continues in **chapter 2** with a description of the cryogenic source constructed at the Vrije Universiteit. The source is designed to use neon as buffer gas, and BaF molecules are formed in a reaction between laser ablated Ba atoms and the SF_6 gas that is mixed into the buffer gas. A constant ablation yield is achieved by using a reliable system that rotates the target with a stepper motor.

Chapter 3 describes the experimental setup and methods to detect the molecular beam. Using continuous-wave lasers, with wavelengths around 860 nm, the molecular beam is detected by absorption and fluorescence detection 5 and 780 mm behind the cell exit, respectively. Special attention was paid to reliable and accurate frequency calibration using a frequency comb laser, which was crucial for the velocity measurement method described in Chapter 5, and also resulted in daily reproducible and stable measurements. Furthermore, due to the use of a frequency comb, multiple transitions were measured with absolute accuracy, which are listed in Table 4.1 and Table 4.2. The improved accuracy of the measurements allowed us to improve some molecular constants for BaF as found in the literature, see **appendix A**. We note that a full analysis of the molecular constants requires a comprehensive fit, using data from both previous measurements and our measurements, which we leave for future work. Measurements and analysis of the thermodynamic properties of the molecular beam are described in detail in **chapter 4**. Starting with measurements of parameters, such as the transverse velocity and beam size, the chapter concludes with a calculation of the brightness of the beam. In addition, the rotational and vibrational temperature were measured. This required an appropriate selection of transitions and experimental settings to obtain a large set of measurements that included varying the buffer gas flow rate, while keeping the total operation time of the source short to limit the effect of fluctuations of the output of the source. It is found that the collisional dynamics in the beam does not produce a Boltzmann distribution representing a single rotational temperature, while the experimentally determined vibrational temperature is much higher than the rotational one.

During my project, the necessity of a proper velocity detection method became increasingly apparent. Therefore, a setup to retrieve the velocity was built and tested, which is discussed in **chapter 5**. The measurement principle is based on a two-step excitation, where a Doppler-shifted transition frequency is measured between two excited states. The second excitation step allows for a perfect counter-propagating alignment of the laser beam with respect to the molecular beam path, which simplifies analysing the Doppler shift, while avoiding problems of overlap of hyperfine transitions or optical pumping of molecules due to frequency and positional selectivity in the first Doppler-free excitation step.

Besides a velocity distribution, the measurement additionally provided temporal information for the velocity components individually, i.e. a longitudinal phase-space distribution of the molecular beam. Correlations between arrival time and velocity were expected far from the source exit, but more suprisingly, the reconstructed phase-space distribution at the source exit also showed strong correlations. These correlations allowed us to study the dynamics inside the cell. In **chapter 6**, I describe four source parameters that determine the phase-space distribution, namely the energy of the ablation pulse, the operation time of the setup, the flow rate of the neon buffer gas and the distance of the Ba target to the cell aperture.

7.1 Summary of the velocity and brightness of all measured parameters

Throughout this work, I have compared the output of the source with the output when operated at its 'standard' settings; i.e., 8 mJ per pulse ablation power, 10 Hz repetition rate, 2 s rotation period of the target, 20 SCCM neon buffer gas flow rate, 0.03 SCCM SF_6 flow rate, 20 K cell temperature and a 11 mm target to cell aperture distance. Table 7.1 summarises the typical values for the various quantities that describe the molecular beam obtained in the experiments detailed in Chapter 4 and Chapter 6.

Figure 7.1 summarises the effect of changing the source parameters on the brightness and forward velocity of the molecular beam. In each set of measurements, a specific parameter, indicated in the legend, is tuned with respect to its standard setting. Note that measurements taken with the same setting do not always lead to the same result. We attribute this to the effect of the time that the source has been operating, which varies between measurements. For this reason, we focus on relative changes while tuning a single parameter. It is important to highlight that for calculating the brightness, we have performed measurements of the time of flight and the forward velocity at each setting, while the transverse velocity and spatial distributions have been measured at a few settings only and re-used these for the other settings. This is mainly

TABLE 7.1: Summary of the thermal dynamic properties of a typical molecular beam of BaF molecules. See the main text in Chapter 4 and Chapter 6 for more details.

Quantity	Typical value	Unit
$\sigma_{\mathrm{Ne-BaF}}$	5×10^{-15}	cm^2
$v_\perp(z = 5\ \mathrm{mm})$	93	m/s
$v_\perp(z = 14\ \mathrm{mm})$	118	m/s
$v_\parallel$	207	m/s
$\Omega(z = 5\ \mathrm{mm})$	0.15	sr
$\Omega(z = 14\ \mathrm{mm})$	0.24	sr
$d_{\mathrm{beam}}(z = 5\ \mathrm{mm})$	4.4	mm
$T_{\mathrm{rot,abs.}}{}^a$	6.0	K
$T_{\mathrm{rot,LIF}}{}^a$	3.7	K
$T_{\mathrm{vib.}}$	~ 400	K
M	2	optical passes mol. beam
$\sigma_{\mathrm{abs,\ closed\ transition}}$	1.18×10^{-13}	m^2
$\frac{2F_e+1}{2F_g+1}$	1/3	
ξ	6/9	
$\mathcal{FC}_{v(0,0)}$	0.9601 [15]	
σ_{abs}	2.5×10^{-14}	m^2
$\eta_{F=1\to F=0}$	34	%
χ	4/3	
$\Delta t_{\mathrm{BaF}}(\mathrm{FWHM})$	0.9	ms
$\int \ln\left(\frac{1}{1-\eta A(t)}\right) dt$	1.1×10^{-4}	s
$\sqrt{\pi}\sigma_y{}^b$	3.3	mm
$\alpha_{\mathrm{non-res./res.}}$	26	
$n_{N=0,J=1/2}$	6.3×10^9	molecules/cm^3/pulse
$\mathcal{N}_{N=0,J=1/2}$	1.8×10^{10}	molecules/pulse
$\mathcal{B}_{N=0,J=1/2}{}^c$	1.2×10^{11}	molecules/sr/pulse

[a] Determined using the rotational states $J = 0.5$ to $J = 6.5$

[b] Effective vertical molecular beam size to account for molecules outsize laser beam at $y = 0$.

[c] This number is calculated using the measurements at $z = 5$ mm from the source aperture. Due to rotational cooling, the brightness still increases further away from the source, see Figure 4.18.

done to limit the difference in operation time between measurements. The transverse velocity strongly depends on the flow rate of the buffer gas, and the corresponding brightness is corrected for this. We did not investigate the dependency of the transverse spatial distribution on the source parameters but do not expect it to be very sensitive. However, this may lead to an under- or overestimation of the brightness.

I will briefly summarise the main results of all the parameters. **Cell temperature** (blue) Lowering the cell temperature is clearly beneficial due to the reduced velocity, but is limited by the vapour pressure of the buffer gas. **Repetition rate** (light blue) A high repetition rate is beneficial for the time-averaged brightness, and for our setup, a repetition rate of 10 Hz is allowed within the heat load of the cell. **Rotation speed**

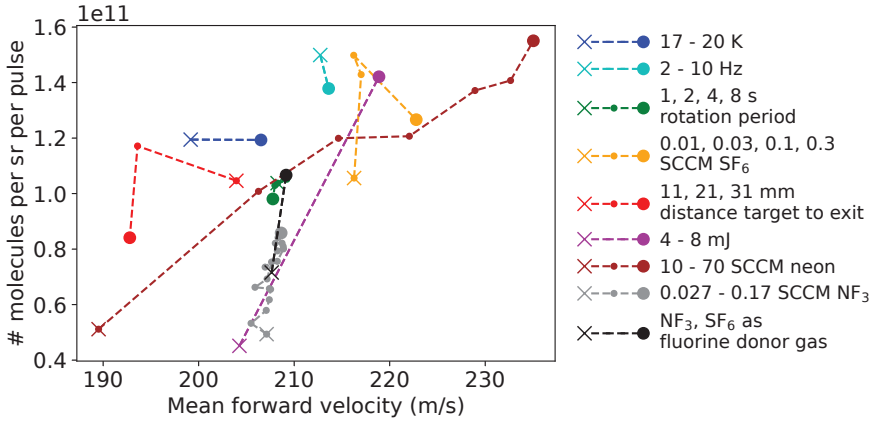

FIGURE 7.1: Brightness and forward velocity of the cryogenic beam. Each set of measurements shows the effect of tuning a single parameter with respect to the standard settings. The × and ● markers correspond to the first and last number of the label text in the legend and (if measured) the • markers correspond to the measured values in between.

source:

of the target (green) No preferred rotation speed of the target was found within the range, and further investigation is not of interest. **SF_6 flow rate** (orange) Optimal settings were found for SF_6 flow rates; a too low SF_6 flow rate limits the reaction to form BaF, while a too high flow rate leads to unnecessary heat load on the cell and potentially accelerates cell contamination. **Cell length** (red) While diffusion loss sets an upper limit of the target to the aperture length, the heat of the Ba target sets a lower limit, which results in an optimal length of 21 mm for our configuration. **Energy of the ablation pulse** (magenta) The optimal setting for the energy of the ablation pulse depends on the desired output. The increase in brightness is coupled with an increase in velocity. For us, the highest measured ablation power seems favourable as the brightness increases more strongly than the velocity, but the number of data points is too small to determine an optimum. **The flow rate of neon buffer gas** (brown) For most applications, the optimal flow rate of the buffer gas is relatively low, i.e. 20 SCCM, as higher flow rates result in a relatively strong increase in velocity with a limited improvement in brightness. Below 20 SCCM, the brightness drops quickly as diffusion losses become a problem. **Fluorine donor** (grey/black) As we have only briefly tested NF_3 (grey) as a fluorine donor gas, we cannot yet draw strong conclusions. The first results showed a strong increase in brightness with increasing NF_3 flow rate, but with the measured flow rate range, brightness remained slightly lower at higher flow rates compared to the use of SF_6 (black).

Within the set of measured parameters, the optimal operation settings for low velocity while preserving the brightness is with 8 mJ per pulse ablation power, 10 Hz

repetition rate, 20 SCCM neon buffer gas flow rate, 0.03 SCCM SF_6 flow rate, 17 K cell temperature and a 21 mm target to cell aperture distance.

Despite testing many, there are still more parameters that I would have liked to have changed. The most notable is the use of helium as buffer gas instead of neon, but this requires a major modification of the setup. Changing the cell diameter and/or cell exit would lead to different flow velocities, and by that, to the neon heat gradient and diffusion loss. Therefore, testing these parameters should be combined with the length of the cell. It has been reported [119] that the shape of the nozzle has a major influence on the divergence of the beam and I would be very interested in trying a de Laval nozzle to achieve a more collimated beam. So far, the study of optimising the ablation yield was limited to changing the energy of the ablation pulse, but the optimum probably depends on the combination of power and intensity on the target.

For efficient extraction from the cell, the buffer gas density needs to be sufficiently high to achieve entrainment of the molecules in the gas. As a consequence of the high buffer gas density, the beam becomes supersonic and the velocity is boosted. Recently, a two-cell design has shown promising results [47]. In this work, the cell was operated in an effusive regime while entrainment in the cell was preserved. An additional benefit is that, in the second part of the cell, contamination of the cell is expected to build up slower, resulting in a more stable velocity distribution.

7.2 Outlook

To perform an *e*EDM measurement, we are interested in the number of molecules passing the interaction zone. Here, I will estimate this number using the numbers provided in Table 7.1 and assuming that the source acts as a point source. In the situation of replacing the supersonic beam source in the 'fast beam' setup, the distance from the source to the detection zone is about 3.8 m [27]. For a beam diameter of 10 mm in the detection zone, the transverse velocity should be less than 0.27 m/s. This corresponds to a solid angle of 1.4×10^{-6} sr and hence about 1.0×10^{6} molecules per pulse in the $N = 0$ state can be detected. This is an order of magnitude higher than estimated for the currently used 'fast beam' setup [28], while the forward velocity from the presently built buffer gas cell is a factor of three lower [30].

The number of molecules in the detection zone for the setup described in Chapter 1 and in more detail in Aggarwal *et al.* [12], depends on many more parameters, of which detailed estimations can be found in Ref [22]. Most importantly, the loss of divergent molecules is reduced by a factor of 2.5 by using an electrostatic lens [23] and can be further reduced by applying transverse laser cooling. In the Stark decelerator, some molecules will be lost, but a better sensitivity of the *e*EDM measurement is expected as a result of an increase in interaction time.

So far, I have only focused on the number of molecules in the $N = 0$ rotational state, because this state will be used for *e*EDM measurement. However, at a rotational temperature of 3.7 K, about 5.5 times more molecules reside in the $N = 1$ or $N = 2$. By applying a pumping scheme demonstrated by Ho *et al.* [25], these molecules could also contribute to the experiment. Note that some optical pumping will be required anyway, as the electrostatic lens and Stark decelerator are only effective for molecules in the $N = 1$ or $N = 2$ state.

In conclusion, we have built an easy-to-use, intense, stable, and reproducible source for BaF molecules that serves as an ideal starting point for the NL-eEDM project [12]. Measurement of the longitudinal phase-space distribution has provided detailed insight into the heating processes within the cryogenic source. The setup is flexible and can be used for other gases, such as BaOH [120] or NH_3. Further investigation of the source parameters, such as the source dimensions and shape of the aperture or second cell, could lead to further optimisation of the molecular beam.

Molecular constants

A

TABLE A.1: Molecular constants used in PGOPHER, *a program for simulating rotational, vibrational and electronic Spectra* [75]. Constants are taken from Refs. [34, 107, 110, 121, 122], except for the state origin of the $A^2\Pi(v=0)$ and $D^2\Sigma^+(v=0)$ manifolds and the spin-orbit coupling constant A in the $A^2\Pi(v=0)$ manifold, which are fitted (with all other constants fixed) using PGOPHER on the transitions listed in Table 4.2 and Table 5.1, which are highly accurate due to the use of an optical frequency comb. With these constants, all measured lines of Table 4.1 agreed to within 1.7 MHz with the calculated values. The magnetic hyperfine constants are described in terms of the Frosch and Foley parameters [123].

Molecular constant	Symbol	Value (cm^{-1})	Value (MHz)
$X^2\Sigma^+(v=0)$			
Rotational constant	B	0.21594802	6473.9588^a
Spin rotation coupling constant	γ	$0.0027004(6)$	$80.955(19)^a$
Quartic centrifugal distortion	D	$1.84294(18)\times10^{-7\ b}$	$0.0055250(5)$
Sextic centrifugal distortion	H	$1.40(39)\times10^{-14\ b}$	$4.2(1.2)\times10^{-10}$
Centrifugal distortion of γ	γ_D	$-1.95(24)\times10^{-6}$	$-0.0584(73)^a$
J^6 Centrifugal distortion of γ	γ_H	$3.7(6)\times10^{-9}$	$0.000112(17)^a$
Magnetic hyperfine parameter	b	$0.0021184(11)$	$63.509(32)^f$
Magnetic hyperfine parameter	c	$0.0002743(19)$	$8.224(58)^f$
$A^2\Pi(v=0)$			
State origin		11946.10960	358135355.9^c
Rotational constant	B	$0.2117414(10)^d$	$6347.847(30)$
Spin-orbit coupling constant	A	632.28781	18955511.5^c
Λ-doubling constant	p	$-0.257310(17)^b$	$-7713.96(51)$
Λ-doubling constant	q	$-8.40(29)\times10^{-5\ b}$	$-2.52(9)$
Centrifugal distortion of p	p_D	$-2.332(24)\times10^{-7\ b}$	$-0.00699(7)$
Centrifugal distortion of A	A_D	$3.1(2)\times10^{-5\ d}$	$0.93(6)$
Magnetic hyperfine parameter	a	$0.0008856(33)$	$26.55(10)^f$
Magnetic hyperfine parameter	$b+c$	$0.000185(6)$	$-5.54(19)^f$
Magnetic hyperfine parameter	d	$0.000119(5)$	$3.58(14)^f$
$D^2\Sigma^+(v=0)$			
State origin		24176.58387	724795750.4^c
Rotational constant	B	$0.2274137(22)^b$	$6817.69(7)$
Spin rotation coupling constant	γ	$0.007130(25)^b$	$213.8(7)$

[a] Ryzlewicz *et al.* [121]

[b] Effantin *et al.* [110]

[c] this work

[d] Steimle *et al.* [34]

[e] Bernard *et al.* [122]

[f] Ernst *et al.* [107]

A

Bibliography

[1] Particle Data Group, P. A. Zyla, and *et al.* Review of Particle Physics. *Progress of Theoretical and Experimental Physics*, **2020**(8), 083C01, 2020.

[2] M. Dine and A. Kusenko. Origin of the matter-antimatter asymmetry. *Reviews of Modern Physics*, **76**(1), 1–30, 2003.

[3] J. H. Christenson, J. W. Cronin, V. L. Fitch, and R. Turlay. Evidence for the 2π Decay of the ${K_2}^0$ Meson. *Physical Review Letters*, **13**(4), 138–140, 1964.

[4] Y. Ema, T. Gao, and M. Pospelov. Standard Model Prediction for Paramagnetic Electric Dipole Moments. *Physical Review Letters*, **129**(23), 231801, 2022.

[5] M. S. Safronova, D. Budker, D. DeMille, D. F. Kimball, A. Derevianko, and C. W. Clark. Search for new physics with atoms and molecules. *Reviews of Modern Physics*, **90**(2), 25008, 2018.

[6] E. A. Hinds. Testing time reversal symmetry using molecules. *Physica Scripta T*, **70**, 34–41, 1997.

[7] J. J. Hudson, B. E. Sauer, M. R. Tarbutt, and E. A. Hinds. Measurement of the electron electric dipole moment using YbF molecules. *Physical Review Letters*, **89**(2), 230031–230034, 2002.

[8] J. J. Hudson, D. M. Kara, I. J. Smallman, B. E. Sauer, M. R. Tarbutt, and E. A. Hinds. Improved measurement of the shape of the electron. *Nature*, **473**(7348), 493–496, 2011.

[9] The ACME Collaboration, J. Baron, W. C. Campbell, D. DeMille, J. M. Doyle, G. Gabrielse, Y. V. Gurevich, P. W. Hess, N. R. Hutzler, E. Kirilov, I. Kozyryev, B. R. O'Leary, C. D. Panda, M. F. Parsons, E. S. Petrik, B. Spaun, A. C. Vutha, and A. D. West. Order of Magnitude Smaller Limit on the Electric Dipole Moment of the Electron. *Science*, **343**(6168), 269–272, 2014.

[10] V. Andreev, D. G. Ang, D. DeMille, J. M. Doyle, G. Gabrielse, J. Haefner, N. R. Hutzler, Z. Lasner, C. Meisenhelder, B. R. O'Leary, C. D. Panda, A. D. West, E. P. West, and X. Wu. Improved limit on the electric dipole moment of the electron. *Nature*, **562**(7727), 355–360, 2018.

[11] T. S. Roussy, L. Caldwell, T. Wright, W. B. Cairncross, Y. Shagam, K. B. Ng, N. Schlossberger, S. Y. Park, A. Wang, J. Ye, and E. A. Cornell. An improved bound on the electron's electric dipole moment. *Science*, **381**(6653), 46–50, 2023.

[12] P. Aggarwal, H. L. Bethlem, A. Borschevsky, M. Denis, K. Esajas, P. A. Haase, Y. Hao, S. Hoekstra, K. Jungmann, T. B. Meijknecht, M. C. Mooij, R. G. E. Timmermans, W. Ubachs, L. Willmann, and A. Zapara. Measuring the electric dipole moment of the electron in BaF. *European Physical Journal D*, **72**(11), 197, 2018.

[13] P. A. Haase, D. J. Doeglas, A. Boeschoten, E. Eliav, M. Iliaš, P. Aggarwal, H. L. Bethlem, A. Borschevsky, K. Esajas, Y. Hao, S. Hoekstra, V. R. Marshall, T. B. Meijknecht, M. C. Mooij, K. Steinebach, R. G. E. Timmermans, A. P. Touwen, W. Ubachs, L. Willmann, and Y. Yin. Systematic study and uncertainty evaluation of P,T-odd molecular enhancement factors in BaF. *The Journal of Chemical Physics*, **155**(3), 034309, 2021.

[14] M. Abe, G. Gopakumar, M. Hada, B. P. Das, H. Tatewaki, and D. Mukherjee. Application of relativistic coupled-cluster theory to the effective electric field in YbF. *Physical Review A*, **90**(2), 022501, 2014.

[15] Y. Hao, L. F. Pašteka, L. Visscher, P. Aggarwal, H. L. Bethlem, A. Boeschoten, A. Borschevsky, M. Denis, K. Esajas, S. Hoekstra, K. Jungmann, V. R. Marshall, T. B. Meijknecht, M. C. Mooij, R. G. E. Timmermans, A. Touwen, W. Ubachs, L. Willmann, Y. Yin, and A. Zapara. High accuracy theoretical investigations of CaF, SrF, and BaF and implications for laser-cooling. *The Journal of Chemical Physics*, **151**(3), 34302, 2019.

[16] Y. Zhang, Z. Zeng, Q. Liang, W. Bu, and B. Yan. Doppler cooling of buffer-gas-cooled barium monofluoride molecules. *Physical Review A*, **105**(3), 033307, 2022.

[17] M. Rockenhäuser, F. Kogel, T. Garg, S. A. Morales-Ramírez, and T. Langen. Laser cooling of barium monofluoride molecules using synthesized optical spectra. *Physical Review Research*, **6**, 043161, 2024.

[18] H. L. Bethlem, G. Berden, and G. Meijer. Decelerating Neutral Dipolar Molecules. *Physical Review Letters*, **83**(8), 1558–1561, 1999.

[19] S. Y. T. van de Meerakker, H. L. Bethlem, N. Vanhaecke, and G. Meijer. Manipulation and control of molecular beams. *Chemical Reviews*, **112**(9), 4828–4878, 2012.

[20] A. Zapara. *Dynamics of Molecular Beams in a Traveling-Wave Stark Decelerator*. PhD thesis, University of Groningen, 2019.

[21] P. Aggarwal, Y. Yin, K. Esajas, H. L. Bethlem, A. Boeschoten, A. Borschevsky, S. Hoekstra, K. Jungmann, V. R. Marshall, T. B. Meijknecht, M. C. Mooij, R. G. E. Timmermans, A. Touwen, W. Ubachs, and L. Willmann. Deceleration and Trapping of SrF Molecules. *Physical Review Letters*, **127**(17), 173201, 2021.

[22] A. Touwen. *Readout and Control of Molecules for Electric Dipole Moment Searches:*. PhD thesis, University of Groningen, 2024.

[23] A. Touwen, J. W. F. van Hofslot, T. Qualm, R. Borchers, R. Bause, H. L. Bethlem, A. Boeschoten, A. Borschevsky, T. H. Fikkers, S. Hoekstra, K. Jungmann, V. R. Marshall, T. B. Meijknecht, M. C. Mooij, R. G. E. Timmermans, W. Ubachs, L. Willmann, and NL-*e*EDM collaboration. Manipulating a beam of barium fluoride molecules using an electrostatic hexapole. *New Journal of Physics*, **26**(7), 073054, 2024.

[24] T. Chen, W. Bu, and B. Yan. Radiative deflection of a BaF molecular beam via optical cycling. *Physical Review A*, **96**(5), 053401, 2017.

[25] C. J. Ho, J. A. Devlin, I. M. Rabey, P. Yzombard, J. Lim, S. C. Wright, N. J. Fitch, E. A. Hinds, M. R. Tarbutt, and B. E. Sauer. New techniques for a measurement of the electron's electric dipole moment. *New Journal of Physics*, **22**(5), 053031, 2020.

[26] A. Boeschoten, V. R. Marshall, T. B. Meijknecht, A. Touwen, H. L. Bethlem, A. Borschevsky, S. Hoekstra, J. W. F. van Hofslot, K. Jungmann, M. C. Mooij, R. G. E. Timmermans, W. Ubachs, and L. Willmann. Spin-precession method for sensitive electric dipole moment searches. *Physical Review A*, **110**(1), L010801, 2024.

[27] T. Meijknecht. *Electric and Magnetic Field Control for Electric Dipole Moment Searches:*. PhD thesis, University of Groningen, 2023.

[28] A. Boeschoten. *Precision Measurements in Diatomic Molecules: A Route to a Permanent Electric Dipole Moment:*. PhD thesis, University of Groningen, 2023.

[29] V. R. Marshall. *Spectroscopy and Systematic Effects: An eEDM Experiment Using BaF Molecules:*. PhD thesis, University of Groningen, 2024.

[30] P. Aggarwal, H. L. Bethlem, A. Boeschoten, A. Borschevsky, K. Esajas, Y. Hao, S. Hoekstra, K. Jungmann, V. R. Marshall, T. B. Meijknecht, M. C. Mooij, R. G. E. Timmermans, A. Touwen, W. Ubachs, L. Willmann, Y. Yin, and A. Zapara. A

supersonic laser ablation beam source with narrow velocity spreads. *Review of Scientific Instruments*, **92**(3), 33202, 2021.

[31] P. Haase. *Electronic Structure Theory Meets Precision Measurements:*. PhD thesis, University of Groningen, 2021.

[32] M. Denis, P. A. B. Haase, M. C. Mooij, Y. Chamorro, P. Aggarwal, H. L. Bethlem, A. Boeschoten, A. Borschevsky, K. Esajas, Y. Hao, S. Hoekstra, J. W. F. van Hofslot, V. R. Marshall, T. B. Meijknecht, R. G. E. Timmermans, A. Touwen, W. Ubachs, L. Willmann, and Y. Yin. Benchmarking of the Fock-space coupled-cluster method and uncertainty estimation: Magnetic hyperfine interaction in the excited state of BaF. *Physical Review A,* **105**(5), 52811, 2022.

[33] D. Rahmlow. *Towards a Measurement of Parity Nonconservation in Diatomic Molecules*. PhD thesis, Yale University, 2008.

[34] T. C. Steimle, S. Frey, A. Le, D. DeMille, D. A. Rahmlow, and C. Linton. Molecular-beam optical Stark and Zeeman study of the $A^2\Pi$ - $X^2\Sigma^+$ (0,0) band system of BaF. *Physical Review A*, **84**(1), 012508, 2011.

[35] M. R. Tarbutt, J. J. Hudson, B. E. Sauer, E. A. Hinds, V. A. Ryzhov, V. L. Ryabov, and V. F. Ezhov. A jet beam source of cold YbF radicals. *Journal of Physics B: Atomic, Molecular and Optical Physics*, **35**(24), 5013–5022, 2002.

[36] J. F. Barry, E. S. Shuman, and D. DeMille. A bright, slow cryogenic molecular beam source for free radicals. *Physical Chemistry Chemical Physics*, **13**(42), 18936–18947, 2011.

[37] N. R. Hutzler, M. F. Parsons, Y. V. Gurevich, P. W. Hess, E. Petrik, B. Spaun, A. C. Vutha, D. DeMille, G. Gabrielse, and J. M. Doyle. A cryogenic beam of refractory, chemically reactive molecules with expansion cooling. *Physical Chemistry Chemical Physics*, **13**(42), 18976–18985, 2011.

[38] G. Z. Iwata, R. L. McNally, and T. Zelevinsky. High-resolution optical spectroscopy with a buffer-gas-cooled beam of BaH molecules. *Physical Review A*, **96**(2), 22509, 2017.

[39] I. Kozyryev, L. Baum, K. Matsuda, B. L. Augenbraun, L. Anderegg, A. P. Sedlack, and J. M. Doyle. Sisyphus Laser Cooling of a Polyatomic Molecule. *Physical Review Letters*, **118**(17), 173201, 2017.

[40] S. Truppe, M. Hambach, S. M. Skoff, N. E. Bulleid, J. S. Bumby, R. J. Hendricks, E. A. Hinds, B. E. Sauer, and M. R. Tarbutt. A buffer gas beam source for short,

intense and slow molecular pulses. *Journal of Modern Optics*, **65**(5-6), 648–656, 2018.

[41] J. Lim, J. R. Almond, M. A. Trigatzis, J. A. Devlin, N. J. Fitch, B. E. Sauer, M. R. Tarbutt, and E. A. Hinds. Laser Cooled YbF Molecules for Measuring the Electron's Electric Dipole Moment. *Physical Review Letters*, **120**(12), 123201, 2018.

[42] R. Albrecht, M. Scharwaechter, T. Sixt, L. Hofer, and T. Langen. Buffer-gas cooling, high-resolution spectroscopy, and optical cycling of barium monofluoride molecules. *Physical Review A*, **101**(1), 013413, 2020.

[43] J. C. Shaw and D. J. McCarron. Bright, continuous beams of cold free radicals. *Physical Review A*, **102**(4), 41302, 2020.

[44] S. C. Wright, M. Doppelbauer, S. Hofsäss, H. Christian Schewe, B. Sartakov, G. Meijer, and S. Truppe. Cryogenic buffer gas beams of AlF, CaF, MgF, YbF, Al, Ca, Yb and NO – a comparison. *Molecular Physics*, **121**, e2146541, 2022.

[45] H. I. Lu, J. Rasmussen, M. J. Wright, D. Patterson, and J. M. Doyle. A cold and slow molecular beam. *Physical Chemistry Chemical Physics*, **13**(42), 18986–18990, 2011.

[46] J. Bumby. *Progress towards a Source of Cold, Slow Molecules for Tests of Fundamental Physics*. PhD thesis, Imperial College London, 2017.

[47] A. D. White, S. Popa, J. Mellado-Muñoz, N. J. Fitch, B. E. Sauer, J. Lim, and M. R. Tarbutt. Slow molecular beams from a cryogenic buffer gas source. *Physical Review Research*, **6**(4), 043232, 2024.

[48] K. Esajas. *Intense Slow Beams of Heavy Molecules to Test Fundamental Symmetries*. PhD thesis, University of Groningen, 2021.

[49] S. E. Maxwell, N. Brahms, R. deCarvalho, D. R. Glenn, J. S. Helton, S. V. Nguyen, D. Patterson, J. Petricka, D. DeMille, and J. M. Doyle. High-flux beam source for cold, slow atoms or molecules. *Physical Review Letters*, **95**(17), 173201, 2005.

[50] D. Patterson and J. M. Doyle. Bright, guided molecular beam with hydrodynamic enhancement. *The Journal of Chemical Physics*, **126**(15), 154307, 2007.

[51] D. Patterson, J. Rasmussen, and J. M. Doyle. Intense atomic and molecular beams via neon buffer-gas cooling. *New Journal of Physics*, **11**(12pp), 55018, 2009.

[52] L. D. van Buuren, C. Sommer, M. Motsch, S. Pohle, M. Schenk, J. Bayerl, P. W. Pinkse, and G. Rempe. Electrostatic extraction of cold molecules from a cryogenic reservoir. *Physical Review Letters*, **102**(3), 33001, 2009.

[53] V. Singh, A. K. Samanta, N. Roth, D. Gusa, T. Ossenbrüggen, I. Rubinsky, D. A. Horke, and J. Küpper. Optimized cell geometry for buffer-gas-cooled molecular-beam sources. *Physical Review A*, **97**(3), 32704, 2018.

[54] N. E. Bulleid, S. M. Skoff, R. J. Hendricks, B. E. Sauer, E. A. Hinds, and M. R. Tarbutt. Characterization of a cryogenic beam source for atoms and molecules. *Physical Chemistry Chemical Physics*, **15**(29), 12299–12307, 2013.

[55] M. T. Hummon, M. Yeo, B. K. Stuhl, A. L. Collopy, Y. Xia, and J. Ye. 2D Magneto-Optical Trapping of Diatomic Molecules. *Physical Review Letters*, **110**(14), 143001, 2013.

[56] Y. Zhou, D. D. Grimes, T. J. Barnum, D. Patterson, S. L. Coy, E. Klein, J. S. Muenter, and R. W. Field. Direct detection of Rydberg–Rydberg millimeter-wave transitions in a buffer gas cooled molecular beam. *Chemical Physics Letters*, **640**, 124–136, 2015.

[57] L. Santamaria, V. D. Sarno, P. D. Natale, M. D. Rosa, M. Inguscio, S. Mosca, I. Ricciardi, D. Calonico, F. Levi, and P. Maddaloni. Comb-assisted cavity ring-down spectroscopy of a buffer-gas-cooled molecular beam. *Physical Chemistry Chemical Physics*, **18**(25), 16715–16720, 2016.

[58] X. Li, L. Xu, Y. Yin, S. Xu, Y. Xia, and J. Yin. Rotational relaxation of fluoromethane molecules in low-temperature collisions with buffer-gas helium. *Physical Review A*, **93**(6), 063407, 2016.

[59] C. J. E. Straatsma, M. I. Fabrikant, G. E. Douberly, and H. J. Lewandowski. Production of carbon clusters C_3 to C_{12} with a cryogenic buffer-gas beam source. *The Journal of Chemical Physics*, **147**(12), 124201, 2017.

[60] W. Bu, T. Chen, G. Lv, and B. Yan. Cold collision and high-resolution spectroscopy of buffer-gas-cooled BaF molecules. *Physical Review A*, **95**(3), 32701, 2017.

[61] S. Xu, M. Xia, R. Gu, C. Pei, Z. Yang, Y. Xia, and J. Yin. Cold collision and the determination of the $X^2\Sigma_{1/2}(v = 1, N = 1) \rightarrow A^2\Pi_{1/2}(v' = 0, J' = 1/2)$ frequency with buffer-gas-cooled MgF molecules. *Journal of Quantitative Spectroscopy and Radiative Transfer*, **236**, 106583, 2019.

[62] S. Hofsäss, M. Doppelbauer, S. C. Wright, S. Kray, B. G. Sartakov, J. Pérez-Ríos, G. Meijer, and S. Truppe. Optical cycling of AlF molecules. *New Journal of Physics*, **23**(7), 075001, 2021.

[63] W. M. Haynes, editor. *CRC Handbook of Chemistry and Physics*. CRC Press, Boca Raton, 97 edition, 2016.

[64] A. G. Tobin, D. W. Sedgley, T. H. Batzer, and W. R. Call. Evaluation of charcoal sorbents for helium cryopumping in fusion reactors. *Journal of Vacuum Science & Technology A*, **5**(1), 101–105, 1987.

[65] Informatics, NIST Office of Data. *NIST Chemistry WebBook*. National Institute of Standards and Technology, 2023.

[66] Cryogenic material properties 304 Stainless | National Institute of Standards and Technology.

[67] Neon | Gas Encyclopedia Air Liquide.

[68] Cryogenic material properties 1100 Aluminum | National Institute of Standards and Technology.

[69] R. L. Brown and S. E. Stein. Boiling point data. In *NIST Chemistry WebBook, NIST Standard Reference Database Number 69*. National Institute of Standards and Technology, 2024.

[70] D. L. Rule and L. L. Sparks. Low-temperature thermal conductivity of composites: Alumina fiberepoxy and alumina fiberPEEK. Technical Report NIST IR 89-3914, National Institute of Standards and Technology, Gaithersburg, MD, 1989.

[71] W. Menzel and F. Mohry. Die Dampfdrucke des CF_4 und NF_3 und der Tripelpunkt des CF_4. *Zeitschrift für anorganische und allgemeine Chemie*, **210**(3), 257–263, 1933.

[72] C.-M. Meng. *Femtosecond Laser Detection of Xenon and Stark Decelerated Polyatomic Molecules*. PhD thesis, Vrije Universiteit Amsterdam, 2015.

[73] M. R. Tarbutt. Laser cooling of molecules. *Contemporary Physics*, **59**(4), 356–376, 2018.

[74] P. Aggarwal, V. R. Marshall, H. L. Bethlem, A. Boeschoten, A. Borschevsky, M. Denis, K. Esajas, Y. Hao, S. Hoekstra, K. Jungmann, T. B. Meijknecht, M. C. Mooij, R. G. E. Timmermans, A. Touwen, W. Ubachs, S. M. Vermeulen, L. Willmann, Y. Yin, and A. Zapara. Lifetime measurements of the $A^2\Pi_{1/2}$ and $A^2\Pi_{3/2}$ states in BaF. *Physical Review A*, **100**(5), 52503, 2019.

[75] C. M. Western. PGOPHER: A program for simulating rotational, vibrational and electronic spectra. *Journal of Quantitative Spectroscopy and Radiative Transfer*, **186**, 221–242, 2017.

[76] J. M. Brown and A. Carrington. *Rotational Spectroscopy of Diatomic Molecules*. Cambridge University Press, 2003.

[77] P. Hofland. Towards absorption spectroscopy on a buffer gas cooled beam of BaF molecules In search of the electric dipole moment of the electron. Master's thesis, Vrije Universiteit Amsterdam, 2019.

[78] G. Kirchmair. Frequency stabilization of a Titanium-Sapphire laser for precision spectroscopy on Calcium ions. Master's thesis, Leopold Franzens University of Innsbruck, 2006.

[79] T. W. Hänsch. Nobel lecture: Passion for precision. *Reviews of Modern Physics*, **78**(4), 1297–1309, 2006.

[80] N. Picqué and T. W. Hänsch. Frequency comb spectroscopy. *Nature Photonics*, **13**(3), 146–157, 2019.

[81] L.-S. Ma, M. Zucco, S. Picard, L. Robertsson, and R. Windeler. A new method to determine the absolute mode number of a mode-locked femtosecond-laser comb used for absolute optical frequency measurements. *IEEE Journal of Selected Topics in Quantum Electronics*, **9**(4), 1066–1071, 2003.

[82] S. Witte, R. T. Zinkstok, W. Ubachs, W. Hogervorst, and K. S. E. Eikema. Deep-Ultraviolet Quantum Interference Metrology with Ultrashort Laser Pulses. *Science*, **307**(5708), 400–403, 2005.

[83] H. Pauly. *Atom, Molecule, and Cluster Beams I*, volume 28. Springer Berlin Heidelberg, Berlin, Heidelberg, 2000.

[84] N. R. Hutzler, H. I. Lu, and J. M. Doyle. The buffer gas beam: An intense, cold, and slow source for atoms and molecules. *Chemical Reviews*, **112**(9), 4803–4827, 2012.

[85] M. C. Mooij, H. L. Bethlem, A. Boeschoten, A. Borschevsky, T. H. Fikkers, S. Hoekstra, J. W. F. van Hofslot, K. Jungmann, V. R. Marshall, T. B. Meijknecht, R. G. E. Timmermans, A. Touwen, W. Ubachs, and L. Willmann. A method to determine the phase-space distribution of a pulsed molecular beam. *Journal of Physics B: Atomic, Molecular and Optical Physics*, **58**(1), 015303, 2025.

[86] I. Kozyryev, L. Baum, K. Matsuda, P. Olson, B. Hemmerling, and J. M. Doyle. Collisional relaxation of vibrational states of SrOH with He at 2 K. *New Journal of Physics*, **17**(4), 045003, 2015.

[87] S. M. Skoff, R. J. Hendricks, C. D. J. Sinclair, J. J. Hudson, D. M. Segal, B. E. Sauer, E. A. Hinds, and M. R. Tarbutt. Diffusion, thermalization, and optical pumping of YbF molecules in a cold buffer-gas cell. *Physical Review A*, **83**(2), 23418, 2011.

[88] D. Budker, D. F. Kimball, and D. P. DeMille. *Atomic Physics: An Exploration Through Problems and Solutions*. Oxford University Press, USA, 2008.

[89] R. C. Hilborn. Einstein coefficients, cross sections, f values, dipole moments, and all that. *American Journal of Physics*, **50**(11), 982–986, 1982.

[90] R. C. Hilborn. Einstein coefficients, cross sections, f values, dipole moments, and all that. *arXiv*, (arXiv:physics/0202029), 2002.

[91] T. E. Wall, J. F. Kanem, J. J. Hudson, B. E. Sauer, D. Cho, M. G. Boshier, E. A. Hinds, and M. R. Tarbutt. Lifetime of the A ($v' = 0$) state and Franck-Condon factor of the A-X (0-0) transition of CaF measured by the saturation of laser-induced fluorescence. *Physical Review A*, **78**(6), 62509, 2008.

[92] M. Fox. *Quantum Optics: An Introduction*. Oxford Master Series in Physics. Oxford University Press, Oxford, New York, 2006.

[93] D. DeMille. Quantum Computation with Trapped Polar Molecules. *Physical Review Letters*, **88**(6), 4, 2002.

[94] K. K. Ni, T. Rosenband, and D. D. Grimes. Dipolar exchange quantum logic gate with polar molecules. *Chemical Science*, **9**(33), 6830–6838, 2018.

[95] J. A. Blackmore, L. Caldwell, P. D. Gregory, E. M. Bridge, R. Sawant, J. Aldegunde, J. Mur-Petit, D. Jaksch, J. M. Hutson, B. E. Sauer, M. R. Tarbutt, and S. L. Cornish. Ultracold molecules for quantum simulation: Rotational coherences in CaF and RbCs. *Quantum Science and Technology*, **4**(1), 014010, 2019.

[96] P. Yu, L. W. Cheuk, I. Kozyryev, and J. M. Doyle. A scalable quantum computing platform using symmetric-Top molecules. *New Journal of Physics*, **21**(9), 093049, 2019.

[97] M. Brouard, D. H. Parker, and S. Y. T. van de Meerakker. Taming molecular collisions using electric and magnetic fields. *Chemical Society Reviews*, **43**(21), 7279–7294, 2014.

[98] G. Tang, M. Besemer, S. Kuijpers, G. C. Groenenboom, A. van der Avoird, T. Karman, and S. Y. T. van de Meerakker. Quantum state–resolved molecular dipolar collisions over four decades of energy. *Science*, **379**(6636), 1031–1036, 2023.

[99] N. Vanhaecke, U. Meier, M. Andrist, B. H. Meier, and F. Merkt. Multistage Zeeman deceleration of hydrogen atoms. *Physical Review A*, **75**(3), 031402, 2007.

[100] E. Narevicius, A. Libson, C. G. Parthey, I. Chavez, J. Narevicius, U. Even, and M. G. Raizen. Stopping supersonic beams with a series of pulsed electromagnetic coils: An atomic coilgun. *Physical Review Letters*, **100**(9), 093003, 2008.

[101] E. S. Shuman, J. F. Barry, and D. DeMille. Laser cooling of a diatomic molecule. *Nature*, **467**(7317), 820–823, 2010.

[102] D. McCarron. Laser cooling and trapping molecules. *Journal of Physics B: Atomic, Molecular and Optical Physics*, **51**(21), 212001, 2018.

[103] N. J. Fitch and M. R. Tarbutt. Laser-cooled molecules. *Advances In Atomic, Molecular, and Optical Physics*, **70**, 157–262, 2021.

[104] J. Wang, V. A. Shamamian, B. R. Thomas, J. M. Wilkinson, J. Riley, C. F. Giese, and W. R. Gentry. Speed ratios greater than 1000 and temperatures less than 1 mK in a pulsed he beam. *Physical Review Letters*, **60**(8), 696–699, 1988.

[105] J. F. Barry, E. S. Shuman, E. B. Norrgard, and D. DeMille. Laser Radiation Pressure Slowing of a Molecular Beam. *Physical Review Letters*, **108**(10), 103002, 2012.

[106] B. Hemmerling, E. Chae, A. Ravi, L. Anderegg, G. K. Drayna, N. R. Hutzler, A. L. Collopy, J. Ye, W. Ketterle, and J. M. Doyle. Laser slowing of CaF molecules to near the capture velocity of a molecular MOT. *Journal of Physics B: Atomic, Molecular and Optical Physics*, **49**(17), 174001, 2016.

[107] W. E. Ernst, J. Kändler, and T. Törring. Hyperfine structure and electric dipole moment of BaF $X^2\Sigma^+$. *The Journal of Chemical Physics*, **84**(9), 4769–4773, 1986.

[108] D. H. Murphree. *Nuclear Spin-Dependent Parity Nonconservation in Diatomic Molecules*. PhD thesis, Yale University, 2009.

[109] J. L. Wen, J. D. Tang, J. F. Dong, X. J. Du, S. M. Hu, and Y. R. Sun. Doppler-free spectroscopy of an atomic beam probed in traveling-wave fields. *Physical Review A*, **107**(4), 042811, 2023.

[110] C. Effantin, A. Bernard, J. d'Incan, G. Wannous, J. Vergès, and R. F. Barrow. Studies of the electronic states of the baf molecule part I: Effective constants for seven states below 30 000 cm^{-1}. *Molecular Physics*, **70**(5), 735–745, 1990.

[111] M. Rockenhäuser, F. Kogel, E. Pultinevicius, and T. Langen. Absorption spectroscopy for laser cooling and high-fidelity detection of barium monofluoride molecules. *Physical Review A*, **108**, 062812, 2023.

[112] M. C. Mooij, H. L. Bethlem, A. Boeschoten, A. Borschevsky, K. Esajas, T. H. Fikkers, S. Hoekstra, J. W. F. van Hofslot, K. Jungmann, V. R. Marshall, T. B. Meijknecht, R. G. E. Timmermans, A. Touwen, W. Ubachs, L. Willmann, and Y. Yin. Influence of source parameters on the longitudinal phase-space distribution of a pulsed cryogenic beam of barium fluoride molecules. *New Journal of Physics*, **26**(5), 053009, 2024.

[113] K.-K. Ni, S. Ospelkaus, M. H. G. De Miranda, A. Pe'er, B. Neyenhuis, J. J. Zirbel, S. Kotochigova, P. S. Julienne, D. S. Jin, and J. Ye. A High Phase-Space-Density Gas of Polar Molecules. *Science*, **322**(5899), 231–235, 2008.

[114] N. F. Ramsey. *Molecular Beams*. Oxford Classic Texts in the Physical Sciences. Oxford University Press, Oxford, New York, 1985.

[115] S. DePaul, D. Pullman, and B. Friedrich. A pocket model of seeded supersonic beams. *Journal of Physical Chemistry*, **97**(10), 2167–2171, 1993.

[116] G. M. Davis, M. C. Gower, C. Fotakis, T. Efthimiopoulos, and P. Argyrakis. Spectroscopic studies of ArF laser photoablation of PMMA. *Applied Physics A*, **36**(1), 27–30, 1985.

[117] R. deCarvalho, J. Doyle, B. Friedrich, T. Guillet, J. Kim, D. Patterson, and J. Weinstein. Buffer-gas loaded magnetic traps for atoms and molecules: A primer. *European Physical Journal D*, **7**(3), 289–309, 1999.

[118] N. J. Simon, E. S. Drexler, and R. P. Reed. Properties of copper and copper alloys at cryogenic temperatures. Final report. *National Institute of Standards and Technology*, 1992.

[119] D. Xiao, D. M. Lancaster, C. H. Allen, M. J. Taylor, T. A. Lancaster, G. Shaw, N. R. Hutzler, and J. D. Weinstein. Shaped nozzles for cryogenic buffer-gas beam sources. *Physical Review A*, **99**(1), 013603, 2019.

[120] T. H. Fikkers *et al.* (NL-*e*EDM collaboration). in preparation.

[121] C. Ryzlewicz and T. Törring. Formation and microwave spectrum of the 2Σ-radical barium-monofluoride. *Chemical Physics*, **51**(3), 329–334, 1980.

[122] A. Bernard, C. Effantin, J. d'Incan, J. Verges, and R. F. Barrow. Studies of the electronic states of the baf molecule part II: The 5d(v = 0, 1, 2) states. *Molecular Physics*, **70**(5), 747–755, 1990.

[123] R. A. Frosch and H. M. Foley. Magnetic hyperfine structure in diatomic molecules. *Physical Review*, **88**(6), 1337–1349, 1952.

List of publications

Chapter 5 is based on:
M. C. Mooij, H. L. Bethlem, A. Boeschoten, A. Borschevsky, T. H. Fikkers, S. Hoekstra, J. W. F. van Hofslot, K. Jungmann, V. R. Marshall, T. B. Meijknecht, R. G. E. Timmermans, A. Touwen, W. Ubachs, and L. Willmann, "A method to determine the phase-space distribution of a pulsed molecular beam" *Journal of Physics B*, **58**(1), 015303, 2025.
Contributions: Design and construction of the experiment, data taking and analysis, writing the first draft of the manuscript.

Chapter 6 is based on:
M. C. Mooij, H. L. Bethlem, A. Boeschoten, A. Borschevsky, K. Esajas, T. H. Fikkers, S. Hoekstra, J. W. F. van Hofslot, K. Jungmann, V. R. Marshall, T. B. Meijknecht, R. G. E. Timmermans, A. Touwen, W. Ubachs, L. Willmann, and Y. Yin, "Influence of source parameters on the longitudinal phase-space distribution of a pulsed cryogenic beam of barium fluoride molecules" *New Journal of Physics*, **26**(5), 053009, 2024.
Contributions: Design and construction of the experiment, data taking and analysis, writing the first draft of the manuscript.

The author also contributed to:
P. Aggarwal, H. L. Bethlem, A. Borschevsky, M. Denis, K. Esajas, P. A. Haase, Y. Hao, S. Hoekstra, K. Jungmann, T. B. Meijknecht, M. C. Mooij, R. G. E. Timmermans, W. Ubachs, L. Willmann, and A. Zapara, "Measuring the electric dipole moment of the electron in BaF" *European Physical Journal D*, **72**(11), 197, 2018.
Contributions: Proofreading of the manuscript.

Y. Hao, L. F. Pa˘steka, L. Visscher, P. Aggarwal, H. L. Bethlem, A. Boeschoten, A. Borschevsky, M. Denis, K. Esajas, S. Hoekstra, K. Jungmann, V. R. Marshall, T. B. Meijknecht, M. C. Mooij, R. G. E. Timmermans, A. Touwen, W. Ubachs, L. Willmann, Y. Yin, and A. Zapara, "High accuracy theoretical investigations of CaF, SrF, and BaF and implications for laser-cooling" *The Journal of Chemical Physics*, **151**(3), 34302, 2019.
Contributions: Discussion of results, proofreading of the manuscript.

P. Aggarwal, V. R. Marshall, H. L. Bethlem, A. Boeschoten, A. Borschevsky, M. Denis, K. Esajas, Y. Hao, S. Hoekstra, K. Jungmann, T. B. Meijknecht, M. C. Mooij, R. G. E. Timmermans, A. Touwen, W. Ubachs, S. M. Vermeulen, L. Willmann, Y. Yin, and

A. Zapara, "Lifetime measurements of the $A^2\Pi_{1/2}$ and $A^2\Pi_{3/2}$ states in BaF" *Physical Review A*, **100**(5), 52503, 2019.
Contributions: Discussion of results, proofreading of the manuscript.

P. Aggarwal, H. L. Bethlem, A. Boeschoten, A. Borschevsky, K. Esajas, Y. Hao, S. Hoekstra, K. Jungmann, V. R. Marshall, T. B. Meijknecht, M. C. Mooij, R. G. E. Timmermans, A. Touwen, W. Ubachs, L. Willmann, Y. Yin, and A. Zapara, "A supersonic laser ablation beam source with narrow velocity spreads" *Review of Scientific Instruments*, **92**(3), 33202, 2021.
Contributions: Discussion of results, proofreading of the manuscript.

P. A. Haase, D. J. Doeglas, A. Boeschoten, E. Eliav, M. Iliaš, P. Aggarwal, H. L. Bethlem, A. Borschevsky, K. Esajas, Y. Hao, S. Hoekstra, V. R. Marshall, T. B. Meijknecht, M. C. Mooij, K. Steinebach, R. G. E. Timmermans, A. P. Touwen, W. Ubachs, L. Willmann, and Y. Yin, "Systematic study and uncertainty evaluation of P,T-odd molecular enhancement factors in BaF" *Journal of Chemical Physics*, **155**(3), 034309, 2021.
Contributions: Discussion of results, proofreading of the manuscript.

P. Aggarwal, Y. Yin, K. Esajas, H. L. Bethlem, A. Boeschoten, A. Borschevsky, S. Hoekstra, K. Jungmann, V. R. Marshall, T. B. Meijknecht, M. C. Mooij, R. G. E. Timmermans, A. Touwen, W. Ubachs, and L. Willmann, "Deceleration and Trapping of SrF Molecules" *Physical Review Letters*, **127**(17), 173201, 2021.
Contributions: Discussion of results, proofreading of the manuscript.

M. Denis, P. A. B. Haase, M. C. Mooij, Y. Chamorro, P. Aggarwal, H. L. Bethlem, A. Boeschoten, A. Borschevsky, K. Esajas, Y. Hao, S. Hoekstra, J. W. F. van Hofslot, V. R. Marshall, T. B. Meijknecht, R. G. E. Timmermans, A. Touwen, W. Ubachs, L. Willmann, and Y. Yin, "Benchmarking of the Fock-space coupled-cluster method and uncertainty estimation: Magnetic hyperfine interaction in the excited state of BaF" *Physical Review A*, **105**(5), 52811, 2022.
Contributions: Discussions, theoretical investigations and writing first draft of the sections "Introduction" and "Comparison of theoretical and experimental results", proofreading of the rest of the manuscript.

A. Boeschoten, V. R. Marshall, T. B. Meijknecht, A. Touwen, H. L. Bethlem, A. Borschevsky, S. Hoekstra, J. W. F. van Hofslot, K. Jungmann, M. C. Mooij, R. G. E. Timmermans, W. Ubachs, and L. Willmann, "Spin-precession method for sensitive electric dipole moment searches" *Physical Review A*, **110**(1), L010801, 2024.
Contributions: Discussion of results, proofreading of the manuscript.

A. Touwen, J. W. F. van Hofslot, T. Qualm, R. Borchers, R. Bause, H. L. Bethlem, A. Boeschoten, A. Borschevsky, T. H. Fikkers, S. Hoekstra, K. Jungmann, V. R. Marshall, T. B. Meijknecht, M. C. Mooij, R. G. E. Timmermans, W. Ubachs, L. Willmann, and NL-eEDM collaboration, "Manipulating a beam of barium fluoride molecules using an electrostatic hexapole" *New Journal of Physics*, **26**(7), 073054, 2024.
Contributions: Discussion of results, proofreading of the manuscript.

Samenvatting

In deze samenvatting tracht ik uit te leggen wat ik in mijn lab heb bereikt de afgelopen jaren en wat er in het proefschrift “Een cryogene buffergas bundel bron van BaF moleculen” staat.

Om te beginnen, wil ik een heel eind uitzoomen. Ik heb (een heel klein stukje) van de wereld om ons heen onderzocht om deze beter te begrijpen en deze (beter) te kunnen beschrijven in een natuurkundig model. Een methode (een reductionistische) is om alle materie en hun interacties te beschrijven aan de hand van een aantal elementaire deeltjes. Elementair betekent dat het deeltje zelf niet verder opgesplitst kan worden. Waar voorheen ‘water’ als elementair werd beschouwd, bleek later dat er een kleiner elementair deeltje bestond, namelijk een watermolecuul. Maar dit molecuul kon wederom opgebouwd worden uit kleinere deeltjes, namelijk atomen, enzovoorts. Deze zoektocht naar de echte elementaire deeltjes heeft geleid tot het Standaardmodel der elementaire deeltjes (SM), dat bestaat uit 17 elementaire deeltjes die materie en de interacties tussen materie beschrijft.

Materie-antimaterie asymmetrie

Met het SM kunnen vele processen in de wereld nauwkeurig beschreven worden, maar de wereld blijkt complexer dan dit model. Bijvoorbeeld lijkt er wel een hoop materie te zijn, namelijk alles waaruit de wereld om ons heen uit bestaat, maar (vrijwel) geen antimaterie te zijn. Antimaterie lijkt erg op materie, maar heeft een omgekeerde lading. Het kan, samen met het overeenkomstige materie deeltje, gevormd worden vanuit een hoeveelheid energie of visa versa. Echter, het SM voorspelt dat in dit proces een gelijke ‘symmetrische’ hoeveelheid antimaterie als materie wordt gevormd.

Aangezien een natuurkundig model zoals het SM als doel heeft de wereld te beschrijven, heeft, bij een tegenstrijdigheid tussen model en de wereld, de wereld gelijk en moet het model dus aangepast. Er is dan verbeterde theorie nodig en deze moet experimenteel getest worden. In het geval van het SM zijn er vele ‘voorbij het SM’ theorieën bedacht, die vaak doormiddel van nieuwe zwaardere deeltjes beter de processen trachten te beschrijven dan het SM doet.

Een belangrijk onderdeel van het SM is dat veel processen symmetrisch zijn bij inversie van tijd, lading en ruimtelijke coördinaten, ook wel tijdinversie (T), lading conjugatie (C van het Engelse ‘charge’) en pariteit (P) symmetrie genoemd. Een voorbeeld van T-symmetrie is dat (volgens het SM) het proces van de vorming van een

materie en antimaterie deeltje uit energie zich hetzelfde gedraagt als het verdwijnen ('annihileren') van die twee deeltjes in energie. Om dus een asymmetrie in de hoeveelheid materie en antimaterie te kunnen verklaren, wordt (o.a.) de oplossing gezocht in 'nieuwe deeltjes' die zorgen voor schending van de symmetrieën. Specifiek wordt gezocht naar schending van de gecombineerde CP-symmetrie of T-symmetrie (volgens de CPT-theorema zijn CP en T-symmetrie (in veel gevallen) gelijk aan elkaar).

Symmetrie schendende theorieën testen

Maar hoe kun je deze symmetrie schendende theorieën testen? Daarvoor moet een systeem gemeten worden dat symmetrie schendt, zoals een elektron dat een elektrisch dipool moment (*e*EDM) heeft. Binnen het SM is het elektron een elementair deeltje met een puntmassa en een negatieve lading. Deze lading lijkt symmetrisch te zijn en te overlappen met het massamiddelpunt. T-schendende theorieën 'voorbij het SM' voorspellen echter zware deeltjes en processen die de ladingsverdeling een heel klein beetje verstoren, waardoor de lading een spreiding krijgt met een iets meer negatieve kant en een wat minder negatieve kant, dit heet een dipool moment. Dit is waar onze groep, de NL-*e*EDM collaboratie, onderzoek naar doet: een zoektocht naar een elektrisch dipoolmoment van het elektron.

Een *e*EDM schendt T-symmetrie op de volgende manier. Een fundamentele eigenschap van het elektron is de 'spin', de kwantummechanische versie van een rotatie om zijn as. Een mogelijk elektrisch dipool moment moet (vanwege niet nader te bepalen redenen) langs dezelfde as liggen als de spin, de relatieve richting t.o.v. de spin is (nog) niet bekend. Bij T-symmetrie is de draaiing van het elektron omgekeerd, en daarmee de richting van de spin. De richting van het elektrische dipool moment blijft echter dezelfde kant op staan. De richting van de spin en het elektrisch dipool moment zijn dus ten opzichte van elkaar anders na tijdinversie en daarmee is een *e*EDM niet T-symmetrisch.

Binnen het SM zijn symmetrie schendende deeltjes en processen zo zeldzaam en zwak dat een mogelijk *e*EDM veel kleiner is dan met de huidige meetgevoeligheid kan worden gemeten. Echter, aangezien de 'voorbij het SM' theorieën veel grotere schending van T-symmetrie bevatten, voorspellen ze een veel grotere waarde voor de *e*EDM. Een waarde die, afhankelijk van de theorie, dichtbij de huidige meetgevoeligheid kan liggen. De zoektocht naar een *e*EDM is dus een algemene methode om verschillende nieuwe theorieën te testen. Het is tevens ook selectief voor alleen 'voorbij het SM' theorieën, dus een *e*EDM meten zou geen bevestiging van het SM kunnen zijn maar echt 'voorbij het SM' theorieën aantonen.

Een elektrisch dipool meten

Hoe meet je een elektrisch dipool moment? In de basis is het vrij simpel: als iets een elektrisch dipool moment heeft zal het gaan oriënteren in de richting van een elektrisch veld. De praktijk is zoals altijd lastiger. Ten eerste is een elektron geladen, dus al heeft het een klein dipool moment, in een elektrisch veld zal het voordat het goed en wel kan oriënteren versnellen naar de positieve elektrode. Ten tweede is het mogelijke dipool moment extreem klein en dus is een hele gevoelige meetmethode nodig. Een oplossing voor het eerste probleem is om een elektron meten in een neutraal systeem. Polaire moleculen zijn hier erg geschikt voor en wij gebruiken BaF moleculen. Hoewel een BaF molecuul meerdere elektronen bevat, zijn de meesten sterk gebonden in het molecuul, en is het effectief een systeem met één vrij bewegend elektron, die gebruikt wordt in de *e*EDM meting. Bijkomend voordeel is dat in een zwaar molecuul zoals BaF het interne elektrisch veld een miljoen keer sterker is dan dat er redelijkerwijs in het lab gemaakt kan worden. Dit verbetert de gevoeligheid van de meting aanzienlijk. Hierbij is het wel vereist dat het molecuul zelf polair is, zodat er controle mogelijk is over de oriëntatie van het molecuul en daarmee de oriëntatie van het interne elektrisch veld.

Het NL-*e*EDM ontwerp

Het elektron in een molecuul kan zich in verschillende energiebanen (ook wel energietoestanden) bevinden, vergelijkbaar met het atoommodel van Bohr. Als een elektron een elektrisch dipool moment heeft, zal de energiebaan van het elektron een klein beetje veranderen. Deze verschuiving is echter zo klein, dat direct meten niet haalbaar is. We meten daarom het verschil tussen twee energiebanen waarin de spin van het elektron omgekeerd is. In onze methode wordt het elektron in twee energiebanen tegelijkertijd (een 'superpositie') gebracht. Vervolgens laten we een wolk van deze moleculen een stukje door een magneetveld vliegen en daardoor is er tijdelijk een energieverschil tussen de toestanden. Nadat de moleculen uit het magneetveld zijn gevlogen, kunnen we meten hoe groot het energie verschil tijdelijk was. Als we tegelijkertijd ook elektrische velden aanbrengen zou er, in het geval van een *e*EDM, nog een extra energieverschil zijn. Bijvoorbeeld als we het elektrisch en magnetisch veld in dezelfde richting genereren, neemt het energieverschil nog iets verder toe (aangenomen dat het elektrisch dipool moment positief is). Als we van een van de velden de richting omdraaien, neemt het energieverschil af. Door deze twee situaties te vergelijken kunnen we heel precies meten of er een extra verschuiving is en dus een niet nul *e*EDM. Als er geen verschil is tussen de metingen kan een bovengrens van het *e*EDM worden bepaald.

De experimentele opstelling van de NL-*e*EDM collaboratie is een 'bundel' experiment, waarbij op 10 Hz wolkjes moleculen, in vacuüm, horizontaal door verschillende

componenten van de opstelling bewegen. Om de *e*EDM te meten, worden de moleculen met een laser in de 'superpositie' toestand gebracht. Vervolgens vliegen ze door een zone waar zich een (erg stabiel en homogeen) elektrisch en magnetisch veld bevindt, waarna het energieverschil tussen de twee toestanden gemeten wordt, wederom met lasers.

Het ontwerp van het NL-*e*EDM experiment focust op het verbeteren van de gevoeligheid. Ten eerste door zoveel mogelijk moleculen te meten en ten tweede door zo langzaam mogelijk deze moleculen te laten vliegen, zodat ze zich zo lang mogelijk in de velden bevinden. De opstelling bestaat daarom uit de volgende onderdelen: een molecuulbron, die BaF moleculen in gas fase maakt en waaruit een bundel (het wolkje) moleculen met een snelheid van ongeveer 200 m/s vliegt. Deze bundel wordt via een elektrostatische lens efficiënt in een 'molecuul afremmer' gemikt, waarin met tijd-variërende elektrische velden de voorwaartse snelheid drastisch verlaagd wordt tot ongeveer 30 m/s. De moleculen vliegen niet alleen naar voren, maar ook altijd een beetje opzij, dat leidt tot verlies van moleculen. Daarom wordt deze beweging opzij ook afgeremd door middel van laser licht.

De molecuul bron

Het onderwerp van dit proefschrift is het ontwerpen, bouwen, testen en begrijpen van de bron van BaF moleculen. Het belangrijkste doel voor de bron is: zo veel mogelijk 'geschikte' moleculen met een zo laag mogelijke snelheid verkrijgen, zodat ze efficiënt verder afgeremd kunnen worden. BaF moleculen zijn erg reactief en reageren gemakkelijk tot een ander molecuul. Het zout BaF_2 komt van nature wel voor als vaste stof bij kamertemperatuur, maar is lastig in gasfase te krijgen en verliest niet makkelijk een fluor atoom. Wij beginnen daarom met puur barium, waar we met een korte en intense laserpuls wat atomen vanaf verdampen, ook wel ablatie geheten. Deze atomen reageren vervolgens met een fluorrijk gas, zwavelhexafluoride (SF_6), waarbij onder andere BaF gevormd wordt.

Bij dit ablatieproces en de chemische reactie komt veel energie vrij en daardoor worden de moleculen warm. Dat willen we om twee redenen niet. Ten eerste bewegen warme moleculen heel snel, dus als we hier een bundel van zouden maken is de gemiddelde snelheid van de moleculen veel te hoog, terwijl we juist een langzame bundel wilden. Ten tweede willen we graag zoveel mogelijk 'geschikte' moleculen, en geschikt betekent dat ze allemaal in dezelfde rotatie en vibratie kwantumtoestand zitten, dat wil zeggen, het buitenste elektron van alle moleculen moet in dezelfde energiebaan zitten. Echter, bij warm gas hebben de moleculen genoeg energie om in verschillende banen te zitten. We willen dus graag zo koud mogelijke moleculen.

Om de moleculen af te koelen, laten we ze botsen met 'cryogeen buffergas'. Cryogeen betekent dat het gas heel koud is (20 Kelvin, ongeveer -253 graden Celsius) en het buffergas bestaat uit neon gas dat zelf niet reageert met de moleculen en alleen dient om de warmte van de moleculen over te nemen en af te voeren. Hierbij is een praktisch detail, dat we voor efficiënt afkoelen veel botsingen tussen de moleculen en het neon gas willen hebben, maar eenmaal koud vooral geen botsingen willen, zodat ze ongestoord een paar meter door de *e*EDM meetopstelling kunnen vliegen. Wij lossen dit op door alle processen van barium ablatie, chemische reactie tot BaF en buffergas koeling in een bijna afgesloten ruimte, de 'cel', te laten plaatsvinden, waarin de neon dichtheid redelijk hoog kan zijn. Aan één kant van de cel zit een gaatje, waardoorheen het mengsel van moleculen en buffergas een veel grotere ruimte in kan ontsnappen, om zo een bundel van moleculen te vormen. Deze ruimte wordt met vacuümpompen op een zo laag mogelijke druk gehouden, zodat de bundel ongestoord zijn weg kan vervolgen. Om een constante neon druk in de cel te houden, stroomt er continue nieuw buffergas de cel in (aan de overzijde van de cel ten opzichte van de uitgang). Daardoor ontstaat er een langzame stroming van neon gas in de cel, waarin periodiek barium moleculen gevormd worden die met de stroming mee de cel verlaten.

In **hoofdstuk 2** wordt het technisch ontwerp en de werking van de molecuul bron beschreven. Een doorsnede van de 3D tekeningen van de bron zijn verwerkt in de omslag van dit proefschrift. De belangrijkste onderdelen zijn de koperen cel binnenin, de metalen vacuümkamers om een lage druk te bereiken, een cryopomp om de cel op 20 K te krijgen, gasleidingen om neon en SF_6 gas in de cel te krijgen en de montage van het blokje barium aan een kleine motor, om zo een groter oppervlakte van het blokje te gebruiken om vanaf te verdampen.

Om een ideale bundel te kunnen maken, moet de bundel ook gemeten worden. **Hoofdstuk 3** beschrijft de benodigde opstelling hiervoor. We gebruiken hiervoor nabij-infrarood laserlicht, waarvan de frequentie (de kleur) heel precies kan worden afgesteld zodat alleen de 'geschikte' BaF moleculen dit licht kunnen absorberen en alle andere BaF moleculen, neon atomen, etc niet onze meting verstoren. We kunnen het laser licht ook precies uitlijnen op de juiste positie en in de gewenste richting. We hebben in de opstelling twee meetpunten.

Dichtbij de uitgang van de cel, loopt een laserbundel dwars door de molecuulbundel. We meten vervolgens hoeveel licht er geabsorbeerd wordt door de moleculen. Hieruit kunnen we o.a. het aantal moleculen in de bundel bepalen. Op 780 mm van de uitgang van de cel doorkruist een tweede laserbundel de molecuulbundel. Hier absorberen de moleculen opnieuw het licht en nemen hierdoor een beetje energie op, ze raken 'aangeslagen'. Vervolgens vervallen ze terug en daarbij zenden ze weer licht uit, in een willekeurige richting. Dit uitgezonden licht kunnen we heel gevoelig meten. Deze 'Laser geïnduceerde fluorescentie (LIF)' techniek is gevoeliger dan de absorptiemeting

en dat is nodig omdat de molecuulbundel terwijl het door de opstelling vliegt ook opzij uitdijt en dus steeds een lagere dichtheid krijgt. In hoofdstuk 5 beschrijven we hoe we LIF gebruiken om de snelheid van de bundel te bepalen.

Een belangrijk onderdeel van de laseropstelling is het stabiliseren van de frequentie van de laser. Hiervoor is een frequentiekam gebruikt. Dit is een speciale laser die in onze opstelling functioneert als een hele exacte en stabiele referentie frequentie waarmee we onze laserfrequentie vergelijken. Hierdoor kan een laserfrequentie van bijvoorbeeld 348666402 MHz op 1 MHz nauwkeurig worden gestabiliseerd. Deze nauwkeurigheid geeft zoveel resolutie, dat ook de beweging van de moleculen te meten is. Dit werkt als volgt: Vergelijkbaar met het Doppler effect in lucht, ziet een bewegend molecuul een net wat andere frequentie ($\sim$100 MHz hoger of lager) van het laserlicht. Tegelijkertijd absorberen moleculen maar erg selectief alleen frequenties binnen 2.7 MHz van hun gewenste frequentie. Een verschuiving van 100 MHz vereist dus een aanpassing van de laserfrequentie. Aangezien we onze laserfrequentie heel precies kunnen meten, kunnen we aan de hand van de verschuiving van de frequentie zeggen hoe snel het molecuul beweegt. In **hoofdstuk 4** gebruiken we de meetopstelling beschreven in hoofdstuk 3 om de thermodynamische eigenschappen van de molecuulbundel uitvoerig te meten en karakteriseren. We meten onder andere de duur van de molecuulpuls (0.9 ms), de zijwaartse snelheid (93 m/s), de breedte van de bundel (4.4 mm) en de interne warmte van de moleculen. Dit laatste zegt iets over de hoeveel 'geschikte' moleculen. We gebruiken al deze metingen om aan het einde van het hoofdstuk het aantal 'geschikte' moleculen in één molecuulpuls te berekenen. Dit zijn er ongeveer 1.8×10^{10} moleculen.

Hoofdstuk 5 bevat ons gepubliceerde werk over een methode om de voorwaartse snelheid van de molecuulbundel te meten. Deze methode bevat twee stappen. Zoals ook beschreven bij hoodfstuk 3, is op precies 780 mm van de uitgang van de bron een laserbundel dwars op de molecuulbundel uitgelijnd. Door absorptie van dit laser licht, wordt het vrije elektron in een molecuul in een hogere 'aangeslagen' energiebaan gebracht. Een tweede laserbundel is in de tegenovergestelde richting t.o.v. de molecuulbundel uitgelijnd (en dus dwars op de eerste laserbundel). Het licht van deze laser brengt het elektron vanuit de 'aangeslagen' energiebaan naar een nog hogere energiebaan. Vervolgens vervalt het elektron helemaal terug en de hoeveelheid licht die daarbij uitgezonden wordt meten we. Aangezien de moleculen richting het licht van de tweede laser bewegen, is er een groot Doppler effect en moet de frequentie van dit laserlicht iets lager afgesteld worden. Deze mate van verschuiving (ten opzichte van de Doppler vrije frequentie) geeft de informatie over de snelheid. Hoewel de informatie over de snelheid alleen zichtbaar is in de frequentie van de tweede laser (de eerste laser staat immers dwars op beweging van de molecuulbundel) verbetert het gebruik van de eerste laser de meting aanzienlijk. De eerste laser beperkt namelijk waar de snelheid gemeten wordt. Zou de snelheid met een enkele laser gemeten worden, dan zouden

moleculen het hele pad vanaf de uitgang van de cel tot de detector het laserlicht zien en daardoor 'aangeslagen' kunnen raken en vervolgens licht uitzenden voordat ze bij de detector zijn. Omdat bij dit uitzenden van licht een molecuul vaak in een andere energiebaan belandt dan het begon, wordt het molecuul onzichtbaar voor het laserlicht. Eenmaal bij de detector zijn dan nog maar weinig moleculen zichtbaar.

Daarnaast zorgt de eerste laser ervoor dat de positie van de moleculen op het moment van licht uitzenden nauwkeurig bekend is. Omdat bij elke frequentieverschuiving van de tweede laser, het uitgezonden licht ook met een hoge tijdsresolutie gemeten wordt, is van alle moleculen de snelheid en bijbehorende aankomsttijd bekend bij een bepaalde positie. Deze gecombineerde snelheid-tijd (of snelheid-positie) distributie heet een faseruimte distributie.

In de faseruimte metingen is te zien dat eerst de snelle en pas later de langzame moleculen aankomen bij de detector. Dit resultaat is niet onverwachts (en niet zo interessant), omdat de moleculen 780 mm moesten afleggen tot de detector. Echter, omdat van alle moleculen afzonderlijk de snelheid en aankomsttijd bekend is, kan de aankomsttijd ook voor een andere positie berekend worden. Een zeer interessante positie is direct achter de uitgang van de cel. Verrassend genoeg komen ook daar in eerste instantie vooral snelle moleculen uit de bron. Dit was een onverwachte uitkomst en aanleiding voor het artikel beschreven in hoofdstuk 6. Deze faseruimte distributie bij de uitgang van de cel is verwerkt in de omslag van het proefschrift, waarbij de zichtbaarheid van de 3D-tekening de vorm heeft van de faseruimte distributie uit de linkerhelft van Figuur 5.6.

In **hoofdstuk 6** analyseren we de werking van de bron in detail aan de hand van de 'naar de bron teruggerekende' faseruimte distributie metingen. Hierbij gebruiken we het feit dat de snelheid van de moleculen in de bundel afhangt van de druk en temperatuur in de cel. Bij de uitgang van de cel, is er een drukverschil tussen de neon druk in de cel en de verwaarloosbare druk buiten de cel, waardoor de neon atomen en BaF moleculen naar buiten versneld worden. Hoe groter het verschil in de druk, hoe meer de versnelling. In deze versnelling naar buiten, wordt onderling beweging van de deeltjes in de bundel (dit is de definitie van de temperatuur van de bundel), omgezet in gezamenlijke de voorwaartse snelheid. Aangezien de temperatuur niet lager dan 0 Kelvin kan worden, bepaalt de begintemperatuur van de deeltjes in de cel dus de maximale voorwaartse snelheid die de bundel kan krijgen buiten de cel. Dit verband geeft ons de mogelijkheid om met een meting *buiten* de cel iets te zeggen over wat er *in* de cel gebeurt.

We hebben deze analysemethode toegepast op een heleboel metingen, bij allerlei verschillende instellingen van de bron, zoals de temperatuur van de cel en de ablatie energie. De combinatie van deze metingen gaf ons veel inzicht in de onderliggende oorzaak van de vorm van de faseruimte distributie, namelijk wat er allemaal *binnen in*

de cel gebeurt. We konden hier 3 stappen in onderscheiden: (1) de ablatie van barium atomen zorgt voor tijdelijke opwarming van het neon buffergas. We zien daarom eerst een toename van snelheid en daarna een geleidelijke afname. (2) De snelheid waarmee het buffergas afkoelt neemt af als de wand van de cel vervuild raakt met een laagje bariumpoeder. (3) Naast opwarming van het buffergas door de geableerde bariumatomen, wordt het buffergas ook opgewarmd door het bariumblokje dat zelf opwarmt van het ablatieproces. De afkoeling hiervan duurt veel langer dan de puls, en dus is deze warmte ook nog aanwezig na de snelle afkoeling van punt (2). Er ontstaat een (tijdelijke) temperatuurgradiënt door de cel heen, vanaf het warme bariumblokje tot de uitgang van de cel. Hierdoor hangt de gemeten snelheid af van de lengte van de cel. Bij een korte de afstand tussen het warme bariumblokje en de uitgang van de cel, is de temperatuur hoger bij de uitgang van de cel, dan bij langere afstanden. Deze metingen en het verkregen begrip van de werking van de bron helpen ons met het verder optimaliseren van de bron.

In **hoofdstuk 7** vat ik de belangrijkste resultaten samen. De gemeten parameters uit hoofdstuk 4 zijn samengevat in een tabel en de belangrijkste resultaten van de faseruimte distributie metingen uit hoofdstuk 6 zijn samengevat in een grafiek.

Dankwoord

Na meer dan 7 jaar komt er dan toch echt een einde aan mijn promotietraject. Een bijzonder traject dat verweven liep met vele veranderingen in mijn privéleven. Ik zou daarom een aantal belangrijke mensen van de afgelopen jaren willen bedanken.

Allereerst Rick. Op Ameland vertelde jij over het eEDM project en ik merkte toen meteen dat je een heel fijn persoon bent om mee samen te werken. Hoewel ik niet veel van moleculen wist, heb je me de kans gegeven aan dit mooie project te werken. Het was een project dat goed bij me paste, met als basis een opstelling bouwen die vol met AMO fysica zit en tegelijkertijd met als doel een grotere fundamentele vraag beantwoorden. Je bent altijd betrokken geweest en had altijd een goede toon (ook bij kritiek), waardoor ik op mijn gemak was en niet bang was om vragen te stellen. Ik kwam daardoor goed tot mijn recht en ging ontspannen naar de VU en daar ben ik je erg dankbaar voor! Je hebt me op allerlei manieren geholpen en heel veel geleerd, van opstarten in een leeg lab, genoeg uitzoomen voor presentaties, kritisch en wetenschappelijk mijn resultaten beoordelen (met altijd de vraag 'wat heb je veranderd?') tot artikelen en een proefschrift schrijven. Ik denk dat we samen veel hebben geleerd van de fysica van een cryogene bron en BaF spectroscopie en een goede tijd hebben gehad. Dankjewel voor alles!

Wim, hoewel je zeker in het begin wat meer op de achtergrond bleef, heb ik altijd je steun gevoeld en stond je klaar om mee te denken waar nodig. Veel dank voor alle hulp, met name rond spectroscopie en de artikelen en dit proefschrift schrijven!

Wander, waar ik in eerste instantie redelijk alleen in het lab zat, veranderde dat toen jij in het lab ernaast begon. Er kwam een hoop gezelligheid bij met de vele koffies, lunches en na corona ook conferenties. Met je scherpe luisterende oor heb je me een heel stuk secuurder gemaakt als ik iets vertel, wetende dat je elke kleine fout zal corrigeren. Je hebt me vaak en veel geholpen in het lab, met even een laser alvast aan zetten of de cryopomp aan dan wel uit zetten. Dankjewel!

Elmer, de afgelopen twaalf jaar hebben we vrijwel alles op de universiteit samen of vergelijkbaar gedaan, meestal maar een paar labs uit elkaar. Ik vind het daarom erg leuk dat we elkaars paranimfen zijn. Buiten de natuurkunde natuurlijk de molen, samen fietsen, waarbij je me oneindig weetjes en verhalen hebt verteld en natuurlijk de vakanties. Hoogtepunten blijven toch het mislukte biertje na een lange wandeling, de dubbele etappes per dag bij de Mont Blanc (want wat doe je anders vanaf 12 uur, als de normale dagwandeling er al op zit?) en het wildkamperen in de Pyreneeën. Met je vele verhalen, filosofische gedachten experimenten en dezelfde insteek van elkaar

helpen, niet zeuren en flink doorstappen, konden we volop genieten van de bergen! Ik hoop dat we snel weer een keer de bergen in kunnen!

Kees, in je masterproject heb jij hebt me wegwijs gemaakt in molecuulspectroscopie. De eerste absorptiemetingen konden toen net gedaan worden en jij kwam elke dag het lab in met weer een meetplan. We hebben toen een aantal erg leuke, productieve en leerzame maanden metingen gedaan in het lab! Daarna ben je gezellig naar de VU gekomen voor een PhD en zijn we samen gaan fietsen! Je stond altijd klaar om mee te denken of te helpen. Ik zou graag Paul (Hofland) en Jelmer willen bedanken voor het goede werk en de gezelligheid in het lab tijdens hun master- en bachelorproject.

I would like to thank Kjeld Eikema, Stefan Witte, Jeroen Koelemeij, Max Beyer, Laura Dreissen and late Wim Vassen for the great scientific discussions and a good and motivating atmosphere in the group. Ik wil graag Rob speciaal bedanken voor alle snelle en goede technische hulp en Johan en Jacob en iedereen van de VU werkplaats voor alle mooie en goede onderdelen voor mijn opstelling en alle quick service in coronatijd. And of course my fellow PhD and Postdoc colleagues Anne, Meissa, Joël, Yuri, Charlaine, Frank, Yuanqing, Kenneth, Ruud, Julian, Vincent, Andrés, Kevin, and all the others from the QMLA group for the help in the lab and the fun during lunch and outside the lab.

Als enige promovendus van de NL-*e*EDM groep op de VU was ik deel van zowel de VU als een RUG groep. Ik heb me altijd erg welkom gevoeld in Groningen. Ik wil graag Steven Hoekstra bedanken voor het leiden van de *e*EDM collaboratie, met al je enthousiaste inzet om er een echte groep van te maken. Anastasia Borschevsky, Lorenz Willmann, Klaus Jungmann, Rob Timmermans, Jordy de Vries and Steven Jones thank you all for the good discussions and the great scientific work.

Ik zou graag Leo en Kevin willen bedanken voor het meedenken en alle hulp met het opbouwen van de cryogene bron. Waar Pi en ik misschien beiden beperkte samenwerking met anderen hadden, vooral in de corona tijd, heb ik erg goede herinneringen aan onze puzzel rond de molecuulconstanten van de hyperfijnstructuur en het samen schrijven van het artikel. Je hebt me toen veel geleerd over artikelen schrijven.

Anno, in het begin van jou PhD heb je voor mij een data acquisitie software geschreven, waar ik vele jaren plezier van heb gehad en je altijd enorm dankbaar voor ben geweest. Je hebt me daarna nog een officieuze Python cursus gegeven met alle ondersteuning die ik kreeg bij het uitbreiden van de software. Je vele bezoeken aan de VU en de diepgaande interesse in mijn werk waren voor ons beiden leerzaam en hebben me nuttig en thuis laten voelen in de groep. Dankjewel ook voor de mooie 3D plaatjes.

Ties, ik ben je erg dankbaar voor het verzilveren van mijn werk door flink te gaan meten met de opstelling. Ik vind het bewonderingswaardig hoe vaak je naar Amsterdam kwam om te meten. Je bracht een hoop gezelligheid mee en met je kwaliteiten leerde je

vlekkeloos de opstelling kennen. Het doet me erg goed dat je veel van de metingen hebt kunnen doen aan BaOH waar ik zelf niet meer aan toe ben gekomen. Ik ben natuurlijk ook een beetje jaloers dat je nu een molecuulspectroscopie expert bent geworden. Dank ook voor het lezen van delen van mijn proefschrift.

Joost, altijd enthousiast en gezellig bracht je een hoop energie. Dankjewel voor het nalezen van delen van mijn proefschrift. Ginny, thank you for the data collecting and analysis of the hyperfine structure. I would like to thank Alexander, Thomas, Parul, Nithesh, Yanning, Malika, Yongliang, Artem and all the others of the Groningen group for the great work on the *e*EDM and the fun Ameland summerschools!

Maarten, we kennen elkaar sinds de intreeweek en sindsdien is het altijd leuk en vertrouwd. Ik vind het dan ook erg leuk dat je mijn paranimf bent. Er was naast studeren veel gezelligheid met z'n drieën bij jou eten of naar de molen, waardoor ik me altijd meer thuis heb gevoeld in Amsterdam. Nu zien we elkaar nog steeds geregeld en het is leuk om te zien hoe je zo bezig bent met die jongens. Ik heb ook erg genoten van de wekelijkse bezoekjes op Roeterseiland. Bedankt voor alle jaren vriendschap!

Paul, ik heb weinig mensen zo vaak gezien de afgelopen jaren als jou en naar mijn mening had het vaker gemogen. Eerst met klussen in de matloods, maar met name in coronatijd toen we 5 minuten lopen uit elkaar woonden. Ik denk nog regelmatig met veel plezier terug aan onze dagelijkse half uurtje voetballen in het Oosterpark, een goede onderbreking van het thuiswerken. En nu, ondanks dat ik ben verhuisd naar Edam, kom je nog steeds bijna elke twee weken langs. Je bent altijd relaxed, geïnteresseerd en trouw.

Ik wil graag Marius bedanken voor de gezelligheid en het logeeradres in Groningen.

Verder zou ik graag mijn familie willen bedanken voor alle steun en hulp. Speciale herinneringen heb ik aan de twee midweken schrijven bij mijn ouders in Middelburg, met oppas voor Floris. Buiten de productieve dagen was het ook erg leuk dat jullie Floris en Floris jullie echt leerden kennen. Charlotte, Robert, Christianne en Arno, dank voor alle gezellige avonden en Artis bezoeken. Dankjewel Anne voor eindeloze PhD interesse en support en het nalezen van delen van mijn proefschrift. Daarnaast wil ik graag mijn schoonfamilie bedanken. Ina en Theo, bedankt voor het oppassen op Floris, zodat ik kon schrijven en hij een leuke dag op de boerderij had! Irene, dankjewel voor het helpen met de jongens en nalezen van de samenvatting.

Suzan, toen ik mijn PhD begon, was je nog mijn buurmeisje. Inmiddels wonen we in Edam met twee lieve kleine jongetjes, Floris en Tobias. Hoewel ik in het begin mijn PhD redelijk bij mezelf kon houden, werd je helaas richting het einde ongevraagd erbij betrokken. Je hebt me desondanks door de jaren heen altijd geholpen en heel veel ruimte gegeven ondanks de drukte met de twee jongens, eerst voor lange dagen meten, en later voor de vele uren en avonden schrijven. Bedankt voor alles!